AVANCES EN SISTEMAS INTERACTIVOS PARA PERSONAS CON PARÁLISIS CEREBRAL

Farhan Akram

ADVERTIMENT. L'accés als continguts d'aquesta tesi doctoral i la seva utilització ha de respectar els drets de la persona autora. Pot ser utilitzada per a consulta o estudi personal, així com en activitats o materials d'investigació i docència en els termes establerts a l'art. 32 del Text Refós de la Llei de Propietat Intel·lectual (RDL 1/1996). Per altres utilitzacions es requereix l'autorització prèvia i expressa de la persona autora. En qualsevol cas, en la utilització dels seus continguts caldrà indicar de forma clara el nom i cognoms de la persona autora i el títol de la tesi doctoral. No s'autoritza la seva reproducció o altres formes d'explotació efectuades amb finalitats de lucre ni la seva comunicació pública des d'un lloc aliè al servei TDX. Tampoc s'autoritza la presentació del seu contingut en una finestra o marc aliè a TDX (framing). Aquesta reserva de drets afecta tant als continguts de la tesi com als seus resums i índexs.

ADVERTENCIA. El acceso a los contenidos de esta tesis doctoral y su utilización debe respetar los derechos de la persona autora. Puede ser utilizada para consulta o estudio personal, así como en actividades o materiales de investigación y docencia en los términos establecidos en el art. 32 del Texto Refundido de la Ley de Propiedad Intelectual (RDL 1/1996). Para otros usos se requiere la autorización previa y expresa de la persona autora. En cualquier caso, en la utilización de sus contenidos se deberá indicar de forma clara el nombre y apellidos de la persona autora y el título de la tesis doctoral. No se autoriza su reproducción u otras formas de explotación efectuadas con fines lucrativos ni su comunicación pública desde un sitio ajeno al servicio TDR. Tampoco se autoriza la presentación de su contenido en una ventana o marco ajeno a TDR (framing). Esta reserva de derechos afecta tanto al contenido de la tesis como a sus resúmenes e índices.

WARNING. Access to the contents of this doctoral thesis and its use must respect the rights of the author. It can be used for reference or private study, as well as research and learning activities or materials in the terms established by the 32nd article of the Spanish Consolidated Copyright Act (RDL 1/1996). Express and previous authorization of the author is required for any other uses. In any case, when using its content, full name of the author and title of the thesis must be clearly indicated. Reproduction or other forms of for profit use or public communication from outside TDX service is not allowed. Presentation of its content in a window or frame external to TDX (framing) is not authorized either. These rights affect both the content of the thesis and its abstracts and indexes.

UNIVERSITAT ROVIRA i VIRGILI

Active contours for intensity inhomogeneous image segmentation

FARHAN AKRAM

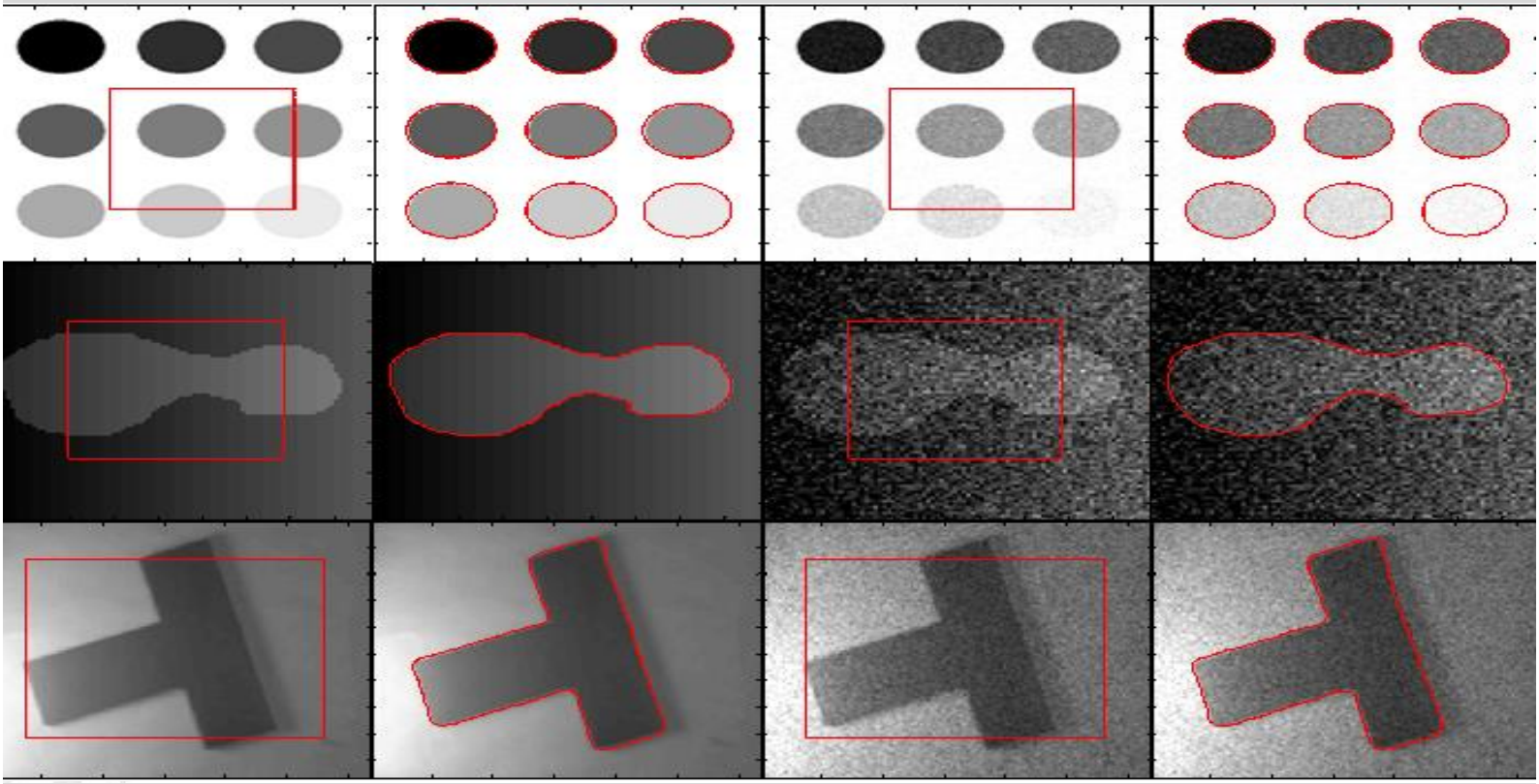

DOCTORAL THESIS
2017

UNIVERSITAT ROVIRA I VIRGILI
AVANCES EN SISTEMAS INTERACTIVOS PARA PERSONAS CON PARÁLISIS CEREBRAL
Farhan Akram

Active contours for intensity inhomogeneous image segmentation

DOCTORAL THESIS

Author:
Farhan Akram

Advisors:
Dr. Domènec Savi Puig Valls
Dr. Miguel Ángel García García

Departament d'Enginyeria Informàtica i Matemàtiques

UNIVERSITAT ROVIRA I VIRGILI
Tarragona
2017

UNIVERSITAT ROVIRA I VIRGILI
AVANCES EN SISTEMAS INTERACTIVOS PARA PERSONAS CON PARÁLISIS CEREBRAL
Farhan Akram

UNIVERSITAT ROVIRA I VIRGILI
Departament d'Enginyeria Informàtica i Matemàtiques

Av. Paisos Catalans, 27
43007 Tarragona
Tel. +34 977 55 95 95
Fax. +34 977 55 95 97

We STATE that the present study, entitled "Active contours for intensity inhomogeneous image segmentation", presented by Farhan Akram, for the award of the degree of Doctor, has been carried out under our supervision at the Departament d'Enginyeria Informàtica i Matemàtiques.

Tarragona, 26th May 2017.

Doctoral Thesis Supervisors,

Dr. Domènec Savi Puig Valls

Dr. Miguel Ángel García García

UNIVERSITAT ROVIRA I VIRGILI
AVANCES EN SISTEMAS INTERACTIVOS PARA PERSONAS CON PARÁLISIS CEREBRAL
Farhan Akram

To my mother Farhat Yasmin,
To my father Mumhammad Akram &
To my wife Tehreem

UNIVERSITAT ROVIRA I VIRGILI
AVANCES EN SISTEMAS INTERACTIVOS PARA PERSONAS CON PARÁLISIS CEREBRAL
Farhan Akram

Abstract

Intensity inhomogeneity is a well-known problem in image segmentation, which affects the accuracy of intensity-based segmentation methods. In this thesis, edge-based and region-based active contour methods are proposed to segment intensity inhomogeneous images. Firstly, we have proposed an edge-based active contour method based on the Difference of Gaussians (DoG), which helps to segment the global structure of the image. Secondly, we have proposed a region-based active contour method to both correct and segment intensity inhomogeneous images. A phase stretch transform (PST) kernel has been used to compute new intensity means and bias field, which are employed to define a bias fitted image. A new signed pressure force (SPF) function has been formulated with a bias image fitted difference to stabilize the gradient descent flow. Thirdly, another region-based active contour method has been proposed using an energy functional based on local and global fitted images. Moreover, local and global SPF functions have been introduced in the solution of the energy functional to stabilize the gradient descent flow. Intensity inhomogeneous images contain undesired smooth intensity variations (bias field) that alter the results of intensity-based segmentation methods. In the proposed region-based methods, the bias field is approximated with a Gaussian distribution and the bias of intensity inhomogeneous regions is corrected by dividing the original image by the approximated bias field. Finally, a hybrid region-based multiphase (four-phase) active contours method has been proposed to partition a brain MR image into three distinct regions: white matter (WM), gray matter (GM) and cerebrospinal fluid (CSF). The proposed energy functional has been formulated by combining local and global fitted images in a multiplicative fashion. In this work, a post processing (pixel correction) method has also been devised to improve the accuracy of the segmented WM, GM and CSF regions in a brain MR image. Experimental results with both synthetic and real brain MR images have been used for a quantitative and qualitative comparison with state-of-the-art active contour methods to show the advantages of the proposed segmentation techniques.

Keywords: Active contours, edge-based, region-based, multiphase, local and global fitted images, biased fitted image, signed pressure force, magnetic resonance imaging, brain segmentation, pixel correction, thresholding, phase stretch transform, bias correction.

Acknowledgements

I would like to express my gratitude to my advisors Dr. Domenec Savi Puig Valls and Dr. Miguel Angel Garcia Garcia for giving me the opportunity to work under their academic supervision and for their dedication, guidance and support during these years.

During the last years, I have met many people from whom I have learnt a lot. To all of them, thank you very much for each of the great moments that we have shared and also for the great talks that I am completely sure we have had. I also would like to thank each of the former and current members of the Intelligent Robotics and Computer Vision Group for their companionship and friendship.

I would like to thank Agency of Management of University and Research Grants (AGAUR) and Universitat Rovira i Virgili for the financial support given to me through a doctoral scholarship.

I would also like to thank my wife, parents, brothers and sisters, for their love, support and encouragement. Without them, this thesis would not have been possible.

Last but not the least, I want to express my gratitude to all those anonymous reviewers who have made useful revisions on my conference and journal publications.

Contents

UNIVERSITAT ROVIRA I VIRGILI
AVANCES EN SISTEMAS INTERACTIVOS PARA PERSONAS CON PARÁLISIS CEREBRAL
Farhan Akram

UNIVERSITAT ROVIRA I VIRGILI
AVANCES EN SISTEMAS INTERACTIVOS PARA PERSONAS CON PARÁLISIS CEREBRAL
Farhan Akram

UNIVERSITAT ROVIRA I VIRGILI
AVANCES EN SISTEMAS INTERACTIVOS PARA PERSONAS CON PARÁLISIS CEREBRAL
Farhan Akram

List of Figures

UNIVERSITAT ROVIRA I VIRGILI
AVANCES EN SISTEMAS INTERACTIVOS PARA PERSONAS CON PARÁLISIS CEREBRAL
Farhan Akram

UNIVERSITAT ROVIRA I VIRGILI
AVANCES EN SISTEMAS INTERACTIVOS PARA PERSONAS CON PARÁLISIS CEREBRAL
Farhan Akram

List of Tables

UNIVERSITAT ROVIRA I VIRGILI
AVANCES EN SISTEMAS INTERACTIVOS PARA PERSONAS CON PARÁLISIS CEREBRAL
Farhan Akram

CHAPTER 1

Introduction

1.1 Image segmentation

In computer vision and image processing, segmentation is a process of partitioning a digital image into multiple non-overlapping regions. The main goal is to simplify or change the image into something more meaningful or easier to analyse. Intensity inhomogeneity is one of the well-known problems in image segmentation, which can substantially reduce the accuracy of intensity-based segmentation methods. It manifests as a smooth intensity variation across the image that complicates the segmentation of the objects contained in it.

Numerous segmentation methods have been proposed so far, such as thresholding (Batenburg and Sijbers, 2009), clustering methods (Barghout and Sheynin, 2013; Guberman et al., 2012), histogram-based methods (Ohlander et al., 1978), edge detection (Kimmel, 2003), region growing methods (Nock and Nielsen, 2004; Chen

UNIVERSITAT ROVIRA I VIRGILI
AVANCES EN SISTEMAS INTERACTIVOS PARA PERSONAS CON PARÁLISIS CEREBRAL
Farhan Akram

et al., 1994) and variational and partial differential equation (PDE)-based methods (level-sets and active contours) (Kass et al., 1988; Osher and Sethian, 1988; Caselles et al., 1997; Osher and Paragios, 2003; Chan and Vese, 2001; Mumford and Shah, 1989).

1.2 Intensity inhomogeneity

Intensity inhomogeneity is one of the well-known problems in image segmentation, which arises from the imperfections of the image acquisition process or due to external interferences. It manifests as a smooth intensity variation across the image that complicates the segmentation of the objects contained in it. For instance, in medical image analysis, segmentation and registration stages are highly sensitive to spurious variations of image intensity. Therefore, the complexity of intensity inhomogeneity can lead to false results and assumptions that can be critical for decision making by both doctors and radiologists. This is why numerous methods for intensity inhomogeneity correction have been proposed in the past (Vovk et al., 2007).

Thus, intensity inhomogeneity correction is often a pre-processing stage necessary for achieving better image segmentation. In turn, correct segmentation makes intensity inhomogeneity correction rather trivial. Actually, both intensity inhomogeneity correction and segmentation can be viewed as two intertwined processes. In segmentation-based intensity inhomogeneity correction methods, both processes are merged such that they benefit from each other.

The techniques that aim to avoid intensity inhomogeneity in the image acquisition process are known as *prospective methods*. They are only capable of correcting intensity inhomogeneity caused by the imaging device, not being able to segment the objects affected by intensity inhomogeneity. On the other hand, techniques that can correct an image and also segment the objects affected by intensity inhomogeneity are called *retrospective methods*. Retrospective methods are further classified according to the image segmentation method they apply into: filtering methods (Lewis and Fox, 2004; Studholme et al., 2004), surface fitting methods (Meyer et al., 1995;

Vokurka et al., 1999), histogram-based methods (Vovk et al., 2004, 2006), and active contours (Li et al., 2008a, 2011; Zhang et al., 2015, 2016; Li et al., 2009a,b; Huang and Zeng, 2015). Segmentation-based methods (Li et al., 2011; Zhang et al., 2015, 2016) are the most versatile, since they unify segmentation and bias correction in a single framework. In these methods, segmentation and bias correction are applied in conjunction to benefit from each other.

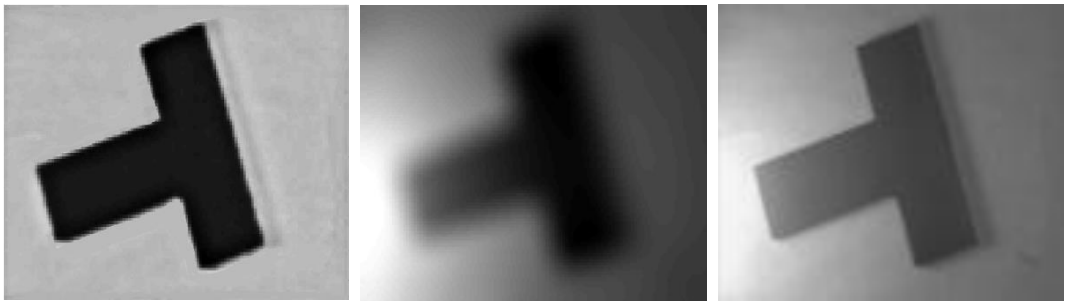

(a) (b) (c)

Figure 1.1: From homogeneous to inhomogeneous. (a) Homogeneous image, (b) Bias that causes intensity inhomogeneity and (c) Intensity inhomogeneous image.

Figure 1.1 shows an example of an image affected by intensity inhomogeneity, which can be caused by imaging device or by the environmental interference.

1.3 Active contours

Active contours are retrospective methods suitable for both image segmentation and bias correction (Li et al., 2011, 2014; Ivanovska et al., 2016; Kahali et al., 2016; Zhang et al., 2015, 2016). The first active contour method was proposed by Kass et al. (1988) in order to segment an image by evolving a curve towards the boundary of an object contained in the image. The active contours are represented as parametrized curves in a Lagrangian framework (Kass et al., 1988) and the implicit curves in an Eulerian framework (Chan and Vese, 2001; Mumford and Shah, 1989; Malladi et al., 1995; Li et al., 2005). The main idea behind active contours is to formulate an energy functional by using image statistics, curvature and gradient information. The energy functional is then minimized to evolve the level-set curve towards the desired object boundary. Currently, various active contour models and enhanced

UNIVERSITAT ROVIRA I VIRGILI
AVANCES EN SISTEMAS INTERACTIVOS PARA PERSONAS CON PARÁLISIS CEREBRAL
Farhan Akram

versions are employed in various image processing applications, as well as medical image analysis. Active contour methods can be categorized into edge-based (Kass et al., 1988; Caselles et al., 1997; Li et al., 2005) and region-based (Mumford and Shah, 1989; Chan and Vese, 2001; Akram et al., 2015a; Li et al., 2007, 2008b; Zhang et al., 2010a; Akram et al., 2014; Peng et al., 2014; Xie et al., 2015; Wang et al., 2010, 2009b; Li et al., 2015) methods. Both types have strengths and limitations.

Edge-based methods, as their name states, use image edge information as a balloon force to evolve the curve towards the object boundaries (Caselles et al., 1997). The level-set method without re-initialization (LSWR) and the distance regularized level-set (DRLS) method are devised by Li et al. to segment image objects and remove the re-initialization step during the curve evolution (Kass et al., 1988; Caselles et al., 1997). However, these methods are unable to segment objects with weak and/or blurred boundaries.

In turn, region-based methods can properly segment images with weak and/or blurred boundaries by using image statistical information. Traditional region-based methods (Chan and Vese, 2001; Mumford and Shah, 1989) are formulated under the assumption that images are homogeneous; therefore, they cannot segment intensity inhomogeneous images.

1.4 Motivation

Numerous region-based methods have been proposed to segment intensity inhomogeneous images by introducing image local information in their models (Li et al., 2007, 2008b; Zhang et al., 2010a; Akram et al., 2014). A region scalable fitting (RSF) method for image segmentation was proposed by Li et al. (2008b, 2007) in the context of intensity inhomogeneity. In this method, a Gaussian kernel is introduced in the energy formulation to exploit the image local information. A localized active contour method (LAC) was devised by Lankton and Tannenbaum (2008), in which global region-based methods are reformulated by replacing the global means with image local information. These methods can segment intensity

inhomogeneous regions, unlike their global counterparts. However, these methods are sensitive to the position of the initial contour. Moreover, they also have a high computational cost due to the complex local information in their formulation.

A region-based active contour model with a variational level-set formulation for image segmentation was presented by Wang et al. (2009a). It uses local intensity means described by local Gaussian distributions (LGD) in order to compute the level-set curve. It can be used to segment images in the presence of intensity inhomogeneity and noise. However, it is sensitive to the position of the initial contour. Moreover, it also needs a high value of a parameter of the Gaussian kernel (sigma) to properly delineate the object, which increases the overall time complexity of the model.

A local active contour model for segmenting images with intensity inhomogeneity was proposed by Zhang et al. (2010a). Local image information is used to define a local image fitting (LIF) energy functional, which can be interpreted as a constraint on the differences between the fitting image (Li et al., 2007, 2008b) and the original image. Furthermore, a new method is used to regularize the level-set function by using Gaussian kernel filtering after each iteration. In addition, re-initialization of the level-set curve is not required. However, this method is sensitive to the initial contour, and the final contour does not strictly follow the object boundary.

Alternatively, a region-based active contour method was formulated by Akram et al. (2014) in the context of intensity inhomogeneity by utilizing local intensity means. It uses a signed pressure force (SPF) function based on a local fitted image in its energy formulation in order to segment images with intensity inhomogeneity. A Gaussian kernel is used to smooth the level-set function after every step. Therefore, this method does not require re-initialization. This method has a high time complexity compared to the traditional global region-based methods (Chan and Vese, 2001; Mumford and Shah, 1989).

A variational level-set approach for bias correction and segmentation (VLSBCS) for images corrupted with intensity inhomogeneity was proposed by Li et al. (2011, 2008a). The computed bias field is intrinsically ensured to be smooth by the data

UNIVERSITAT ROVIRA I VIRGILI
AVANCES EN SISTEMAS INTERACTIVOS PARA PERSONAS CON PARÁLISIS CEREBRAL
Farhan Akram

term in the variational formulation, without any additional effect to maintain the smoothness of the bias field. A local statistical active contour model (LSACM) for image segmentation in the presence of intensity inhomogeneity was proposed by Zhang et al. (2015, 2016). In this work, the inhomogeneous objects are modelled as Gaussian distributions of different means and variances. A statistical energy functional is then defined for each local region, which combines the bias field, the level-set function, and the constant approximating the true signal of the corresponding object. Both of these methods are able to segment and correct intensity inhomogeneous images. However, they are also sensitive to the initial contours and have a high time complexity.

Figure 1.2 shows an example of intensity inhomogeneous image segmentation using active contours. Figure 1.2(a) shows that a traditional active contour method, such as CV (Chan and Vese, 2001), is unable to segment intensity inhomogeneous objects. In turn, figure 1.2(b) shows that a local active contour method, such as RSF (Li et al., 2008b), is able to properly segment intensity inhomogeneous objects. However, local active contour methods have a high computational complexity because of the intensity mean computations in the local neighbourhoods during the contour evolution process. Edge-based active contour methods can segment intensity inhomogeneous objects, although these methods do not guarantee that the level-set curve will stop at the object boundary if it is blur or the intensity difference between the background and the object boundary is not clear.

1.5 Objectives

In this thesis, different active contour methods are proposed to segment intensity inhomogeneous images. The main objectives are:

- Devise an edge-based active contour method to segment images with intensity inhomogeneity with weak and/or blurred object boundaries.
- Devise a retrospective region-based active contour method to both segment and correct intensity inhomogeneity.

UNIVERSITAT ROVIRA I VIRGILI
AVANCES EN SISTEMAS INTERACTIVOS PARA PERSONAS CON PARÁLISIS CEREBRAL
Farhan Akram

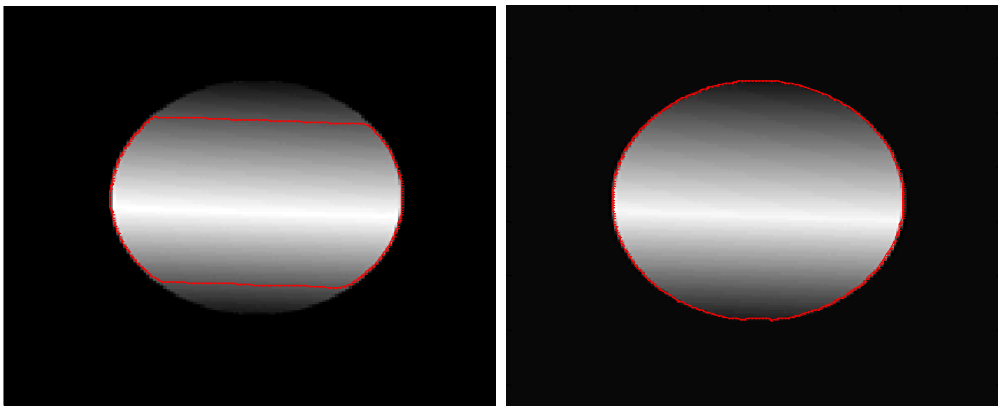

(a) (b)

Figure 1.2: Intensity inhomogeneous image segmentation using active contours. (a) Image segmentation using a traditional active contour method. (b) Image segmentation using a local active contour method.

- Devise a multiphase region-based active contour method to segment both 2D and 3D brain MR images.
- The proposed methods should be robust to intensity inhomogeneities irrespectively of the noise interference.
- The proposed methods should be computationally more efficient than the state-of-the-art.
- The proposed methods should not be sensitive to the initial position of the level-set curve.

1.6 Thesis organization

The rest of thesis is organized as follows. Theoretical background is discussed in chapter 2. From chapter 3 to 5, different active contour methods are proposed to segment intensity inhomogeneous images. An edge-based active contour method driven by the difference of Gaussians is proposed in chapter 3. In chapter 4, a novel retrospective region-based active contour method is proposed by using a biased fitted image. In chapter 5, a retrospective region-based active contour method is proposed by using both local and global image fitted differences. A multiphase (four-phase) region-based active contour method is proposed in chapter 6, which is used to segment brain MR images into white matter (WM), gray matter (GM) and cerebrospinal fluid

UNIVERSITAT ROVIRA I VIRGILI
AVANCES EN SISTEMAS INTERACTIVOS PARA PERSONAS CON PARÁLISIS CEREBRAL
Farhan Akram

(CSF) regions. Finally, the thesis is concluded and future work is discussed in the last chapter.

CHAPTER 2

Theoretical foundations

2.1 Introduction

Active contours (also known as snakes) is one of the well-known segmentation methods, as mentioned in chapter 1. This method was proposed by Kass et al. (1988) in order to extract the interesting objects in an image, by evolving a level-set curve towards the object boundaries. Active contours are represented as parametrized curves in a Lagrangian framework (Kass et al., 1988) and as implicit curves in an Eulerian framework (Chan and Vese, 2001; Mumford and Shah, 1989; Malladi et al., 1995; Li et al., 2005). The main idea behind active contours is to formulate an energy functional by using image statistics, curvature and gradient information. The energy functional is then minimized to evolve the level-set curve towards the desired object boundaries. Currently, a wide variety of active contour models and enhanced versions are employed in various image processing applications, as well in medical

UNIVERSITAT ROVIRA I VIRGILI
AVANCES EN SISTEMAS INTERACTIVOS PARA PERSONAS CON PARÁLISIS CEREBRAL
Farhan Akram

image analysis.

Active contour models are further divided into two main categories: edge-based methods (Kass et al., 1988; Caselles et al., 1997; Li et al., 2005, 2010) and region-based methods (Chan and Vese, 2001; Li et al., 2008a; Zhang et al., 2010b; Akram et al., 2015a) models. Both types have strengths and limitations as discussed below.

2.2 Edge-based active contour methods

Edge-based methods, as their name states, use image edge information as a balloon force to evolve the curve towards the object boundaries. However, these types of methods are unable to segment object with weak and/or blurred boundaries.

2.2.1 Snakes

In the classical energy-based snakes approach, first introduced by Kass et al. (1988), the curve C is associated with an energy given by Eq. (2.1), where p parametrizes the curve $0 \leq p \leq 1$, and α, β, and λ are real positive constants. The first two terms control the smoothness of the contours to be detected: α the "tension" and β the "rigidity". In turn, the third term is responsible for attracting the contour towards the object in the image. In this approach, the curve is parametrized with points $(x_i\ ,\ y_i)$ and the arc length. This method of parametrizing the curve is known as the Lagrangian approach (common in fluid mechanics problems), which focuses attention on material particles as they move through the flow (Panton, 2013). Although effective in giving a continuous boundary, this approach cannot directly deal with changes in topology. The curve points may "tangle" and "collide" as the curve evolves. It is thus crucial that prior knowledge be obtained and a reasonable initial curve be set such that the algorithm gives meaningful results.

$$E(C) = \alpha \int_0^1 |C'(p)|^2 dp + \beta |C''(p)|^2 dp - \lambda \int_0^1 |\nabla I(C(p))| dp \tag{2.1}$$

2.2.2 Geodesic active contour (GAC) model

Caselles et al. (1993, 1997) and Malladi et al. (1995) further enhanced the idea of snakes by developing a curve evolution flow which can better accommodate the object geometry and the changing topology as the curve evolves. The basic idea stems from Euclidean curve shortening and the use of level-sets when evolving the curve. Let Ω be a bounded open subset of $\mathbf{R}^2$ and $I : [0, a] \times [0, b] \rightarrow \mathbf{R}^+$ be a given image. Let $C(q) : I[0, 1] \rightarrow \mathbf{R}^2$ be a parametrized planer curve in Ω. The GAC model is formulated by minimizing the following energy functional:

$$E_{GAC}(C) = \int_0^1 g(|\nabla I(C(q))|)|C(q)|dq, \tag{2.2}$$

where g is the edge indicator function defined as:

$$g(|\nabla I|) = \frac{1}{1 + |\nabla G_\sigma * I|^2} \tag{2.3}$$

By applying the calculus of variations (Aubert and Kornprobst, 2010) to Eq. (2.2), the following Euler-Lagrange equation is obtained:

$$C_t = g(|\nabla I|)\kappa\overrightarrow{N} - (\nabla g.\overrightarrow{N})\overrightarrow{N}, \tag{2.4}$$

where κ is the curvature of the contour and $\overrightarrow{N}$ is the inward normal to the curve. Usually, a constant velocity term α is added to increase the propagation speed. Eq. (2.4) can be rewritten as:

$$C_t = g(|\nabla I|)(\kappa + \alpha)\overrightarrow{N} - (\nabla g.\overrightarrow{N})\overrightarrow{N}. \tag{2.5}$$

The corresponding level-set formulation is as follows:

$$\frac{\partial \phi}{\partial t} = g|\nabla \phi|\Big(div\Big(\frac{\nabla \phi}{|\nabla \phi|}\Big) + \alpha\Big) + \nabla g.\nabla \phi, \tag{2.6}$$

where α is the balloon force, which controls how the contour shrinks or expands.

UNIVERSITAT ROVIRA I VIRGILI
AVANCES EN SISTEMAS INTERACTIVOS PARA PERSONAS CON PARÁLISIS CEREBRAL
Farhan Akram

2.3 Region-based active contour methods

Region-based methods can properly segment images with weak and/or blurred boundaries by using image statistical information. Traditional region-based methods (Chan and Vese, 2001; Mumford and Shah, 1989) are formulated under the assumption that images are homogeneous; therefore, they cannot segment intensity inhomogeneous images. However, some active contour methods have lately been proposed to segment images with intensity inhomogeneities by using image local information. Based on the way intensity means are computed, region-based active contour models can be further divided into two categories: global and local.

2.3.1 Global region-based models

2.3.1.1 Mumford-Shah energy model

For the image segmentation problem, Mumford and Shah (1989) proposed an active contour method to find an optimal piecewise smooth approximation function u of an image. Let $I : \Omega \rightarrow \mathbf{R}^2$, where u varies within each sub-region Ω_i of the image domain smoothly, and rapidly or discontinuously across the boundaries of Ω_i in order to approximate a closed curve $C \subset \Omega$ along the object boundary. They proposed the following energy functional:

$$E_{MS} = \lambda \int_{\Omega} \left|I(x) - u(x)\right|^2 dx + v \int_{\Omega \backslash C} \left|\nabla u(x)\right|^2 dx + \mu L(C), \qquad x \in \Omega \qquad (2.7)$$

where $L(C)$ is the length of the curve C, and μ and $v \geq 0$ are fixed parameters. The unknown contour C and the non-convexity of the above energy functional make it difficult to minimize it. Some alternative methods were later proposed to simplify or modify the above functional, as described below.

2.3.1.2 Chan-Vese model

Chan and Vese (2001) proposed an active contour method based on the Mumford and Shah (1989) model. Let $I : \Omega \to \mathbf{R}^2$ be an input image, $\phi : \Omega \to \mathbf{R}^2$ a level-set, and C a closed curve corresponding to the zero level-set: $C = \{x \in \Omega | \phi(x) = 0\}$. Figure 2.1 illustrates the above assumptions and notations regarding the level-set function ϕ, which defines the evolving curve C. Let C be an evolving curve in Ω, as the boundary of an open subset w of Ω such that, $w \subset \Omega$, and $C = \delta w$. Let us assume that $inside(C)$ denotes the region w and $outside(C)$ denotes the region $\Omega \backslash \overline{w}$. With the above assumptions, the following energy functional is defined:

$$E_{CV} = \lambda_1 \int\limits_{inside(C)} \big|I(x) - c_1\big|^2 dx + \lambda_2 \int\limits_{outside(C)} \big|I(x) - c_2\big|^2 dx + \mu.\,\text{Length}(C) + v.\,\text{Area}\big(inside(C)\big), \quad x \in \Omega \tag{2.8}$$

Using the Heaviside function H_ϵ, and the one-dimensional Dirac function δ_ϵ, the energy functional E_{CV} becomes:

$$E_{CV} = \lambda_1 \int\limits_{\Omega} \big|I(x) - c_1\big|^2 H_\epsilon(\phi) dx + \lambda_2 \int\limits_{\Omega} \big|I(x) - c_2\big|^2 \big(1 - H_\epsilon(\phi)\big) dx + \mu \int\limits_{\Omega} \big|\nabla H_\epsilon(\phi)\big|^2 dx + v \int\limits_{\Omega} H_\epsilon(\phi) dx, \tag{2.9}$$

where $\mu \geq 0$, $v \geq 0$, $(\lambda_1, \lambda_2) > 0$ are fixed parameters and $H_\epsilon(\phi)$ is the regularized version of the Heaviside function:

$$H_\epsilon(\phi) = \frac{1}{2} + \frac{1}{\pi} arctan\Big(\frac{\phi}{\epsilon}\Big) \tag{2.10}$$

Parameter ϵ controls the smoothness of the Heaviside function. For $\epsilon \to 0$, the Heaviside function is the ideal unit step function. Parameter μ scales the Euclidean

UNIVERSITAT ROVIRA I VIRGILI
AVANCES EN SISTEMAS INTERACTIVOS PARA PERSONAS CON PARÁLISIS CEREBRAL
Farhan Akram

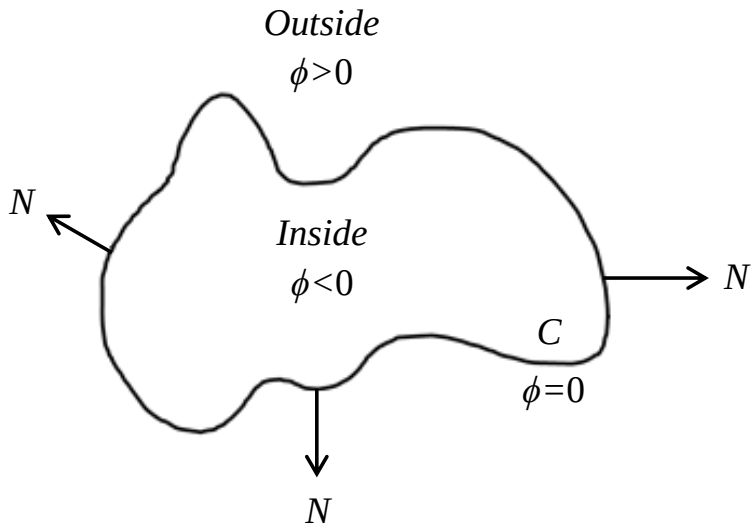

Figure 2.1: Curve C=$\{x : \phi\ (x)$=$0\}$ propagating along the normal direction N

length of the curve C in Eq. (2.9), which is used to regularize the contour. In turn, parameter v scales the area term in Eq. (2.9), which is used to compute the area of the region inside C. Constants c_1 and c_2 approximate the image intensities inside and outside contour C, respectively. By minimizing the above energy functional with respect to ϕ through steepest gradient descent (Aubert and Kornprobst, 2010), the following gradient descent flow is obtained:

$$\frac{\partial \phi}{\partial t} = \Big(-\lambda_1 \big(I(x) - c_1\big)^2 + \lambda_2 \big(I(x) - c_2\big)^2 + \mu\, \mathrm{div}\left(\frac{\nabla \phi}{|\nabla \phi|}\right) - v \Big) \delta_\epsilon(\phi), \qquad (2.11)$$

where $\delta_\epsilon(\phi)$ is the regularized Dirac function:

$$\delta_\epsilon(\phi) = \frac{\epsilon}{\pi(\phi^2 + \epsilon^2)} \qquad (2.12)$$

In addition to specifying the smoothness of the Heaviside function defined in Eq. (2.10), parameter ϵ also controls the width of the Dirac function. For $\epsilon \to 0$, the Dirac function is the ideal unit impulse. By minimizing Eq. (2.9) with respect to c_1 and c_2 while keeping ϕ constant, c_1 and c_2 are defined as:

$$c_1 = \frac{\int\limits_{\Omega} I(x)H_\epsilon(\phi)dx}{\int\limits_{\Omega} H_\epsilon(\phi)dx},$$
$$c_2 = \frac{\int\limits_{\Omega} I(x)\big(1 - H_\epsilon(\phi)\big)dx}{\int\limits_{\Omega} \big(1 - H_\epsilon(\phi)\big)dx} \tag{2.13}$$

The data fitting term $-\lambda_1(I - c_1)^2 + \lambda_2(I - c_2)^2$ in Eq. (2.11) plays a key role in the curve evolution. Parameters λ_1 and λ_2 weight the first and the second terms, respectively. In most cases, $\lambda_1 = \lambda_2$ and $v = 0$ when the image is smooth and the signal-to-noise ratio is low. Parameter μ is a scale factor. If it is low enough, small objects are likely to be extracted. Alternatively, if it is high, big objects can be detected (Chan and Vese, 2001). Obviously, c_1 and c_2 in Eq. (2.13) are related to the global properties of the image contents inside and outside curve C, respectively. However, such a global image segmentation is not accurate if the image intensity inside and/or outside the curve is inhomogeneous.

2.3.1.3 Active contour with selective local and global segmentation (ACSLG)

A region-based active contour model (ACM) using a new signed pressure force (SPF) function based on global intensity means was proposed by Zhang et al. (2010b). The SPF function defined in (Xu et al., 2000) is in the range [1, 1]. It modulates the sign of the pressure force inside and outside the region of interest and it is used to shrink the contour when it is outside the object and to expand it when it is inside the object. The mathematical formulation of the proposed SPF function is as follows:

$$spf(I) = \begin{cases} \frac{I(x) - \frac{c_1+c_2}{2}}{\max\left(\left|I(x) - \frac{c_1+c_2}{2}\right|\right)}, & I(x) \neq 0 \\ 0, & I(x) = 0 \end{cases} \qquad x \in \Omega, \tag{2.14}$$

UNIVERSITAT ROVIRA I VIRGILI
AVANCES EN SISTEMAS INTERACTIVOS PARA PERSONAS CON PARÁLISIS CEREBRAL
Farhan Akram

where c_1 and c_2 are defined in Eq. (2.13). By replacing the edge indicator $g(I)$ in Eq. (2.6) with the SPF function $spf(I)$, the following formulation is obtained:

$$\frac{\partial \phi}{\partial t} = g|\nabla \phi|\Big(div\Big(\frac{\nabla \phi}{|\nabla \phi|}\Big) + \alpha\Big) + \nabla g.\nabla \phi, \tag{2.15}$$

2.3.2 Local region-based models

2.3.2.1 Region scalable fitted (RSF) model

Li et al. (2008b, 2007) proposed the RSF model by embedding local image information in the energy functional. RSF is able to segment images with intensity inhomogeneity. The basic idea is to introduce a Gaussian kernel function to define the RSF energy functional as follows:

$$\begin{aligned} E_{_{RSF}} = \lambda_1 \int\limits_{\Omega} K_\sigma(x-y)\big|I(y) - f_1(x)\big|^2 H_\epsilon(\phi) dydx \\ + \lambda_2 \int\limits_{\Omega} K_\sigma(x-y)\big|I(y) - f_2(x)\big|^2 \big(1 - H_\epsilon(\phi)\big) dydx, \end{aligned} \tag{2.16}$$

where $(\lambda_1, \lambda_2) > 0$ are fixed parameters, $I : \Omega \to \mathbf{R}^2$ is an input image, K_σ is a Gaussian kernel with standard deviation σ, and f_1 and f_2 are two smooth functions that approximate the local image intensities inside and outside curve C, respectively.

In RSF, $C \subset \Omega$ can be represented by the zero level-set of a Lipschitz function $\phi : \Omega \subset \mathbf{R}$. By minimizing the energy functional $E_{_{RSF}}$ with respect to ϕ, the gradient descent flow is defined as follows:

$$\frac{\partial \phi}{\partial t} = -(\lambda_1 e_1 - \lambda_2 e_2)\delta_\epsilon(\phi), \tag{2.17}$$

where e_1 and e_2 are defined as:

$$e_1(x) = \int_{\Omega} K_\sigma(x-y)\big|I(y) - f_1(x)\big|^2 dy,$$
$$e_2(x) = \int_{\Omega} K_\sigma(x-y)\big|I(y) - f_2(x)\big|^2 dy \tag{2.18}$$

In Eq. (2.17), parameters λ_1 and λ_2 weight the two integrals over the regions inside and outside curve C, respectively, which are defined in Eq. (2.18). In most cases, $\lambda_1 = \lambda_2$. Functions f_1 and f_2 are the local intensity means inside and outside curve C, which are computed in a local neighbourhood:

$$f_1(x) = \frac{K_\sigma * \big[I(x)H_\epsilon(\phi)\big]}{K_\sigma * H_\epsilon(\phi)},$$
$$f_2(x) = \frac{K_\sigma * \big[I(x)\big(1 - H_\epsilon(\phi)\big)\big]}{K_\sigma * \big(1 - H_\epsilon(\phi)\big)} \tag{2.19}$$

Functions f_1 and f_2 in Eq. (2.19) represent weighted averages of image intensities in a Gaussian window inside and outside the curve, respectively. In that way, the RSF model can handle images with intensity inhomogeneity.

The standard deviation σ of the Gaussian kernel plays an import role in practical applications. It behaves as a scale parameter that controls the region scalability from the small neighbourhood to the whole image domain (Li et al., 2008b). It must be properly chosen according to the images. A too small σ may cause an undesirable result, whereas a too large σ will yield a high computational cost.

In order to guarantee a stable evolution of the level-set function, the distance regularized term defined in (Li et al., 2005) is incorporated into Eq. (2.17). Moreover, the Euclidean length term is used to regularize the zero contour of ϕ. Finally, the total variational formulation is as follows:

$$\frac{\partial \phi}{\partial t} = \gamma\left(\nabla^2\phi - \operatorname{div}\left(\frac{\nabla\phi}{|\nabla\phi|}\right)\right) + \left(\mu \operatorname{div}\left(\frac{\nabla\phi}{|\nabla\phi|}\right) - (\lambda_1 e_1 - \lambda_2 e_2)\right)\delta_\epsilon(\phi), \tag{2.20}$$

UNIVERSITAT ROVIRA I VIRGILI
AVANCES EN SISTEMAS INTERACTIVOS PARA PERSONAS CON PARÁLISIS CEREBRAL
Farhan Akram

where γ is a scaling parameter of the distance regularized energy penalization term that controls the energy leakage and μ is a scaling parameter of the Euclidean length of the curve.

2.3.2.2 Local image fitted (LIF) model

A local image fitting energy functional was proposed by Zhang et al. (2010a), in which the difference between the fitted image and the original image is minimized as follows:

$$E_{_{LIF}} = \frac{1}{2} \int_{\Omega} \left| I(x) - I_{_{LFI}}(x) \right|^2 dx, \tag{2.21}$$

where $I_{_{LFI}}$ is the local fitted image defined as:

$$I_{_{LFI}}(x) = f_1(x) M_1 + f_2(x) M_2, \tag{2.22}$$

where $M_1 = H_\epsilon(\phi)$, $M_2 = \big(1 - H_\epsilon(\phi)\big)$, and f_1 and f_2 are local intensity means in the given image defined in Eq. (2.19). $H_\epsilon(\phi)$ is the regularized version of the Heaviside function defined in Eq. (2.10). Using the calculus of variations and steepest gradient descent (Aubert and Kornprobst, 2010), $E_{_{LIF}}$ in Eq. (2.21) is minimized with respect to ϕ to yield the corresponding gradient descent flow:

$$\frac{\partial \phi}{\partial t} = \big(I(x) - I_{_{LFI}}(x)\big)\big(f_1(x) - f_2(x)\big)\delta_\epsilon(\phi), \tag{2.23}$$

where $\delta_\epsilon(\phi)$ is the regularized Dirac function defined in Eq. (2.12).

2.3.2.3 Variational level-set approach for bias correction and segmentation (VLSBCS)

A variational level-set method for the segmentation and bias correction of images corrupted with intensity inhomogeneity was formulated by Li et al. (2008a, 2011). In this method, the computed bias field is ensured to be smooth exclusively through the data term defined in the energy functional formulation. This method is based on an image model commonly used to describe images with intensity inhomogeneity:

$$I(x) = b(x)J(x) + n(x), \tag{2.24}$$

where $I(x)$ is the input image with intensity inhomogeneity, $J(x)$ is the image to be restored without intensity inhomogeneity, $b(x)$ is the bias field, which represents the modulation of the restored image with the intensity inhomogeneity, and $n(x)$ is noise. The model assumes that the restored image $J(x)$ is constant within each object in the image, i.e., $J(x) \approx \sum_{i=1}^{N} m_i M_i$ for $x \in \Omega_i$, with $x \in \{\Omega_i\}_{i=1}^{N}$ being a sub-region of Ω.

In traditional active contour methods, the image domain Ω is assumed to be divided into N disjoint regions, Ω_i, $i = 1, 2, ..., N$, based on the input image $I(x)$. However, due to the intensity inhomogeneity caused by the bias field $b(x)$, the measured intensities are not separable by using traditional intensity-based segmentation methods.

Li et al. (2008a, 2011) proposed a K-means clustering method based on the minimization of the following objective function:

$$E \cong \int \left(\sum_{i=1}^{N} \int_{\Omega_i} K_\sigma(x-y) \left| I(y) - b(x)m_i \right|^2 dy \right) dx, \tag{2.25}$$

where $b(x)$ is the approximated bias field and m_i is the computed intensity mean in the presence of intensity inhomogeneity for each of the phases of the two-phase active

UNIVERSITAT ROVIRA I VIRGILI
AVANCES EN SISTEMAS INTERACTIVOS PARA PERSONAS CON PARÁLISIS CEREBRAL
Farhan Akram

contour method ($i = 1, 2$). Term $b(x)m_i$ can be considered to be the approximation of the means c_i of the clusters corresponding to each of the phases of the two-phase active contour method: $c_i \approx b(x)m_i$.

Directly minimizing the above energy functional with the partition $\{\Omega_i\}_{i=1}^{N}$ as a variable is not feasible. Therefore, multiple level-set functions are used to represent a partition $\{\Omega_i\}_{i=1}^{N}$. In the simplest case of $N = 2$, the image domain is partitioned into two regions $\{\Omega_1, \Omega_2\}$. These regions are separated by the zero-level contour of a function ϕ, that is, $\Omega_1 \cong \{\phi > 0\}$ and $\Omega_2 \cong \{\phi < 0\}$. Using the Heaviside function H_ϵ, the energy E in Eq. (2.25) becomes:

$$E = \int \left(\sum_{i=1}^{N} \int_{\Omega} K_\sigma(x-y) \big| I(y) - b(x)m_i \big|^2 M_i(\phi) dy \right) dx, \tag{2.26}$$

where M_i is the characteristic function of a given image based on the regularized Heaviside function in Eq. (2.10). When the image domain is partitioned in two regions $\{\Omega_1, \Omega_2\}$, M_i is defined as $M_1 = H_\epsilon(\phi)$ and $M_2 = \big(1 - H_\epsilon(\phi)\big)$. By taking the Gateaux derivative (the first order functional derivative) (Aubert and Kornprobst, 2010) of the energy E, the following expressions for $b(x)$ and m_i are obtained:

$$b(x) = \frac{\sum_{i=1}^{2} K_\sigma * \big[I(x) m_i M_i(\phi) \big]}{\sum_{i=1}^{2} K_\sigma * \big[m_i^2 M_i(\phi) \big]}, \tag{2.27}$$

$$m_i = \frac{\int K_\sigma * \big[I(x) b(x) M_i(\phi) \big] dx}{\int K_\sigma * \big[b^2(x) M_i(\phi) \big] dx}, \tag{2.28}$$

For $N = 4$, the image is partitioned into four regions $(\Omega_1, \Omega_2, \Omega_3, \Omega_4)$ using two level-sets ϕ_1 and ϕ_2. Then, M_i is defined as $M_1(\Phi) = H_\epsilon(\phi_1)H_\epsilon(\phi_2)$, $M_2(\Phi) = H_\epsilon(\phi_1)(1 - H_\epsilon(\phi_2))$, $M_3(\Phi) = (1 - H_\epsilon(\phi_1))H_\epsilon(\phi_2)$ and $M_4(\Phi) = (1 - H_\epsilon(\phi_1))(1 - H_\epsilon(\phi_2))$.

2.3.2.4 Local statistical active contour model (LSACM)

In order to segment and correct bias in an intensity inhomogeneous image, a local statistical active contour model was devised by Zhang et al. (2015, 2016), in which the inhomogeneous objects are modeled as Gaussian distributions of different means and variances. The means of the Gaussian distributions are adaptively estimated by multiplying the bias field by the original signal within a Gaussian window. Let $I : \Omega \rightarrow \mathbf{R}^2$ be the input image, $\Phi : \Omega \rightarrow \mathbf{R}^2$ a level-set function, which yields a closed curve $C = \{x \in \Omega | \Phi(x) = 0\}$, $b(x)$ is the approximated bias field, m_i and σ_i are intensity means and variances, respectively. Φ is a function of one level-set ϕ for a two-phase segmentation and Φ is a function of two level-sets (ϕ_1, ϕ_2) for four-phase segmentation. Based on the above assumptions, an energy functional is defined as:

$$E(\Phi) = \int_{\Omega} K_{\beta}(x,y)\big(log(\sigma_i) + (I(y) - b(x)m_i)^2/2\sigma_i^2\big)M_i(\Phi)dx, \quad N = 2 \; or \; N = 4 \tag{2.29}$$

where $K_{\beta}(x,y)$ is a Gaussian kernel with a standard deviation β. For $N = 2$, the energy functional in Eq. (2.29) acts as a two-phase active contour method (with one level-set). The two characteristic terms are: $M_1(\Phi) = H_{\epsilon}(\phi)$ and $M_2(\Phi) = (1 - H_{\epsilon}(\phi))$. In turn, for $N = 4$, the energy functional in Eq. (2.29) acts as a four-phase active contour method (with two level-sets ϕ_1 and ϕ_2). The four characteristic terms are defined as: $M_1(\Phi) = H_{\epsilon}(\phi_1)H_{\epsilon}(\phi_2)$, $M_2(\Phi) = H_{\epsilon}(\phi_1)(1 - H_{\epsilon}(\phi_2))$, $M_3(\Phi) = (1 - H_{\epsilon}(\phi_1))H_{\epsilon}(\phi_2)$ and $M_4(\Phi) = (1 - H_{\epsilon}(\phi_1))(1 - H_{\epsilon}(\phi_2))$. In Eq. (2.29), bias correction $b(x)$, intensity means m_i and variance σ_i are defined as:

$$b(x) = \frac{\sum_{i=1}^{N} K_{\beta} * (IM_i(\Phi(x))) \cdot \frac{m_i}{\sigma_i^2}}{\sum_{i=1}^{N} K_{\beta} * M_i(\Phi(x)) \cdot \frac{m_i^2}{\sigma_i^2}} \tag{2.30}$$

UNIVERSITAT ROVIRA I VIRGILI
AVANCES EN SISTEMAS INTERACTIVOS PARA PERSONAS CON PARÁLISIS CEREBRAL
Farhan Akram

$$m_i = \frac{\int \big(K_\beta * b\big) I(x) M_i(\phi(x)) dx}{\int \big(K_\beta * b^2\big) M_i(\phi(x)) dx}, \tag{2.31}$$

$$\sigma_i = \sqrt{\frac{\iint K_\beta(x,y)\big(I(x) - b(x)m_i\big)^2 M_i(\phi(x)) dy dx}{\int K_\beta(x,y) M_i(\phi(x)) dy dx}} \tag{2.32}$$

2.4 Summary

Active contours can be categorized into edge-based and region-based methods. Edge-based methods integrate image gradient and/or curvature information in their energy formulation. In turn, region-based methods use image statistical information to formulate the energy functional. Region-based methods can be further divided into local and global models based on the way the intensity means are computed, that is, by using local or global image information. In this chapter, the theoretical background of the different active contour methods has been discussed to set the basis for the following chapters.

CHAPTER 3

Active contours driven by difference of Gaussians

3.1 Introduction

Intensity inhomogeneity is a well-known problem, which negatively affects the segmentation accuracy of intensity-based methods. Active contours is one of the methods used to segment images with intensity inhomogeneities. Edge-based active contour methods can be used to segment intensity inhomogeneous objects. However, the contours will not stop at the boundaries of objects when their edges are not sharp.

In this chapter, an edge-based active contour method driven by the difference of Gaussians (DoG) function is proposed in the context of intensity inhomogeneous

UNIVERSITAT ROVIRA I VIRGILI
AVANCES EN SISTEMAS INTERACTIVOS PARA PERSONAS CON PARÁLISIS CEREBRAL
Farhan Akram

image segmentation. The Gaussian image difference computed by the DoG function provides edge information of the global structure of the given image. This edge information is used as a balloon force in the proposed energy functional to evolve the level-set curve throughout the image structure. An energy penalizing term from (Li et al., 2005) is used to regularize the curve and to maintain the level-set as a signed distance function, which also removes the need for computationally expensive re-initialization of the level set.

This work has three main contributions. First, it is able to segment the global structure of an image unlike traditional edge-based active contours (Li et al., 2005, 2010). Second, it is able to properly segment intensity inhomogeneous images with a low time complexity compared to local region-based methods (Li et al., 2008b; Zhang et al., 2010a; Lankton and Tannenbaum, 2008; Akram et al., 2014). Third, it is not sensitive to the initial position of the level-set curve.

The selection of the standard deviation parameter of the DoG smoothing kernels is critical, specially when the image is highly affected by noise (the parameter difference should be high). The proposed method is applied to both synthetic and real images to show the segmentation accuracy and robustness of the method.

The rest of the chapter is organized as follows. The proposed methodology is presented in section 3.2. Segmentation results for a qualitative comparison using both synthetic and real brain magnetic resonance (MR) images are discussed in section 3.3. The segmentation results are quantitatively compared with state-of-the-art methods in section 3.4. Finally, the chapter is summarized in section 3.5.

3.2 Proposed method

In traditional active contours the curve C is represented by the zero level-set, such that $C = (x, y)|\phi(x, y) = 0$ of a level-set function $\phi(x, y)$. The evolution of the level-set function ϕ can be written in the following general form:

$$\frac{\partial \phi}{\partial t} + F|\nabla \phi| = 0, \tag{3.1}$$

which is referred to as the *level set equation* (Osher and Sethian, 1988). Function F is called the force function. For image segmentation, function F depends on the image data and the level-set function ϕ.

Let $I : \Omega \rightarrow \mathbf{R}^2$ be a given image, C a curve at which the level-set function $\phi(x, y)$ is zero, $C = (x, y)|\phi(x, y) = 0$. The energy functional E is defined as:

$$E(\phi) = E_{int}(\phi) + E_{ext}(\phi), \tag{3.2}$$

In traditional edge-based active contour methods (Malladi et al., 1995; Sethian, 1999; Caselles et al., 1993), it is necessary to re-initialize (reshape) the level -et as a signed distance function during the curve evolution to properly follow and capture the object boundaries. Therefore, it is necessary to keep the evolving level-set function as an approximate signed distance function during the evolution, especially in a neighbourhood around the zero level-set. It is well-known that a signed distance function must satisfy the desirable property that $|\nabla\phi| = 1$. An energy term $P(\phi)$ is proposed in (Li et al., 2005) as a metric to characterize a function ϕ to a signed distance function in $\Omega \in \mathbf{R}^2$, which helps to penalize the deviation of ϕ from a signed distance function during its evolution. The internal energy $E_{int}(\phi)$ is defined as:

$$E_{int}(\phi) = \alpha \int_{\Omega} \frac{1}{2}(|\nabla\phi| - 1)^2 dxdy, \tag{3.3}$$

where α is the scaling parameter of E_{int}, which penalizes the energy leakage. In Eq. (3.2), E_{ext} is the external energy of a function ϕ, which is defined as follows:

$$E_{ext}(\phi) = \mu L(\phi) + vA_{\Gamma}(\phi), \tag{3.4}$$

where $\mu > 0$ and v are constants, and the terms $L(\phi)$ and $A_{\Gamma}(\phi)$ are defined as:

$$L(\phi) = \int_{\Omega} \delta_{\epsilon}(\phi)|\nabla(\phi)|dxdy, \tag{3.5}$$

$$A_{\Gamma}(\phi) = \int_{\Omega} \Gamma_{\sigma_1,\sigma_2} H_{\epsilon}(-\phi)dxdy, \tag{3.6}$$

UNIVERSITAT ROVIRA I VIRGILI
AVANCES EN SISTEMAS INTERACTIVOS PARA PERSONAS CON PARÁLISIS CEREBRAL
Farhan Akram

where $\Gamma_{\sigma_1,\sigma_2}$ is the difference of Gaussian function, which is used to replace a traditional edge indicator function. In Eqs. (3.5) and. (3.6), $\delta_\epsilon(\phi)$ and $H_\epsilon(\phi)$ are the smooth versions of the Dirac and Heaviside functions, which are defined in Eqs. (2.12) and. (2.10), respectively.

In this chapter, a level-set method based on the difference of Gaussian (DoG) is proposed. A DoG function, which is equivalent to the Mexican Hat function, is a feature enhancement tool that involves the subtraction of a blurred version of an original image from another, less blurred version of the original. As a feature enhancement algorithm, the difference of Gaussian functions can be utilized to increase the visibility of edges and other details present in a digital image. The difference of Gaussian algorithm removes high frequency detail that often includes random noise, thus rendering this approach one of the most suitable for processing images with a high degree of noise. A major drawback of the application of this algorithm is an inherent reduction of the overall image contrast produced by the operation. In this work, it is employed as an edge-detector, which works as a balloon force in the external term of the proposed energy formulation during the level-set curve evolution. Let $I : \Omega \to \mathbf{R}^2$ be an input image. The DoG function $\Gamma_{\sigma_1,\sigma_2}(x)$ is then defined as:

$$\begin{aligned}\Gamma_{\sigma_1,\sigma_2}(x) = I(x) * \frac{1}{\sigma_1\sqrt{2\pi}} \exp\Big(-\frac{x^2}{2\sigma_1^2}\Big) \\ - I(x) * \frac{1}{\sigma_2\sqrt{2\pi}} \exp\Big(-\frac{x^2}{2\sigma_2^2}\Big),\end{aligned} \tag{3.7}$$

where σ_1 and σ_2 are the standard deviations of the first and second Gaussian kernels, respectively, where $\sigma_1 < \sigma_2$.

Figure 3.1 shows a 1D difference of Gaussian (DoG) function. It shows that the DoG function is zero when the slopes of both Gaussian functions intersect with each other. It helps to extract edges even when the images contain intensity inhomogeneous objects.

Finally, from Eq. (3.2), the proposed energy functional, which uses the difference

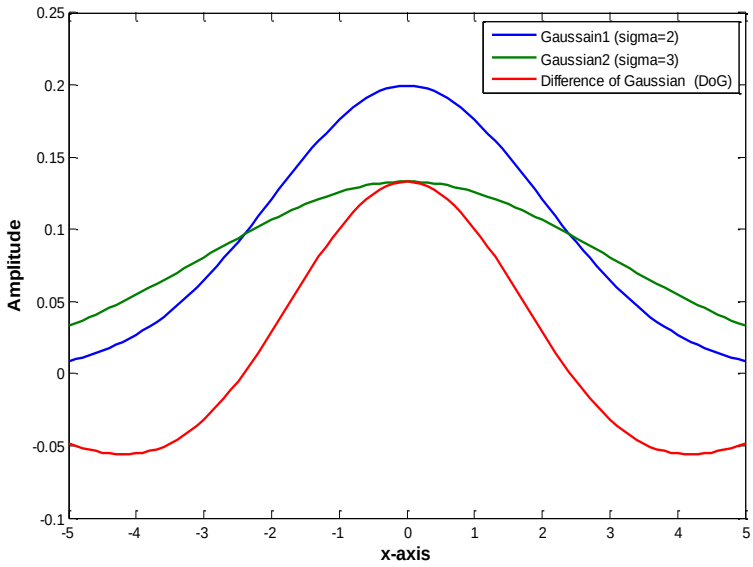

Figure 3.1: 1D difference of Gaussian (DoG) function.

of Gaussian (DoG) function $\Gamma_{\sigma_1,\sigma_2}(x)$ to extract edge information, is defined as:

$$E(\phi) = v \int_{\Omega} \Gamma_{\sigma_1,\sigma_2}(x) H_\epsilon(-\phi) dx + \mu \int_{\Omega} |\nabla H_\epsilon(\phi)| dx + \alpha \int_{\Omega} \frac{1}{2} \big(|\nabla\phi| - 1\big)^2 dx, \tag{3.8}$$

In the above equation, the first term detects the edges using the DoG function. The second term regularizes the region and the third term penalizes the energy leakage. The first variation of the Gateaux derivative (Evans, 1998) of the functional E is denoted by $\frac{\partial E}{\partial \phi}$, which has the following relationship with the evolution equation:

$$\frac{\partial \phi}{\partial t} = -\frac{\partial E}{\partial \phi}, \tag{3.9}$$

The above equation is the gradient descent flow that minimizes the energy functional E. For a particular functional $E(\phi)$ explicitly defined in terms of ϕ, the Gateaux derivative can be computed and expressed in terms of function ϕ and its derivatives (Evans, 1998).

By calculus of variations (Evans, 1998), the Gateaux derivative (first variation)

UNIVERSITAT ROVIRA I VIRGILI
AVANCES EN SISTEMAS INTERACTIVOS PARA PERSONAS CON PARÁLISIS CEREBRAL
Farhan Akram

of the functional E in Eq. (3.8) can be written as:

$$\frac{\partial E}{\partial \phi} = -\Big(v\Gamma_{\sigma_1,\sigma_2} + \mu\,\mathrm{div}\Big(\frac{\nabla\phi}{|\nabla\phi|}\Big)\Big)\delta_\epsilon(\phi) + \alpha\Big[\Delta\phi - \mathrm{div}\Big(\frac{\nabla\phi}{|\nabla\phi|}\Big)\Big], \tag{3.10}$$

where ∇ is the Laplacian operator. Therefore, the function ϕ that minimizes this functional satisfies the Euler-Lagrange equation $-\frac{\partial E}{\partial \phi} = 0$. The steepest descent process for minimization of the functional E yields the following gradient flow:

$$\frac{\partial \phi}{\partial t} = \Big(v\Gamma_{\sigma_1,\sigma_2} + \mu\,\mathrm{div}\Big(\frac{\nabla\phi}{|\nabla\phi|}\Big)\Big)\delta_\epsilon(\phi) + \alpha\Big[\Delta\phi - \mathrm{div}\Big(\frac{\nabla\phi}{|\nabla\phi|}\Big)\Big], \tag{3.11}$$

In this chapter, the spatial partial derivatives $\frac{\partial\phi}{\partial x}$ and $\frac{\partial\phi}{\partial y}$ are approximated by the central difference. The approximation of Eq. (3.11) using a central difference scheme can be written as:

$$\frac{\phi_{i,j}^{k+1} - \phi_{i,j}^{k}}{\tau} = \xi(\phi_{i,j}^{k}) \tag{3.12}$$

where $\xi(\phi_{i,j}^{k})$ is the approximation of the right hand side in Eq. (3.11) by the above difference scheme. The difference equation in (3.12) can be expressed as the following iteration:

$$\phi_{i,j}^{k+1} = \phi_{i,j}^{k} + \tau\xi(\phi_{i,j}^{k}) \tag{3.13}$$

where τ is the time step used in the above numerical implementations. There is a close relation between the time step and the scaling parameter of the energy penalization term i.e., $\tau \times \alpha \leq 0.2$.

In level-set methods, it is essential to initialize the level-set function ϕ as a signed distance function (SDF) ϕ_0. If the initial level-set function is significantly different from the SDF, re-initialization schemes are unable to re-initialize the function to the SDF. In the proposed formulation, not only is the re-initialization procedure completely eliminated, but the level-set function ϕ no longer needs to be initialized as an SDF. The initial level-set function ϕ_0 is defined as:

$$\phi(x, t=0) = \begin{cases} -\rho, & x \in \Omega_0 - \partial\Omega_0 \\ 0, & x \in \partial\Omega_0 \\ \rho, & x \in \Omega - \Omega_0 \end{cases} \tag{3.14}$$

In Eq. (3.14), $\rho > 0$ is a constant ($\rho = 1$ in this work) and $t = 0$ define the initial condition of the level-set function $\phi_0 = \phi(x, t = 0)$. Ω_0 is the inner region of the initial level-set ϕ_0, Ω is the image domain and $\partial\Omega_0$ the boundary of level set ϕ.

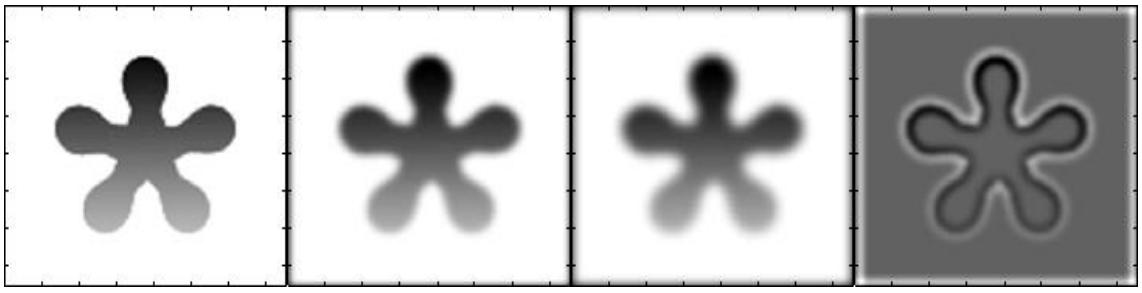

(a) (b) (c) (d)

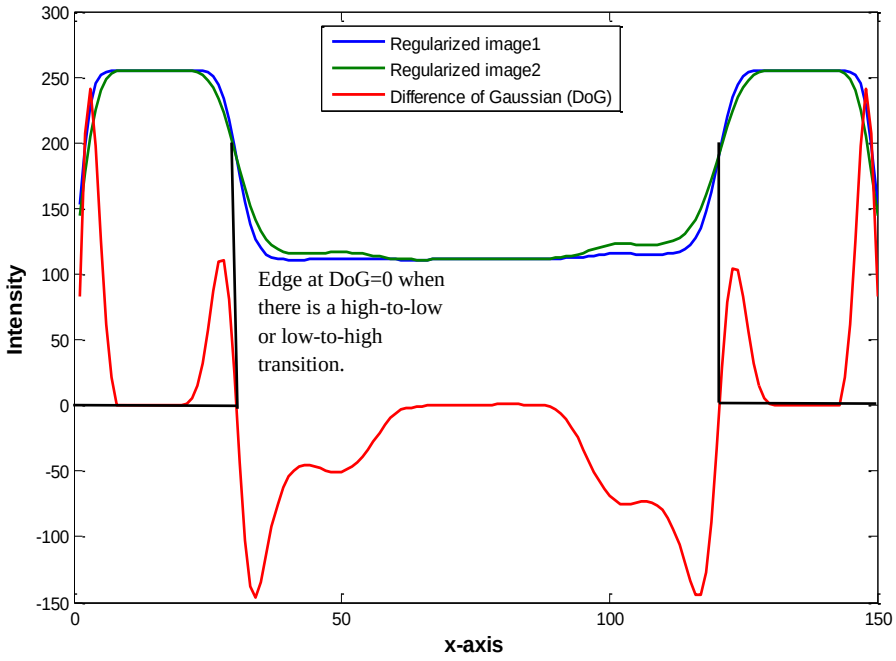

(e)

Figure 3.2: DoG of the middle slice of the flower image. (a) Original image, (b) Gaussian regularized image ($\sigma = 2$), (c) Gaussian regularized image ($\sigma = 3$), (d) Difference of Gaussian regularized images (DoG), and (e) middle profile comparison of (b)-(d).

Figure 3.2 shows a one-dimensional (1D) profile from the middle column of the difference of Gaussian regularized image shown in figure 3.2(d). Figure 3.2(b) and (c)

UNIVERSITAT ROVIRA I VIRGILI
AVANCES EN SISTEMAS INTERACTIVOS PARA PERSONAS CON PARÁLISIS CEREBRAL
Farhan Akram

are Gaussian regularized images, which are subtracted to produce the DoG based edge profile of the given image, as shown in figure 3.2(d). Figure 3.2(e) shows a middle profile comparison between figure 3.2(b)-(d). It shows that when there is an intersection between the 1D middle profile of figure 3.2(b) and (c), then the edge is detected (a transition from high to low or vice versa), which is shown with the red line in Figure 3.2(e).

3.3 Results

In this section, segmentation results using both synthetic and real images are discussed. The proposed method is implemented using MATLAB and run on a 3.4 GHz Intel Core-i7 with 16 GB of RAM, testing it on both synthetic images and real brain magnetic resonance (MR) images of 250×250 pixels with 256 grey levels (8bpp). The parameters used in all experiments in this section are: $\mu = 0.001 \times 255^2$, $v = -40$, $\sigma_1 = 1$, $\sigma_2 = 2$, $\alpha = 1.0$, $\epsilon = 1$ and the time step $\tau = 0.1$.

Figure 3.3 shows segmentation results of different state-of-the-art methods using a flower image with different contrast variations until the flower object becomes inhomogeneous with respect to the image background. It shows that the DRLS method is able to properly segment images in the first four rows, but it is unable to segment the image in the last column. In turn, the CV method is able to properly segment the images in the first two rows and fails to properly segment the remaining images. Although the RSF method is able to segment objects in all images, the petals of the flowers in the images of the last two rows are not properly segmented. In turn, the qualitative comparison shows that the proposed method yields the best segmentation result for all the objects.

Table 3.1 shows a CPU time comparison among the evaluated methods tested in figure 3.3. For the images in the first and second rows, the CV method is the fastest among all segmentation algorithms. In turn, the proposed method is the fastest for the images in the last three rows.

Figure 3.4 shows that the DLSR method could segment the first three images

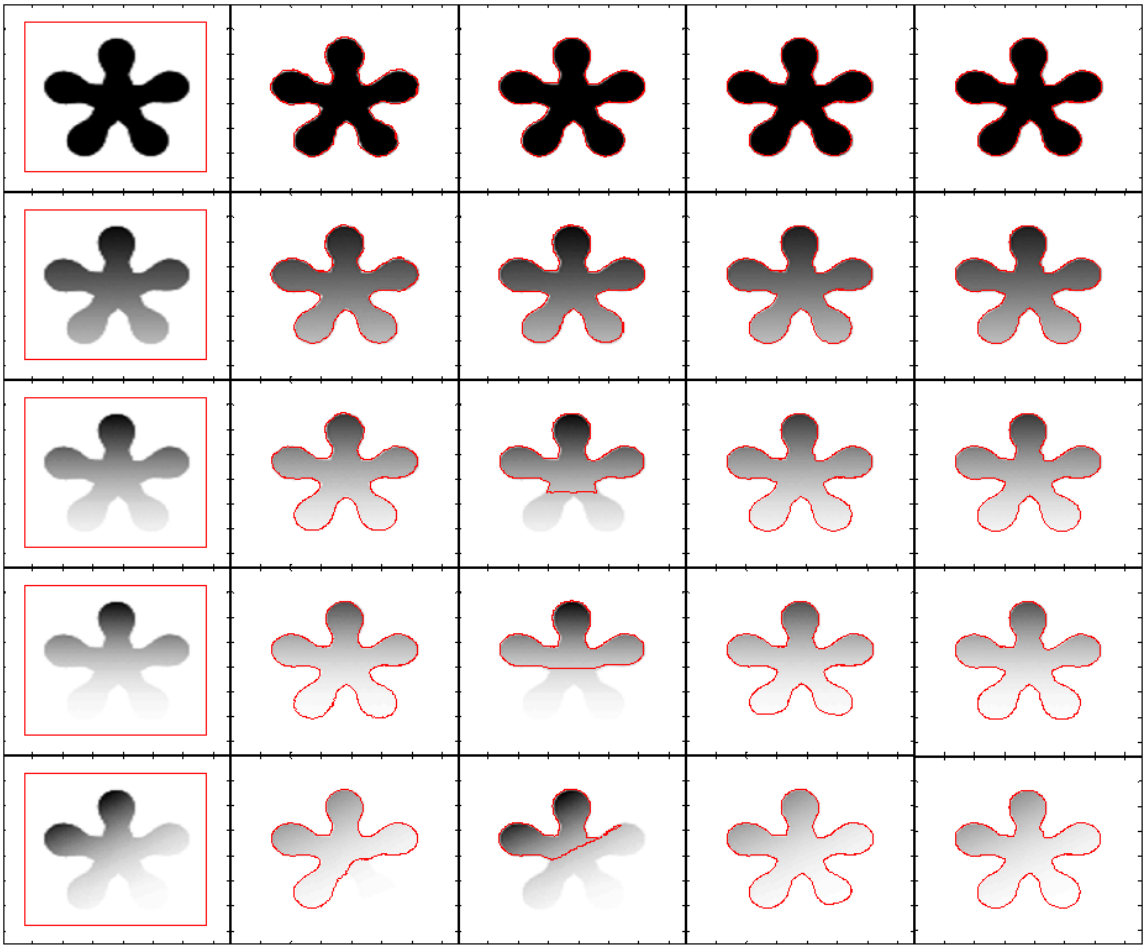

(a) (b) (c) (d) (e)

Figure 3.3: Segmentation of a flower object using different contrast variations (from homogeneous to inhomogeneous). (a) Initial contour, (b) DRLS, (c) CV, (d) RSF, (e) Proposed method.

properly. The CV method could not properly segment the objects in all of the images. The RSF method could segment the first two images and the last properly. However, in the last image, the final contour has missed some details of the small objects enclosed in the main object. Moreover, some details of the big object in the right corner are also missed. In turn, the proposed method yielded the best segmentation results for all of the images.

Table 3.2 shows a CPU time comparison among the evaluated methods tested in figure 3.4. It shows that the CV method is the fastest among all segmentation algorithms for the images in the first and the last rows. For the second and fourth images, the proposed method is the fastest. In turn, for the image in the third row, the DRLS method is the fastest.

Table 3.1: CPU time comparison among the state-of-the-art methods shown in figure 3.3.

Row number	DRLS		CV		RSF		Proposed	
	Iterations	CPU time (s)	Iterations	CPU time (s)	Iterations	CPU time (s)	Iterations	CPU time (s)
1	500	5.45	20	**0.80**	200	6.81	140	1.44
2	500	4.79	20	**0.81**	250	8.45	140	1.38
3	500	4.83	1500	12.61	300	10.38	140	**1.40**
4	1300	13.66	1200	10.09	300	9.81	140	**1.39**
5	900	8.77	2500	20.30	550	17.38	200	**1.97**

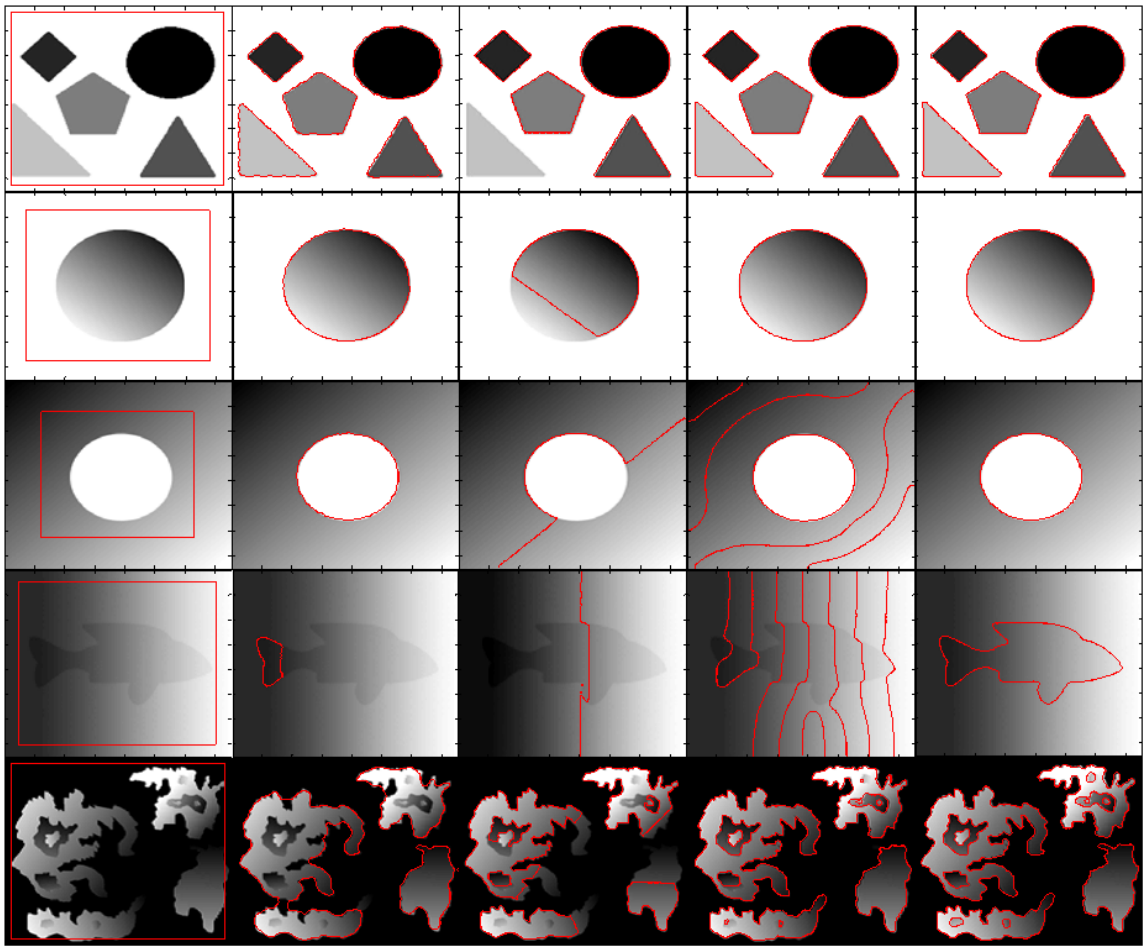

(a) (b) (c) (d) (e)

Figure 3.4: Image segmentation with different types of intensity inhomogeneity (from homogeneous to inhomogeneous). (a) Initial contour, (b) DRLS, (c) CV, (d) RSF, and (e) Proposed method.

Figure 3.5 shows that only the proposed method and LGFIM (Akram et al., 2017) are able to accurately segment all of the intensity inhomogeneous objects. LIF and LSACM are also able to segment all the objects. However, for both methods, the level-set curve around the boundaries of the objects is not quite smooth, which

Table 3.2: CPU time comparison among the state-of-the-art methods shown in figure 3.4.

Row number	DRLS		CV		RSF		Proposed	
	Iterations	CPU time (s)	Iterations	CPU time (s)	Iterations	CPU time (s)	Iterations	CPU time (s)
1	400	4.83	20	**0.88**	100	3.81	240	2.87
2	200	2.28	500	4.77	200	3.59	80	**1.08**
3	200	**2.16**	500	4.97	300	6.31	400	3.73
4	1100	13.3	500	4.83	500	10.64	350	**3.59**
5	1200	22.78	500	**5.42**	300	6.44	350	5.73

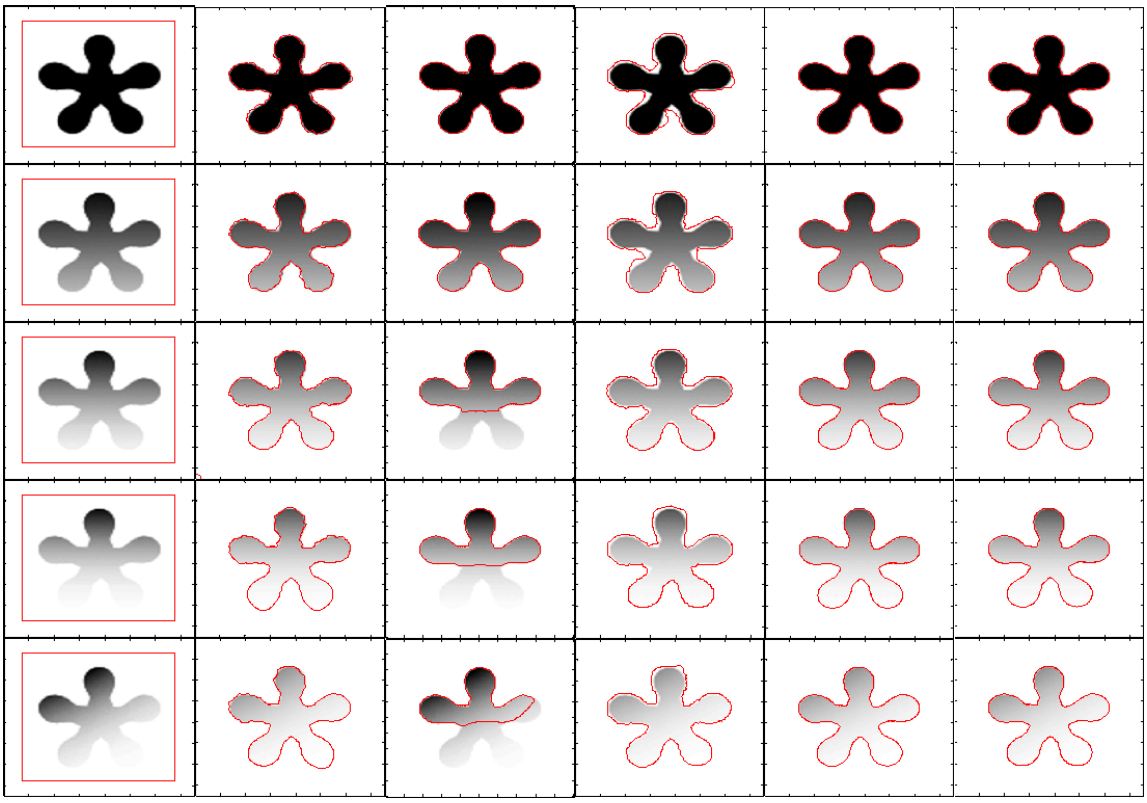

(a) (b) (c) (d) (e) (f)

Figure 3.5: Image segmentation with different types of intensity inhomogeneity (from homogeneous to inhomogeneous). (a) Initial contour, (b) LIF, (c) VLSBCS, (d) LSACM, (e) LGFIM, and (f) Proposed method.

results in information loss. In turn, the VLSBCS method is able to properly segment the images in the first two rows and fails in the last three rows.

Table 3.3 shows a CPU time comparison between the evaluated local active contour methods shown in figure 3.5. For all images, the proposed method yields the lowest CPU time.

In figure 3.6, two images with and without noise are used to show the segmentation capability of the proposed method in the presence of noise. The

UNIVERSITAT ROVIRA I VIRGILI
AVANCES EN SISTEMAS INTERACTIVOS PARA PERSONAS CON PARÁLISIS CEREBRAL
Farhan Akram

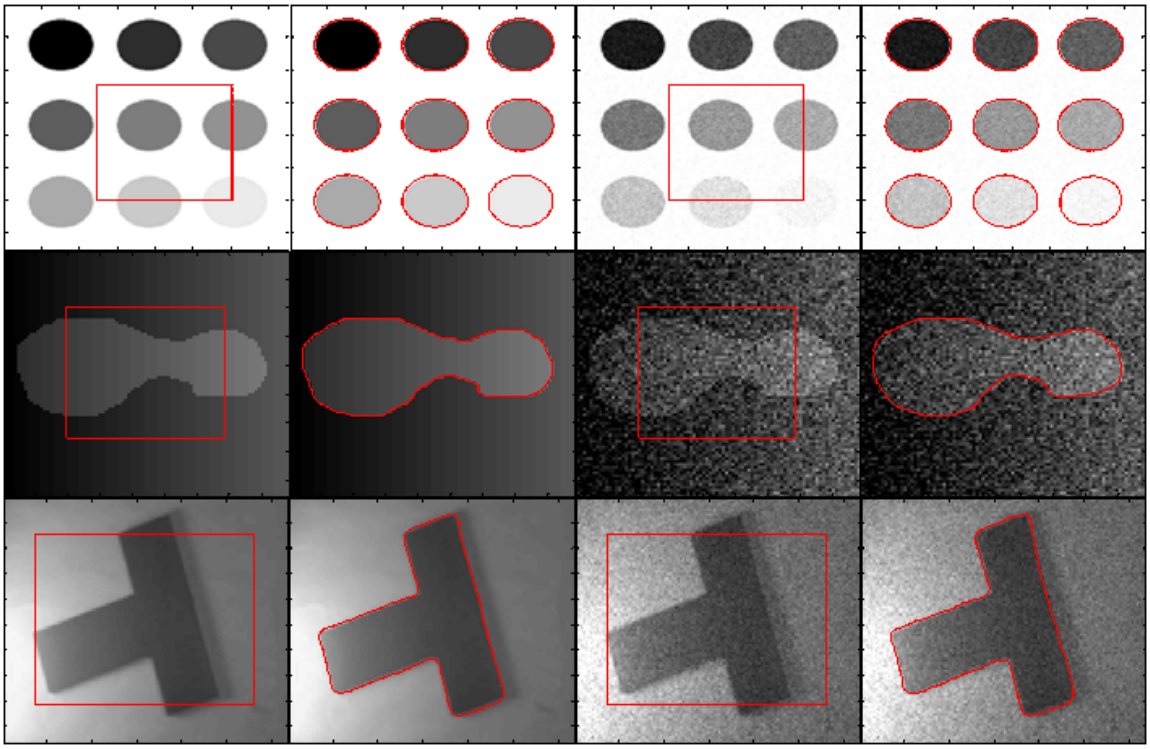

(a) (b) (c) (d)

Figure 3.6: Segmentation results of real and noisy images using the proposed method. (a) and (c) Initial contour, (b) and (d) Final contour.

Table 3.3: CPU time comparison with the local active contour methods shown in figure 3.5.

Row number	LIF		VLSBCS		LSACM		LGFIM		Proposed	
	Iterations	CPU time (s)	Iterations	CPU time (s)	Iterations	CPU time (s)	Iterations	CPU time (s)	Iterations	CPU time (s)
1	400	5.45	20	1.71	40	24.69	20	1.58	140	**1.44**
2	450	5.97	30	2.21	40	25.55	30	2.19	140	**1.38**
3	600	7.56	30	2.27	50	32.05	70	4.12	140	**1.40**
4	2000	57.38	100	5.87	60	38.69	90	5.09	140	**1.39**
5	2000	55.91	100	6.31	80	50.72	100	5.78	200	**1.97**

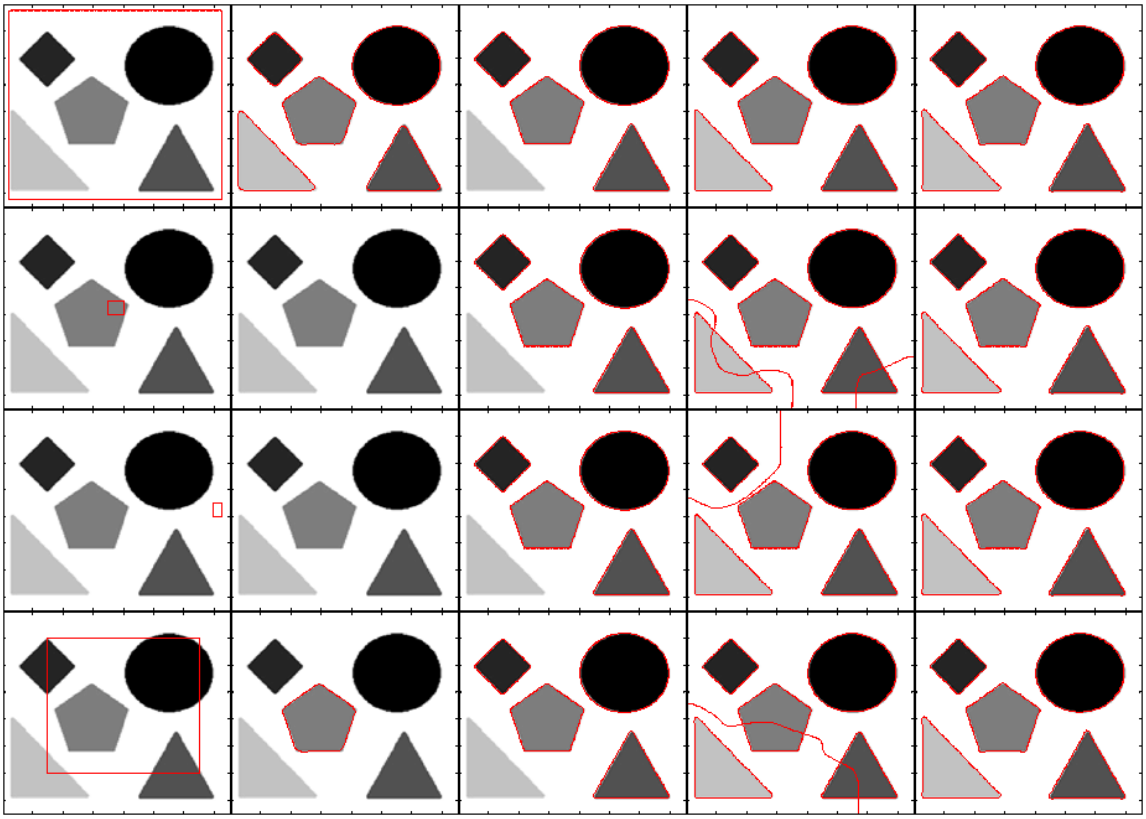

(a) (b) (c) (d) (e)

Figure 3.7: Effects of initial contour on final segmentation. (a) Initial contour, (b) DRLS, (c) CV, (d) RSF, and (e) Proposed method.

proposed method is not affected by the presence of noise. It is able to properly segment the object both with and without background noise.

Figure 3.7 shows the impact of the position of the initial contour on the evaluated methods. The segmentation results produced by the proposed method are not affected by the initial position of the contour, unlike the other evaluated methods, which are sensitive to the initial contour.

Figures 3.8 and 3.9 show the brain MR image segmentation problem using the evaluated methods. The proposed method yields the best segmentation. Figure 3.8 shows that RSF and the proposed method are able to segment the detailed anatomical structure of the brain region, whereas the remaining methods fail to do so. In figure 3.9, RSF, CV and the proposed method are able to segment the detailed structure of the brain. In turn, the DRLS method fails to do so.

UNIVERSITAT ROVIRA I VIRGILI
AVANCES EN SISTEMAS INTERACTIVOS PARA PERSONAS CON PARÁLISIS CEREBRAL
Farhan Akram

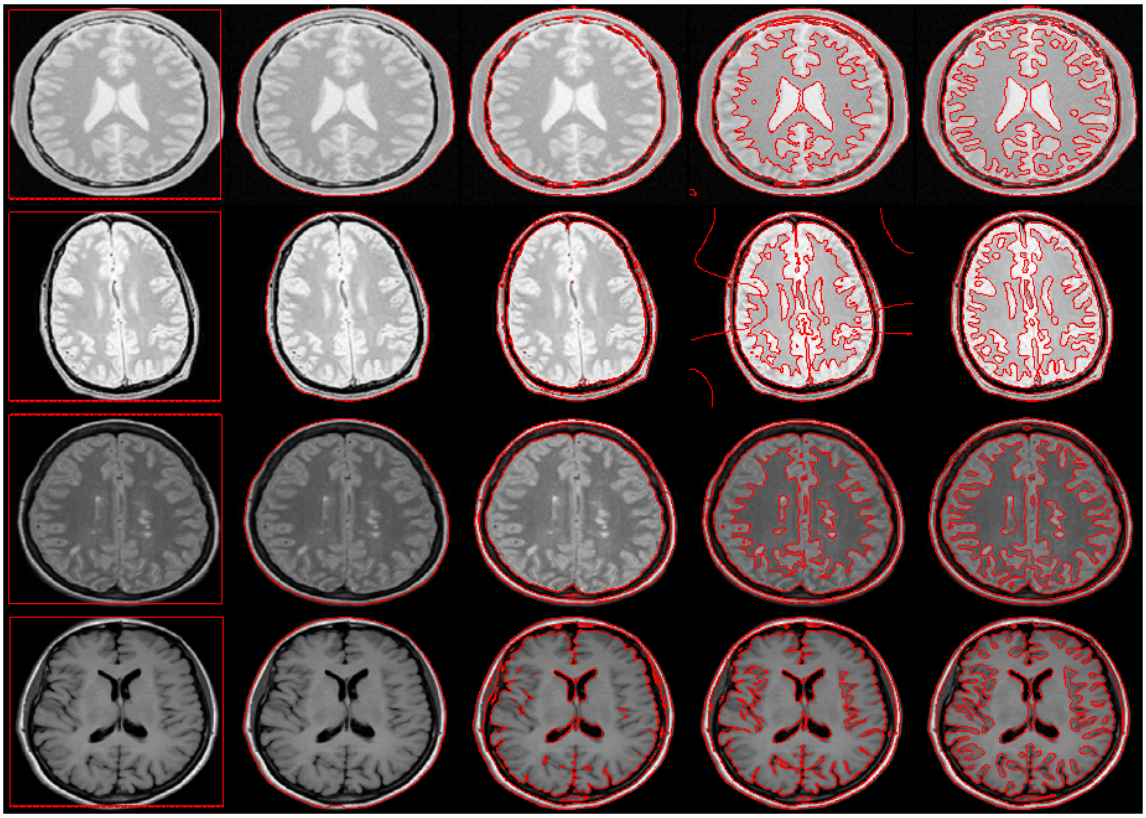

(a) (b) (c) (d) (e)

Figure 3.8: Brain MR image segmentation comparison with the state-of-the-art. (a) Initial contour, (b) DRLS, (c) CV, (d) RSF, (e) Proposed method.

3.4 Quantitative analysis

In this section, the proposed method is quantitatively compared with the alternative state-of-the-art methods. Several metrics are used to evaluate the binary segmentation of a structure in an image. Let G be the ground truth of the region of interest and S the segmented region in the given image $I : \Omega \rightarrow \mathbf{R}^2$. The true positive (TP) set is defined as $TP = G \cap S$, which is the set of the segmented region common in both G and S. The true negative (TN) set is defined as $TN = \overline{G} \cap \overline{S}$, which is the set of image background common in both G and S. Similarly, the false positive (FP) set is defined as $FP = \overline{G} \cap S$, which is the false object segmented as region of interest not belonging to set G. In turn, the false negative (FN) is defined as $FN = G \cap \overline{S}$, which is the region of interest missed by the proposed method during the segmentation process.

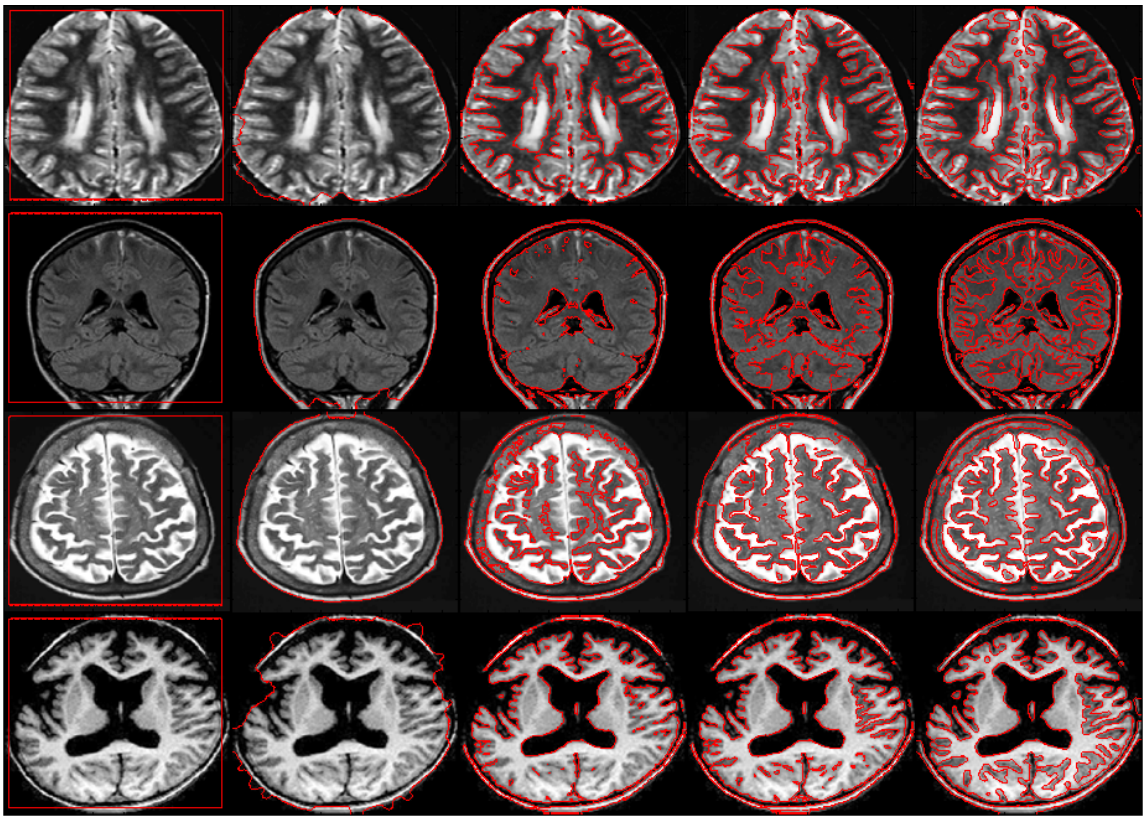

(a) (b) (c) (d) (e)

Figure 3.9: Brain MR image segmentation comparison with the state-of-the-art. (a) Initial contour, (b) DRLS, (c) CV, (d) RSF, (e) Proposed method.

From the above subsets, different similarity metrics are computed. In particular, the Jaccard index (JI) (Jaccard, 1912), the Dice similarity coefficient (DSC) (Dice, 1945) and the Matthews correlation coefficient (MCC) (Matthews, 1975) are frequently used in set comparison, that is, to compute the segmentation accuracy when the ground truth of the region of interest is available. In this chapter, the three set similarity metrics (JI, DSC and MCC) are computed for the quantitative analysis. They are defined as:

$$JI = \frac{TP}{TP + FP + FN}, \quad DSC = \frac{TP}{\frac{1}{2}(TP + FN + TP + FP)},$$
$$MCC = \frac{(TP \times TN) - (FP \times FN)}{\sqrt{(TP + FP)(TP + FN)(TN + FP)(TN + FN)}} \tag{3.15}$$

For the maximum segmentation accuracy, the values of JI, DSC and MCC should

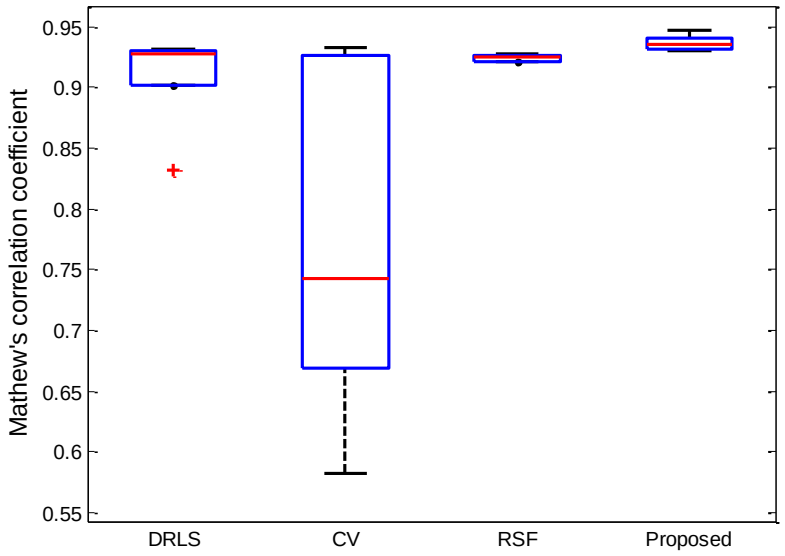

(a)

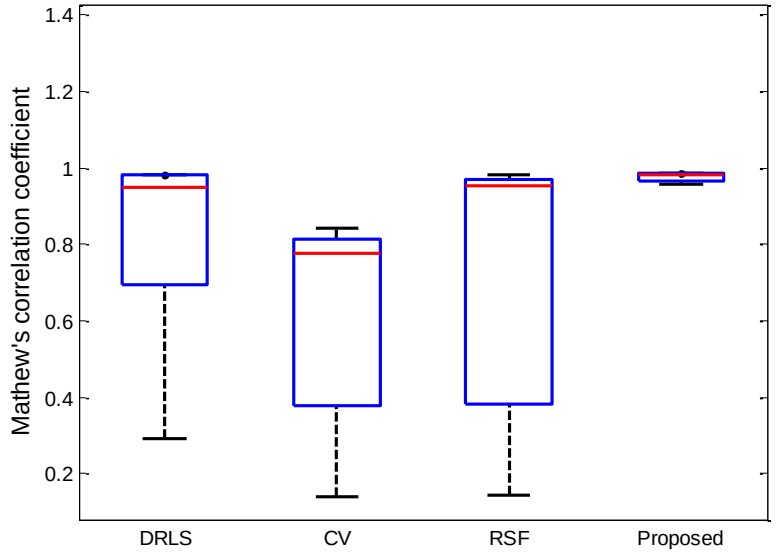

(b)

Figure 3.10: Accuracy plot for Fig. 3.3 and 3.4 using the Matthews correlation coefficient. (a) Box plot of Fig. 3.3. (b) Box plot of Fig. 3.4.

be close to 1 (ideally 1). The Hausdorff distance (HD) (Huttenlocher et al., 1993) is another similarity metric, which is used to compute the accuracy between two sets. It provides a symmetric distance measure of the maximal discrepancy between two labelled contours and is defined as:

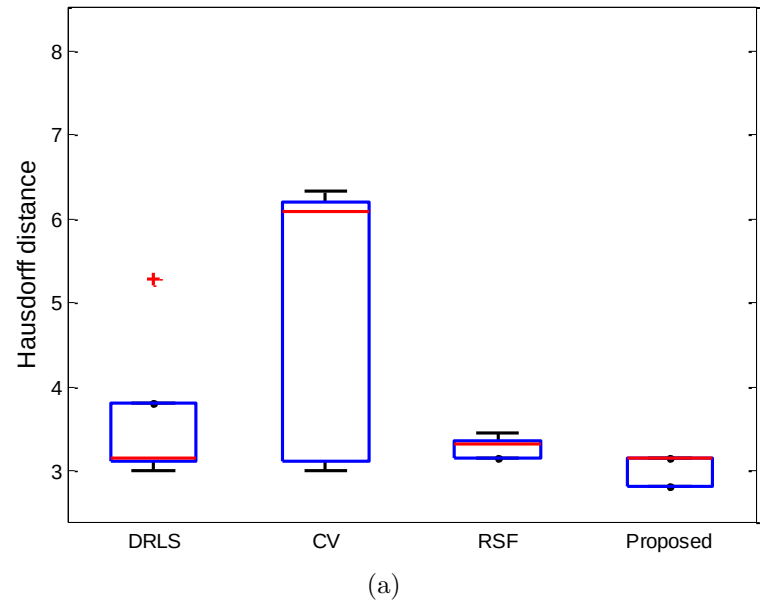

(a)

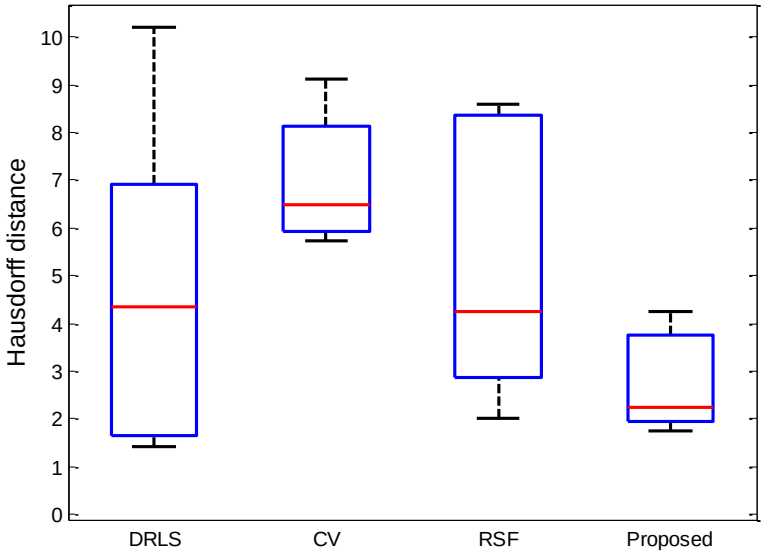

(b)

Figure 3.11: Accuracy plot for Fig. 3.3 and 3.4 using the Haursdorff distance. (a) Box plot of Fig. 3.3. (b) Box plot of Fig. 3.4.

$$HD(G,S) = \max\Big(\max_{g\in G}\big(\min_{s\in S} d(g,s)\big), \max_{s\in S}\big(\min_{g\in G} d(g,s)\big)\Big) \tag{3.16}$$

where G and S are the ground truth and computed contours, respectively, and $d(g,s)$ denotes the Euclidean distance. For the maximum segmentation accuracy, the HD

UNIVERSITAT ROVIRA I VIRGILI
AVANCES EN SISTEMAS INTERACTIVOS PARA PERSONAS CON PARÁLISIS CEREBRAL
Farhan Akram

value should be close to 0 (ideally 0).

Figure 3.10 shows the segmentation accuracy comparison using the Matthews correlation coefficient (MCC) from figures 3.3 and 3.4 in a box plot. The proposed method yields the best segmentation results for both figures 3.3 and 3.4. However, in figure 3.3, RSF yields a similar result compared to the proposed method.

Figure 3.11 shows the segmentation accuracy comparison using the Hausdorff distance (HD) from figure 3.3 and 3.4 in a box plot. It shows that the proposed method yields the smallest HD value for both figures 3.3 and 3.4. Therefore, it yields the best segmentation results.

Table 3.4: Segmentation accuracy analysis comparison using the Jaccard index and Dice similarity coefficient similarity metrics.

Figure	**Jaccard index (JI)**				**Dice similarity coefficient (DSC)**			
	DRLS	**CV**	**RSF**	**Proposed**	**DRLS**	**CV**	**RSF**	**Proposed**
4	0.965 ±0.007	0.918 ±0.023	0.97 ±0.001	**0.974 ±0.002**	0.982 ±0.004	0.957 ±0.012	0.985 ±0	**0.987 ±0.001**
5	0.775 ±0.169	0.612 ±0.145	0.655 ±0.172	**0.943 ±0.016**	0.814 ±0.157	0.715 ±0.125	0.731 ±0.147	**0.971 ±0.009**

Table 3.4 shows the segmentation accuracy comparison of the proposed method with the state-of-the-art using the JI and DSC similarity metrics. Both the mean and standard deviation (mean error) of the evaluated metrics are considered in the result compilation. For figure 3.3, both the proposed method and RSF yield similar values for both JI and DSC. In turn, the proposed method yields the best segmentation result for figure 3.4.

This section also shows segmentation results using 2D brain MR images from a public database of 20 brain anatomical models (Aubert-Broche, 2006). All images have 250×250 pixels and 8 bits per pixel. As a practical application, brain MR images are segmented into white matter (WM) and gray matter (GM) regions, which can be helpful to psychologists to pinpoint psychological diseases and to surgeons during brain surgery.

In order to partition a brain MR image into WM and GM regions, the segmentation result is split into two regions based on two phases: $\phi > 0$ and $\phi < 0$. The WM and GM regions represent the brain region, which is the region of interest, while the regions outside the brain (e.g., skull, fat and vacuum) can be taken as

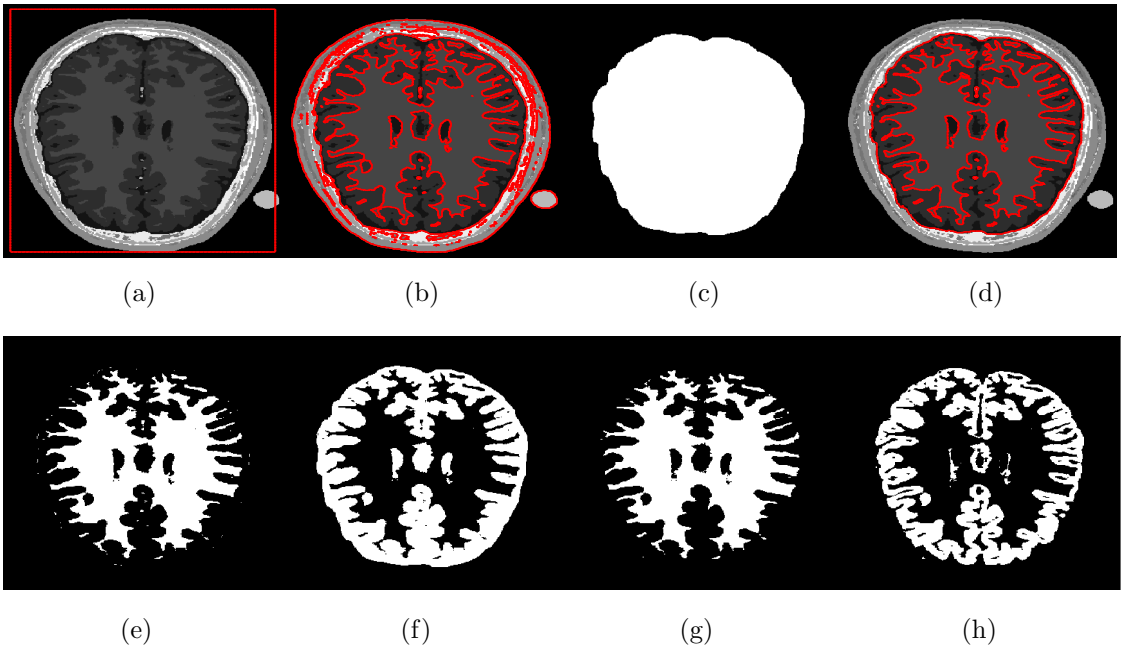

(a) (b) (c) (d)

(e) (f) (g) (h)

Figure 3.12: WM and GM regions computed with the proposed method and their respective ground truths. (a) Initial contour, (b) Final contour, (c) Brain mask, (d) Masked contour, (e) Computed WM, (f) Computed GM, (g) WM ground truth, and (h) GM ground truth.

irrelevant regions. Therefore, we manually extracted the brain area to segment the WM and GM regions, removing the other irrelevant regions out of second row, the third and fourth images show the ground truths of the WM and GM regions, respectively.

Figure 3.12 shows the accuracy analysis of the region of interest in the brain MR images. A total of 100 2D slices from 20 brain anatomical models (Aubert-Broche, 2006) were used. Five 2D slices from every patient were considered. The WM and GM regions for all methods were computed as depicted in figure 3.12. The segmentation accuracy corresponding to the WM and GM regions presented in figure 3.13 was obtained using percentage accuracy in terms of Jaccard index from (3.15).

Table 3.5: Segmentation accuracy of WM and GM regions (in terms of Jaccard index×100) using VLSBCS, LSACM and proposed methods.

Regions	VLSBCS	LSACM	Proposed
WM	87.32 ± 1.60	53.82 ± 1.01	**91.28 ± 0.33**
GM	66.04 ± 2.16	71.63 ± 1.53	**72.89 ± 0.88**

Figure 3.13 and Table 3.5 show that the proposed method yields the best

UNIVERSITAT ROVIRA I VIRGILI
AVANCES EN SISTEMAS INTERACTIVOS PARA PERSONAS CON PARÁLISIS CEREBRAL
Farhan Akram

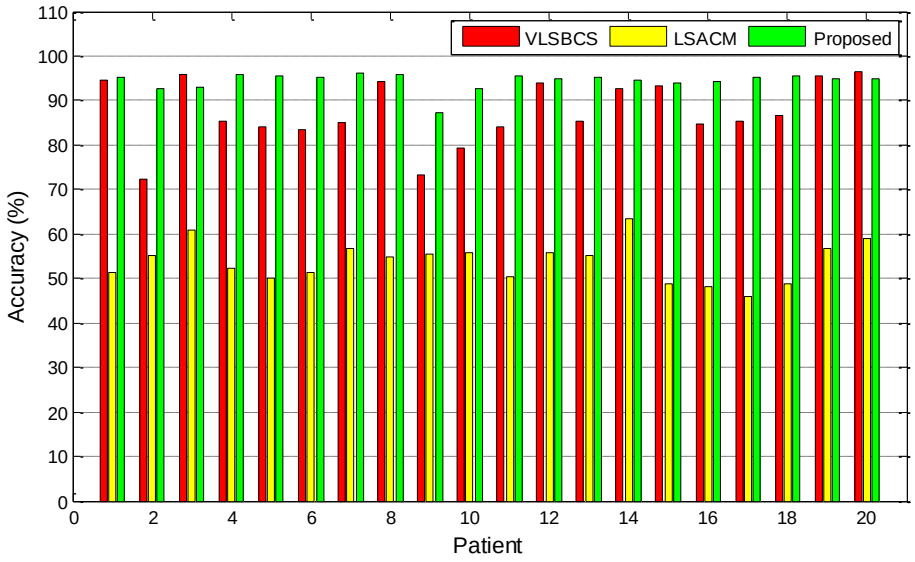

(a)

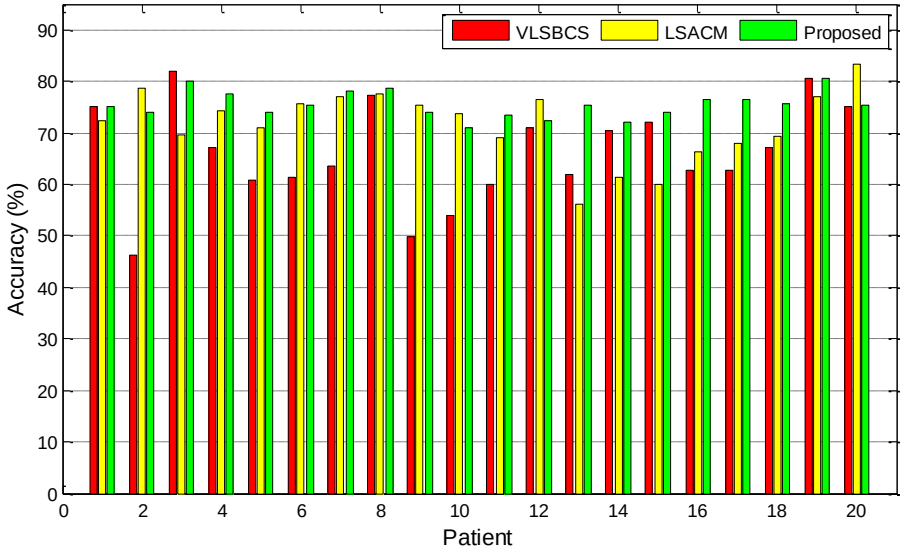

(b)

Figure 3.13: Segmentation accuracy analysis of (a) WM, and (b) GM regions using two-phase active contours.

segmentation accuracy in most cases for both the WM and GM regions.

3.5 Summary

In this chapter, a level-set method is proposed based on the use of a difference of Gaussians (DoG) function as an edge indicator in its formulation. The DoG function

utilizes differences of two smooth images to extract edge information in an image. The proposed method uses this edge information as a balloon force to evolve the level-set curve. A Gaussian kernel is also used to regularize the level-set after each time step, which also removes the computationally expensive re-initialization step.

The inclusion of the DoG function in the level-set formulation acts like a global edge extractor and is able to segment all the regions in an image. Moreover, it is also able to properly segment images with intensity inhomogeneity. The experimental results show that the proposed method yields the best segmentation results using both synthetic and real images as compared to the alternative state-of-the-art methods that have been evaluated.

UNIVERSITAT ROVIRA I VIRGILI
AVANCES EN SISTEMAS INTERACTIVOS PARA PERSONAS CON PARÁLISIS CEREBRAL
Farhan Akram

CHAPTER 4

Image segmentation using active contours driven by bias fitted image robust to intensity inhomogeneity

4.1 Introduction

Intensity inhomogeneity is one of the well-known problems in image segmentation, which can substantially reduce the accuracy of intensity based segmentation methods. It manifests as a smooth intensity variation across the image that complicates the segmentation of the objects contained in it.

The techniques that aim to avoid intensity inhomogeneity in the image acquisition process are known as *prospective methods*. They are only capable of correcting

UNIVERSITAT ROVIRA I VIRGILI
AVANCES EN SISTEMAS INTERACTIVOS PARA PERSONAS CON PARÁLISIS CEREBRAL
Farhan Akram

intensity inhomogeneity caused by the imaging device, not being able to segment the objects affected by intensity inhomogeneity.

On the other hand, techniques that can correct an image and also segment the objects affected by intensity inhomogeneity are called *retrospective methods*. Retrospective methods are further classified according to the image segmentation method they apply into: filtering methods (Lewis and Fox, 2004), surface fitting methods (Vokurka et al., 1999), histogram-based methods (Vovk et al., 2006), and active contours (Li et al., 2008a, 2011; Zhang et al., 2015, 2016). Segmentation-based methods (Li et al., 2011; Zhang et al., 2016) are the most versatile, since they unify segmentation and bias correction in a single framework.

Active contours are retrospective methods suitable for both image segmentation and bias correction (Li et al., 2011; Zhang et al., 2016). The first active contour method was proposed by Kass et al. (1988) in order to segment an image by evolving a curve towards the boundaries of an object contained in the image. An energy functional is first defined by using image statistics, curvature and gradient information. The curve is evolved by minimizing that energy functional. Active contour methods can be categorized into edge-based (Kass et al., 1988; Caselles et al., 1997) and region-based (Mumford and Shah, 1989; Chan and Vese, 2001) methods.

Edge-based active contour methods typically use image gradient information to define an inflating balloon force that is used in the curve evolution process (Caselles et al., 1997). However, they are unable to segment images with intense noise and weak edges. Alternatively, region-based active contour methods use statistical and curvature information from the image in the formulation of the energy functional. Mumford and Shah (1989) devised a global region-based active contour method by assuming image homogeneity. Thus, traditional active contour methods based on Mumford and Shah (1989) model, such as the *active contours without edges* (ACWE) method (Chan and Vese, 2001), cannot segment images with intensity inhomogeneity.

A region-based active contour model in the context of intensity inhomogeneous

image segmentation was proposed by Li et al. (2008b). A Gaussian kernel is used to compute local intensity means. This model is able to segment images with intensity inhomogeneity, which overcomes the limitation of piecewise constant models (Chan and Vese, 2001). However, it is unable to correct intensity inhomogeneous objects. Moreover, this method is sensitive to the position of the initial contour.

A variational level-set approach for bias correction and segmentation (VLSBCS) for images corrupted with intensity inhomogeneity was proposed by Li et al. (2008a, 2011). The computed bias field is intrinsically ensured to be smooth by the data term in the variational formulation, without any additional effect to maintain the smoothness of the bias field. A local statistical active contour model (LSACM) for image segmentation in the presence of intensity inhomogeneity was proposed by Zhang et al. (2015, 2016). In this work, the inhomogeneous objects are modelled as Gaussian distributions of different means and variances. A statistical energy functional is then defined for each local region, which combines the bias field, the level-set function, and the constant approximating the true signal of the corresponding object. Both methods are able to segment and correct intensity inhomogeneous images. However, they are also sensitive to the initial position of the contours and have a high computational complexity.

In this chapter, a novel region-based active contour model is proposed by introducing a phase stretch transform (PST) kernel in the energy functional. The proposed method is formulated to both correct and segment intensity inhomogeneous regions. The response of the PST kernel also behaves as a smooth intensity variation, which is a good model to approximate the bias field. New image intensity means and bias terms are computed after the integration of the PST kernel, which improves both the segmentation and bias correction results. A bias signed pressure force (bSPF) function is also proposed to stabilize the gradient descent solution. Both qualitative and quantitative comparisons with the state-of-the-art methods show that the proposed method yields better results.

The rest of the chapter is organized as follows. The proposed methodology is presented in section 4.2. Segmentation results are compared with the state-of-the-art

methods both qualitatively and quantitatively in section 4.3. Finally, the chapter is summarized in section 4.4.

4.2 Proposed method

Generally, it is assumed that an intensity inhomogeneity is a smooth spatially varying function that alters image intensities that otherwise would be constant for a same object regardless its position in an image. In its simplest form, the model assumes that intensity inhomogeneity is multiplicative or additive, that is, the intensity inhomogeneity field multiplies or adds to the image intensities. In this work, a multiplicative model has been considered for the bias field estimation. Let $I : \Omega \rightarrow \mathbf{R}^2$ be the input image with intensity inhomogeneity, $J(x)$ the restored image without intensity inhomogeneity, $b(x)$ the bias field approximated with a Gaussian distribution, and $n(x)$ additive noise. A given image I can then be approximated by using the following definition:

$$I(x) = b(x)J(x) + n(x), \tag{4.1}$$

If m_i are intensity means computed for the piecewise regions $\left\{\Omega_i\right\}_{i=1}^{N}$ and M_i is the characteristic function of every region, then J is constituted by i piecewise components, $J = m_1M_1 + m_2M_2 + ...m_iM_i$. In order to segment intensity inhomogeneous images, the following energy functional E_{PST} is defined:

$$E_{PST}(\phi) = \lambda E_{bFI}(\phi) + vA(\phi), \tag{4.2}$$

where λ and v are scaling constants. $A(\phi)$ is the area term that smoothes the level-set curve to speed up the curve evolution. It is defined as:

$$A(\phi) = \int_{\Omega} H_{\epsilon}(-\phi)dxdy, \tag{4.3}$$

where $H_\epsilon(\phi)$ is the regularized version of the Heaviside function, which is defined in Eq. (2.10). In Eq. (4.2), E_{bFI} is the proposed energy function based on a biased fitted image, which is defined as:

$$E_{bFI}(\phi) = \frac{1}{2}\int_{\Omega} \big|I(x) - I_{bFI}(x)\big|^2 dx, \tag{4.4}$$

where I_{bFI} is the bias fitted image defined as:

$$I_{bFI}(x) = b(x)\big(m_1 M_1(\phi) + m_2 M_2(\phi)\big), \qquad x \in \Omega \tag{4.5}$$

where m_1, m_2 are the local intensity means and $b(x)$ is the bias field, which are defined as:

$$b(x) = \frac{\sum_{i=1}^{2} K_\xi * \big[I(x) m_i M_i(\phi)\big]}{\sum_{i=1}^{2} K_\xi * \big[m_i^2 M_i(\phi)\big]}, \tag{4.6}$$

$$m_i = \frac{\int K_\xi * \big[I(x) b(x) M_i(\phi)\big] dx}{\int K_\xi * \big[b^2(x) M_i(\phi)\big] dx}, \tag{4.7}$$

where M_i is the characteristic function of a given image based on the regularized Heaviside function in Eq. (2.10). When the image domain is partitioned in two regions $\{\Omega_1, \Omega_2\}$, M_i is defined as $M_1 = H_\epsilon(\phi)$ and $M_2 = \big(1 - H_\epsilon(\phi)\big)$. Parameter ξ is the phase stretch transform (PST) kernel proposed by Asghari and Jalali (2015). Let $I(x, y) : \Omega \to \mathbf{R}^2$ be an input image in the Cartesian plane with two dimensional spatial variables x and y. The frequency response of the PST kernel $\xi(u, v)$, with u and v being the two dimensional frequency variables, is then defined as:

$$\xi(u,v) = \xi_{polar}(r,\theta) = \xi_{polar}(r) = \frac{S.W.r.\tan^{-1}(W.r) - \frac{1}{2}log\big(1 + (W.r)^2\big)}{W.r_{max}.\tan^{-1}(W.r_{max}) - \frac{1}{2}log\big(1 + (W.r_{max})^2\big)} \tag{4.8}$$

where $r = \sqrt{u^2 + v^2}$, $\theta = tan^{-1}(u/v)$ and $tan^{-1}(.)$ is the inverse tangent function, $log(.)$ is the natural logarithm and r_{max} is the maximum frequency from r. S and

W are real-valued numbers related to the strength (S) and warp (W) of the phase profile applied to the image, respectively.

In traditional retrospective active contour methods, a Gaussian kernel is used to approximate the bias field to correct the intensity inhomogeneity. Asghari and Jalali (2015) proposed an edge-detection method based on the phase stretch transform (PST). They proposed a new kernel called phase stretch transform (PST) in the polar domain to regularize an image and detect its edges. In this work, the Gaussian kernel from the traditional retrospective active contour method is replaced with a PST kernel to redefine the bias field and the intensity means as shown in Eqs. (4.6) and (4.7).

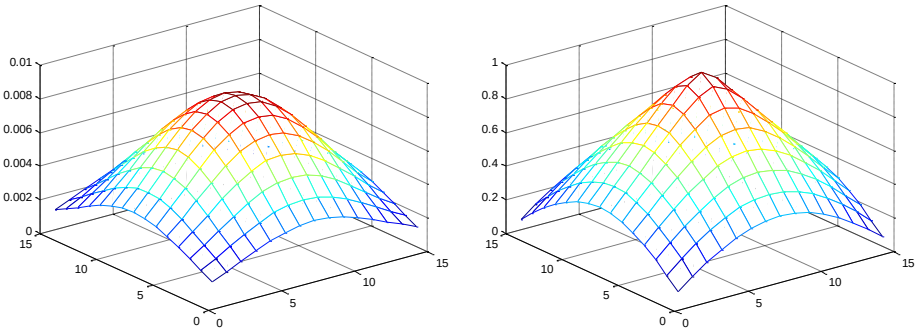

(a) (b)

Figure 4.1: Different kernels used to compute the bias field over the image. (a) Gaussian kernel, and (b) PST kernel.

Figure 4.1 shows a visual comparison between the Gaussian and PST kernels. The sharpness of the PST kernel response is dependent on the warp (W) and strength (S) parameters. If $W > 100$ and $S <= 1$, the PST kernel will yield a sharp distribution. Figure 4.1(b) shows that the PST kernel has sharper top, which plays an important role in successfully detecting edges.

Using the calculus of variations and steepest gradient descent (Aubert and Kornprobst, 2010), E_{PST} in Eq. (4.2) is minimized with respect to ϕ to yield the corresponding gradient descent flow:

$$\frac{\partial \phi}{\partial t} = \Big(\lambda.b(x)\big(I(x) - I_{bFI}(x)\big)\big(m_1 - m_2\big) - v\Big)\delta_\epsilon(\phi), \tag{4.9}$$

where $\delta_\epsilon(\phi)$ is the smooth version of the Dirac function, which is defined in Eq. (2.12).

Parameter $b(x)$ is the bias field defined in Eq. (4.6), and $\{m_1, m_2\}$ are local intensity means defined in Eq. (4.7). The above gradient descent flow is not stable around object boundaries. Moreover, it does not yield proper segmentation when the boundaries between inhomogeneous objects and the background are undistinguishable. $(I - I_{bFI})(m_1 - m_2)$ generates large values that cross a maximum threshold resulting in an unstable contour. Therefore, $(I - I_{bFI})$ is replaced by a new biased signed pressure force (bSPF) function, which normalizes values to $[-1, 1]$ in order to obtain a smooth version of the gradient descent flow:

$$\frac{\partial \phi}{\partial t} = \big(\lambda.b_{SPF}(I)(m_1 - m_2) - v\big)\delta_\epsilon(\phi), \tag{4.10}$$

where the proposed biased SPF function is defined as:

$$b_{SPF}(I) = \begin{cases} \frac{I(x) - I_{bFI}(x)}{\max\left(\left|I(x) - I_{bFI}(x)\right|\right)}, & I(x) \neq 0 \\ 0, & I(x) = 0 \end{cases} \tag{4.11}$$

In level-set methods, it is essential to initialize the level-set function ϕ as a signed distance function (SDF) ϕ_0. In the proposed formulation, not only is the re-initialization procedure completely eliminated, but the level-set function ϕ no longer needs to be initialized as an SDF. The initial level-set function ϕ_0 is defined as:

$$\phi(x, t = 0) = \begin{cases} -\rho, & x \in \Omega_0 - \partial\Omega_0 \\ 0, & x \in \partial\Omega_0 \\ \rho, & x \in \Omega - \Omega_0 \end{cases} \tag{4.12}$$

where $\rho > 0$ is a constant ($\rho = 1$ in this work) and $t = 0$ defines the initial condition

of the level-set function $\phi_0 = \phi(x, t = 0)$. Ω_0 is the inner region of the initial level-set ϕ_0, Ω is the image domain and $\partial\Omega_0$ is the boundary of level-set ϕ.

Finally, A Gaussian kernel G_γ regularizes the level-set function ϕ to remove the need for re-initialization, $\phi = G_\gamma * \phi$, where γ is the standard deviation of the regularizing Gaussian kernel.

4.3 Results

In this section, segmentation results using both synthetic and real images are discussed. The proposed method has been implemented using MATLAB and run on a 3.4 GHz Intel Core-i7 with 16 GB of RAM, testing it on both synthetic images and real brain magnetic resonance (MR) images of 100×100 pixels with 256 grey levels (8bpp). The parameters used in all experiments in this section are: $\lambda = 25$, $v = 3$, $\gamma = 1$, $W = 100$, $S = 1$, $\epsilon = 1$ and time step $\tau = 1$.

Figure 4.2 shows both intensity inhomogeneous image correction and segmentation results of the proposed method using different synthetic images. It shows that it is able to properly segment and correct the intensity inhomogeneous regions.

Figure 4.3 shows segmentation results of different state-of-the-art methods using a flower image with different contrast variations until the flower object becomes inhomogeneous with respect to the image background. It shows that the LSACM method is able to properly segment the images in the first three rows. However, it is unable to properly segment the images in the last two rows. In turn, the VLSBCS method is able to properly segment the images in the first two rows and fails to properly segment the remaining images. The qualitative comparison shows that the proposed method yields the best segmentation results for all the objects.

In figure 4.4, the segmentation and bias correction results using the proposed method (third row) are compared with the ones computed with VLSBCS by Li et al. (2008a, 2011) (first row) and LSACM by Zhang et al. (2015, 2016) (second row) using real brain MR images as a practical application. The proposed method can

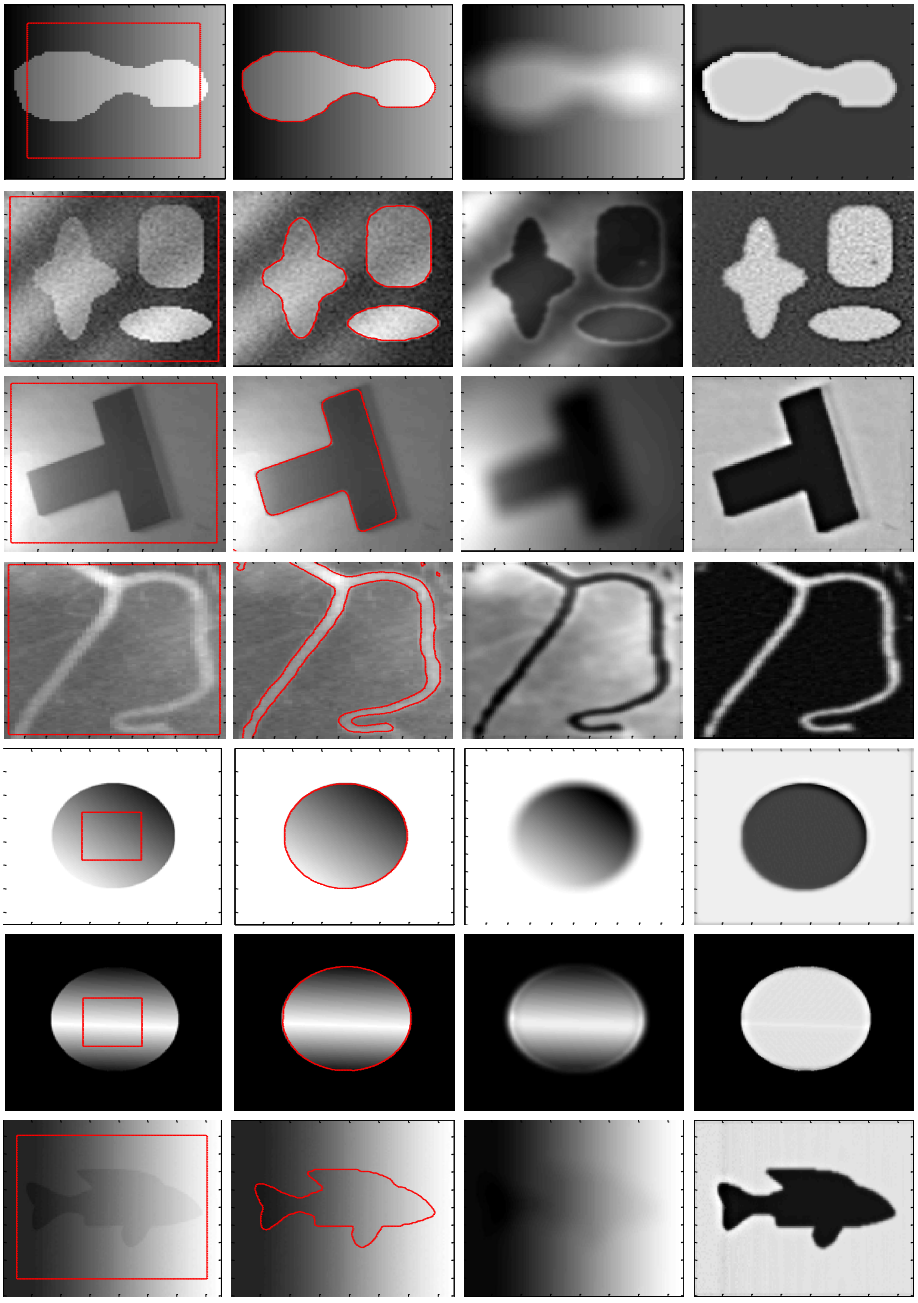

(a) (b) (c) (d)

Figure 4.2: Segmentation flower object using different contrast variations (from homogeneous to inhomogeneous). (a) Initial contour, (b) Final contour, (c) Bias field, and (d) Corrected image.

segment more detailed regions than the other methods. Moreover, the bias-corrected image using the proposed method has more details than the ones computed with the other methods, as highlighted by the red circles.

In figure 4.5, the segmentation results and bias correction using the proposed

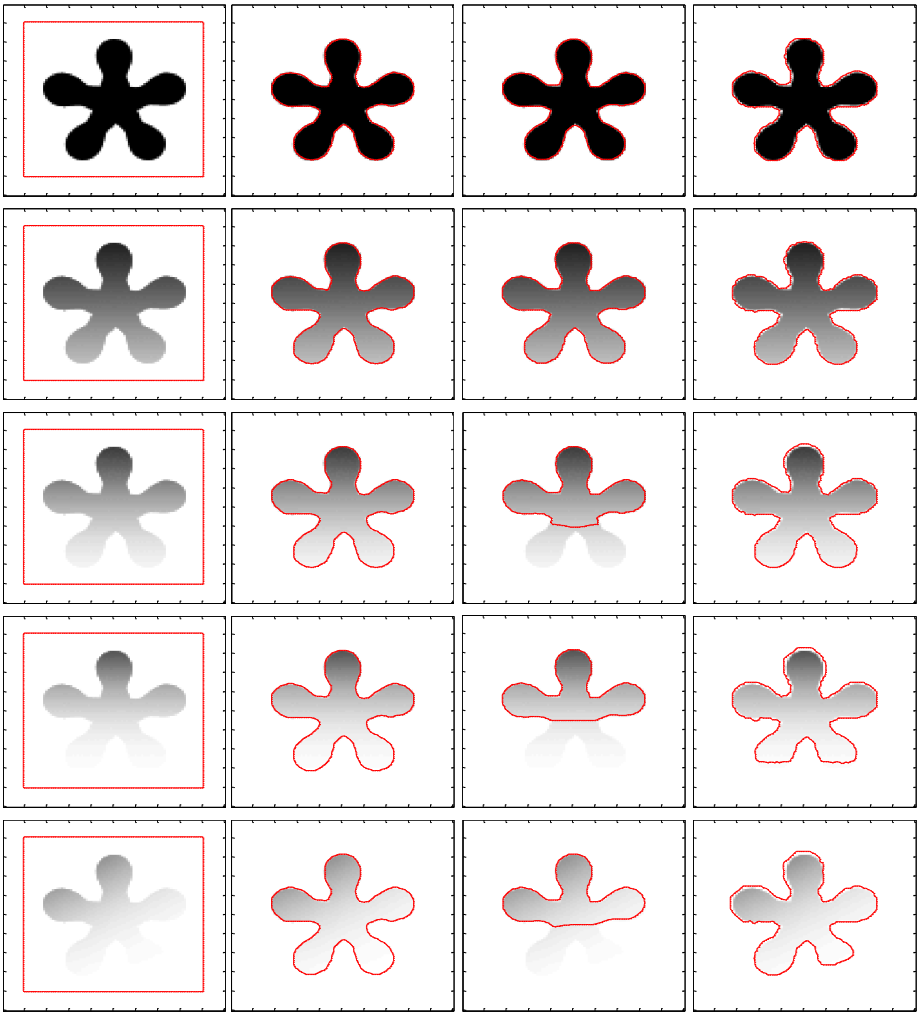

(a) (b) (c) (d)

Figure 4.3: Segmentation flower object using different contrast variations (from homogeneous to inhomogeneous). (a) Initial contour, (b) Proposed method, (c) VLSBCS, and (d) LSACM.

method (third row) are compared with the ones computed with VLSBCS by Li et al. (2008a, 2011) (first row) and LSACM by Zhang et al. (2015, 2016) (second row) using real brain MR images. The results show that the proposed method can segment more detailed regions than the other methods. In turn, the bias-corrected image using the proposed method has similar details compared to the state-of-the-art methods.

Table 4.1 shows a CPU time comparison between the evaluated retrospective active contour methods shown in figure 4.3. For all images, the proposed method yields the lowest CPU time.

In this chapter, the proposed method is also quantitatively compared with the

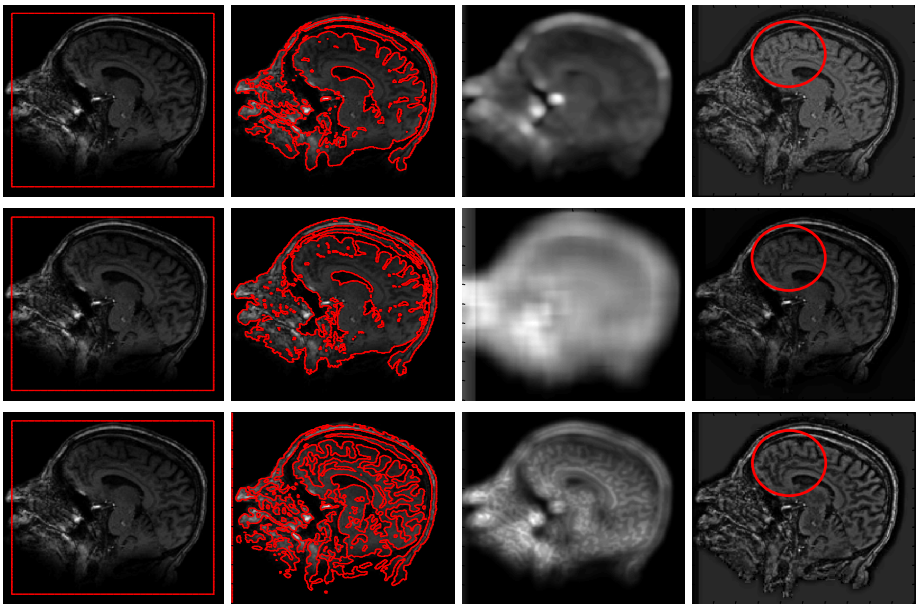

(a) (b) (c) (d)

Figure 4.4: Segmentation flower object using different contrast variations (from homogeneous to inhomogeneous). (a) Initial contour, (b) Final contour, (c) Bias field, and (d) Corrected image.

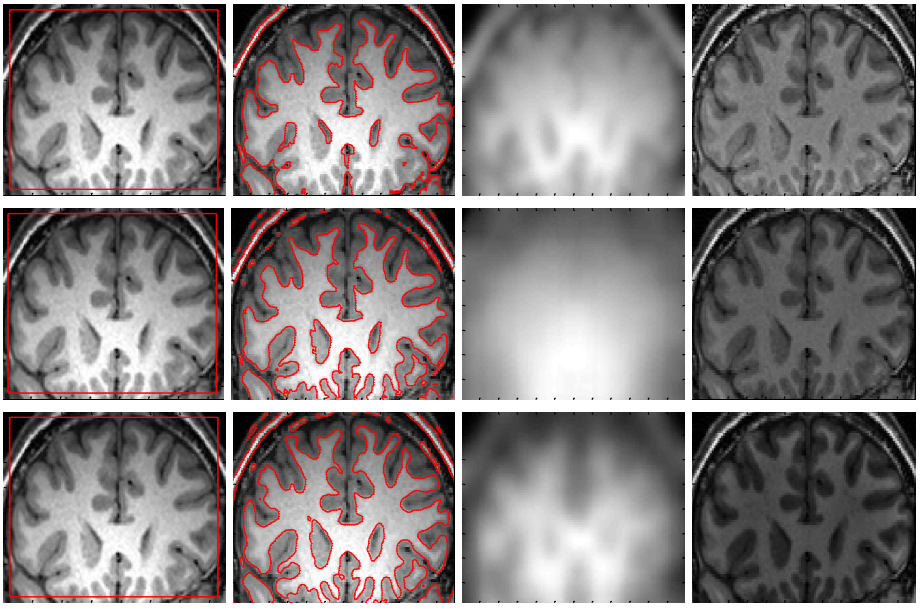

(a) (b) (c) (d)

Figure 4.5: Segmentation flower object using different contrast variations (from homogeneous to inhomogeneous). (a) Initial contour, (b) Final contour, (c) Bias field, and (d) Corrected image.

discussed state-of-the-art methods. Several similarity metrics are used to evaluate the binary segmentation of a structure in an image. Let G be the ground truth of the region of interest and S the segmented region in the given image $I : \Omega \rightarrow \mathbf{R}^2$. The

Table 4.1: CPU time comparison with the state-of-the-art.

Row	VLSBCS		LSACM		Proposed	
	Iterations	CPU time (s)	Iterations	CPU time(s)	Iterations	CPU time (s)
1	20	2	50	17.703	10	**1.875**
2	20	2.016	60	20.672	10	**1.859**
3	100	6.172	60	20.922	10	**2.172**
4	100	6.234	150	91.703	15	**1.984**
5	140	8.141	150	91.797	20	**2.359**

true positive (TP) set is defined as $TP = G \cap S$, which is the set of segmented region common in both G and S. The true negative (TN) set is defined as $TN = \overline{G} \cap \overline{S}$, which is the set of image background common in both G and S. Similarly, the false positive (FP) set is defined as $FP = \overline{G} \cap S$, which is the false object segmented as region of interest not belonging to set G. In turn, the false negative (FN) is defined as $FN = G \cap \overline{S}$, which is the region of interest missed by the proposed method during the segmentation process.

From the above subsets, two similarity metrics are computed: the Jaccard index (JI) (Jaccard, 1912) and the Dice similarity coefficient (DSC) (Dice, 1945). They are frequently used in set comparison, that is, to compute the segmentation accuracy when the ground truth of the region of interest is available. They are defined as:

$$JI = \frac{TP}{TP + FP + FN}, \quad DSC = \frac{TP}{\frac{1}{2}(TP + FN + TP + FP)}, \tag{4.13}$$

For the maximum segmentation accuracy, the values of JI and DSC should be close to 1 (ideally 1). The Hausdorff distance (HD) Huttenlocher et al. (1993) is another similarity metric used to compute the accuracy between two sets. It provides a symmetric distance measure of the maximal discrepancy between two labelled contours and is defined as:

$$HD(G, S) = \max\Big(\max_{g \in G}\big(\min_{s \in S} d(g, s)\big), \max_{s \in S}\big(\min_{g \in G} d(g, s)\big)\Big) \tag{4.14}$$

where G and S are the ground truth and computed contours, and $d(g, s)$ denotes the Euclidean distance. For the maximum segmentation accuracy, the HD value should be close to 0 (ideally 0).

Table 4.2: Segmentation accuracy comparison using different similarity metrics.

Jaccard index (JI)			Dice similarity coefficient (DSC)			Haursdorff distance (HD)		
VLSBCS	**LSACM**	**Proposed**	**VLSBCS**	**LSACM**	**Proposed**	**VLSBCS**	**LSACM**	**Proposed**
0.758 ±0.90	0.944 ±0.008	**0.968 ±0.004**	0.851 ±0.057	0.971 ±0.004	**0.984 ±0.002**	3.935 ±0.728	2.917 ±0.151	**2.416 ±0.202**

Table 4.2 shows the segmentation accuracy comparison of the proposed method with the state-of-the-art using the JI, DSC and HD metrics. For the example shown in figure 4.3, the proposed method yields the best segmentation results.

4.4 Summary

In this chapter, a retrospective active contour method is proposed to both segment and correct intensity inhomogeneity. A phase stretch transform (PST) kernel is used to redefine the image intensity means and bias field. A bias fitted image is defined and used to formulate an energy functional. Moreover, the final gradient descent solution is stabilized using a new biased signed pressure force (bSPF) function. Finally, the level-set curve is regularized using a Gaussian kernel, which also removes the need for computationally expensive re-initialization. The proposed method is compared with state-of-the-art retrospective active contour methods both qualitatively and quantitatively, yielding the best segmentation and bias correction results.

UNIVERSITAT ROVIRA I VIRGILI
AVANCES EN SISTEMAS INTERACTIVOS PARA PERSONAS CON PARÁLISIS CEREBRAL
Farhan Akram

CHAPTER 5

Active contours driven by local and global fitted image models for image segmentation robust to intensity inhomogeneity

5.1 Introduction

Image segmentation is an important stage in image processing and computer vision (Elnakib et al., 2011). Intensity inhomogeneity is one of the well-known problems in image segmentation, which arises from the imperfections of the image acquisition process or due to external interferences. It manifests as a smooth intensity variation

across the image that complicates the segmentation of the objects contained in it. For instance, in medical image analysis, segmentation and registration stages are highly sensitive to spurious variations of image intensity. Therefore, the complexity of intensity inhomogeneity can lead to false results and assumptions that can be critical for decision making by both doctors and radiologists. This is why numerous methods for intensity inhomogeneity correction have been proposed in the past (Vovk et al., 2007).

Thus, intensity inhomogeneity correction is often a pre-processing stage necessary for achieving better image segmentation. In turn, correct segmentation makes intensity inhomogeneity correction rather trivial. Actually, both intensity inhomogeneity correction and segmentation can be viewed as two intertwined processes. In segmentation-based intensity inhomogeneity correction methods, both processes are merged such that they benefit from each other.

The techniques that aim to avoid intensity inhomogeneity in the image acquisition process are known as *prospective methods*. They are only capable of correcting intensity inhomogeneity caused by the imaging device, not being able to segment the objects affected by intensity inhomogeneity. On the other hand, techniques that can correct an image and also segment the objects affected by intensity inhomogeneity are called *retrospective methods*. Retrospective methods are further classified according to the image segmentation method they apply into: filtering methods (Lewis and Fox, 2004; Studholme et al., 2004), surface fitting methods (Meyer et al., 1995; Vokurka et al., 1999), histogram-based methods (Vovk et al., 2004, 2006), and active contours (Li et al., 2008a, 2011; Zhang et al., 2015, 2016; Li et al., 2009a,b; Huang and Zeng, 2015). Segmentation-based methods (Li et al., 2011; Zhang et al., 2015, 2016) are the most versatile, since they unify segmentation and bias correction in a single framework. In these methods, segmentation and bias correction are applied in conjunction to benefit from each other.

Active contours are retrospective methods suitable for both image segmentation and bias correction (Li et al., 2011, 2014; Ivanovska et al., 2016; Kahali et al., 2016; Zhang et al., 2015, 2016). The first active contour method was proposed in Kass et al.

(1988) in order to segment an image by evolving a curve towards the boundary of an object contained in the image. An energy functional is first defined by using image statistics, curvature and gradient information. The curve is evolved by minimizing that energy functional. Active contour methods can be categorized into edge-based (Kass et al., 1988; Caselles et al., 1997; Li et al., 2005) and region-based (Mumford and Shah, 1989; Chan and Vese, 2001; Zhang et al., 2010b; Akram et al., 2015a; Li et al., 2007, 2008b; Zhang et al., 2010a; Akram et al., 2014; Peng et al., 2014; Xie et al., 2015; Li et al., 2015) methods.

Edge-based active contour methods typically use image gradient information to define an inflating balloon force that is used in the curve evolution process (Caselles et al., 1997). However, in case of intense noise or weak edges, edge-based active contours can hardly converge to the right contours. Therefore, edge-based methods are not suitable for that kind of images.

Alternatively, region-based active contour methods use statistical and curvature information from the image in the formulation of the energy functional. They can be further characterized into global (Mumford and Shah, 1989; Chan and Vese, 2001; Zhang et al., 2010b; Akram et al., 2015a) and local Li et al. (2007, 2008b); Wang et al. (2009a); Zhang et al. (2010a); Akram et al. (2014); Peng et al. (2014); Xie et al. (2015); Wang et al. (2010) methods. Mumford and Shah (1989) devised a global region-based active contour method by assuming the input image to be homogeneous. Thus, traditional active contour methods based on Mumford and Shah (1989), such as the *active contours without edges* (ACWE) method (Chan and Vese, 2001), cannot segment images with intensity inhomogeneity. These methods usually compute intensity averages over the whole image. Therefore, they cannot deal with small changes between distinct regions nor segment objects with weak or blurred boundaries. On the other hand, local-based methods (Li et al., 2008b, 2007) are able to distinguish small changes between the background and the foreground. Therefore, they are suitable for intensity inhomogeneous images.

A region-based active contour model in the context of intensity inhomogeneous image segmentation was proposed by Li et al. (2008b, 2007). The major contribution

of that work was the introduction of a region scalable fitting (RSF) energy with a kernel function that enables the extraction of accurate local image information. This model is able to segment images with intensity inhomogeneity, which overcomes the limitation of piecewise constant models (Chan and Vese, 2001). However, it is unable to correct intensity inhomogeneous objects. Moreover, this method is sensitive to the position of the initial contour.

Figure 5.1(a) shows that a traditional region based active contour method (such as ACWE) is unable to segment an image with an intensity inhomogeneous object. However, a local active contour method (such as RSF) is able to properly segment such an object, as shown in figure 5.1(b). Taking figure 5.1 as a reference, it can be concluded that active contour methods that use local statistical information of an image are able to produce fairly acceptable segmentation results in the context of intensity inhomogeneity.

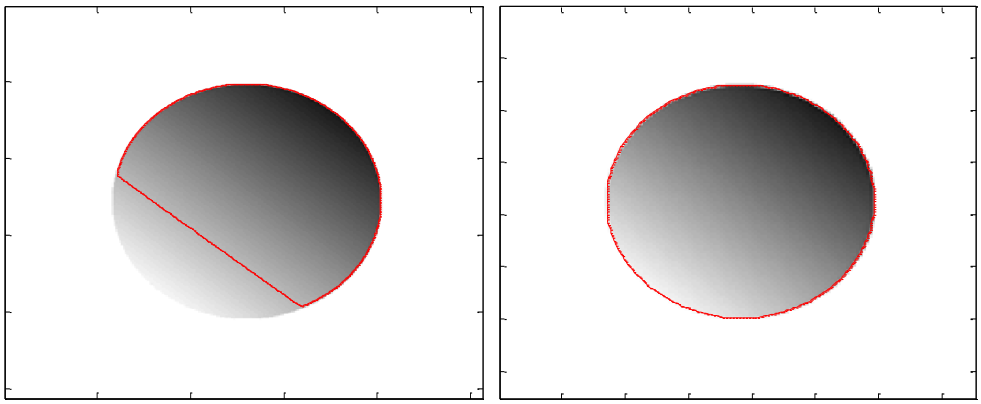

(a) (b)

Figure 5.1: Intensity inhomogeneous image segmentation using (a) ACWE and (b) RSF methods.

The present chapter proposes a new retrospective region-based active contour method that incorporates both local and global fitted images in the energy functional. The local term helps segment objects with intensity inhomogeneity, whereas the global term accelerates the evolution of the contour over smooth homogeneous regions. The new energy functional is formulated with the assumption that the local fitted image from Zhang et al. (2010a) can be divided into two different local and global components. In the gradient descent solution of the proposed energy functional, both local and global signed pressure force (SPF) functions are

introduced. The local SPF function is formulated by using local image differences and deals with inhomogeneous regions. In turn, the global SPF function is formulated by using the global image difference in order to segment homogeneous regions while reducing the convergence time of the level-set curve. The replacement of the local and global image differences by their respective SPF functions makes the gradient descent solution more stable. Finally, a Gaussian kernel is used to regularize the level-set curve, which also avoids the computationally expensive re-initialization.

In this chapter, the proposed two-phase model is also extended to a four-phase model in order to successfully segment a brain MR image into three regions: white matter (WM), grey matter (GM) and cerebrospinal fluid (CSF) regions, which is not possible with a two-phase model. Experiments with both synthetic and real images demonstrate that the proposed method yields better segmentation results and offers bias-corrected images with more detail than state-of-the-art methods.

The main contributions of this work are:

- A new region-based active contour image segmentation model is proposed to both segment and correct intensity inhomogeneous images.
- Traditional local active contour methods are able to segment intensity inhomogeneous images; however, they are sensitive to the position of the initial contour. The proposed method uses both local and global intensity means; therefore, it is not sensitive to the initial contour.
- The proposed method is robust to intensity inhomogeneous images even when they are influenced by intense noise.
- The proposed method yields a low time complexity compared to state-of-the-art local active contour methods.

The rest of the chapter is organized as follows. The proposed method is described in section 5.2. Experimental results and comparisons are shown in section 5.3 using both synthetic and real brain magnetic resonance images as a practical application scope. Quantitative analysis is presented in section 5.4 using a public database of brain anatomical models (Aubert-Broche, 2006). Finally, the chapter is summarized in section 5.5.

5.2 Proposed Method

The generally accepted assumption on intensity inhomogeneity is that it manifests itself as a smooth spatially varying function that alters image intensities that otherwise would be constant for a same object regardless its position in an image. In its simplest form, the model assumes that intensity inhomogeneity is multiplicative or additive, that is, the intensity inhomogeneity field multiplies or adds to the image intensities. Most frequently, the multiplicative model has been used as it is consistent with the inhomogeneous sensitivity of the reception coil of magnetic resonance imaging devices. Therefore, a multiplicative model has been considered for the bias field estimation. Let $I : \Omega \rightarrow \mathbf{R}^2$ be the input image with intensity inhomogeneity, $J(x)$ the restored image without intensity inhomogeneity, $b(x)$ the bias field approximated with a Gaussian distribution, and $n(x)$ additive noise in Eq. (2.24).

$J(x)$ is assumed to be constituted by k piecewise constant image components. $I(x)$ can thus be represented as:

$$I(x) = b(x)\{m_1 M_1 + m_2 M_2 + ... + m_k M_k\}, \tag{5.1}$$

where m_i are intensity means computed for the piecewise regions $\left\{\Omega_i\right\}_{i=1}^{N}$ and M_i is the characteristic function of each region.

In order to segment intensity inhomogeneous images, the following energy functional is defined:

$$E_{_{g,LGFI}} = E_{_{LGFI}}(\phi) + \mu L_g(\phi) + v A_g(\phi), \tag{5.2}$$

where $E_{_{LGFI}}(\phi)$ is a term based on a local and global fitted image, which will be explained later in this section. $\mu \geq 0$ and $v \geq 0$ are fixed parameters. $L_g(\phi)$ and $A_g(\phi)$ are length and area terms, respectively (Li et al., 2005):

$$L_g(\phi) = \int_{\Omega} g(I)\delta_\epsilon(\phi)|\nabla\phi|dx, \tag{5.3}$$

$$A_g(\phi) = \int_{\Omega} g(I)H_\epsilon(-\phi)dx, \tag{5.4}$$

The energy functional $A_g(\phi)$ is introduced to speed up the curve evolution. It is the area of the region $\Omega_\phi^- = \big\{(x,y)|\phi(x,y) < 0\big\}$ (Li et al., 2005). $A_g(\phi)$ can be viewed as the weighted area of Ω_ϕ^-. In Eq. (5.4), $g(I)$ is a positive monotonously decreasing edge indicator function ranging in [0, 1]:

$$g(I) = \frac{1}{1 + |\nabla K_\sigma * I|^2} \tag{5.5}$$

E_{LGFI} is defined according to the following reformulation of Eq. (2.21):

$$E_{LGFI} = \int_{\Omega} \big(I(x) - I_{bLFI}(x)\big)\big(I(x) - I_{GFI}(x)\big)dx, \tag{5.6}$$

5.2.1 Two-phase active contours formulation

In Eq. (5.6), let $I_{bLFI}(x)$ be a two-phase bias local fitted image and $I_{GFI}(x)$ a global fitted image, using a level-set ϕ. They are defined as:

$$I_{bLFI}(x) = b(x)(m_1M_1 + m_2M_2), \tag{5.7}$$

$$I_{GFI}(x) = c_1M_1 + c_2M_2, \tag{5.8}$$

where m_1 and m_2 are local intensity means and c_1 and c_2 are global intensity means of the given image as defined in Eqs. (2.28) and (2.13), respectively. $M_1 = H_\epsilon(\phi)$ and $M_2 = (1 - H_\epsilon(\phi))$, where $H_\epsilon(\phi)$ is the regularized Heaviside function defined in Eq. (2.10). Models based on global intensity means are not sufficient to solve intensity inhomogeneity segmentation problems. In turn, models based on local intensity means have a very high time complexity. Using both local and global fitted images, the proposed method is able to tackle the intensity inhomogeneity problem with a reduced time complexity.

As discussed earlier, an energy functional only based on a global fitted image cannot segment images with intensity inhomogeneity, since global intensity means are computed under the assumption that the input image is homogeneous. Therefore, the bias field $b(x)$ from Eq. (2.27) is only introduced in the local fitted image difference.

By using calculus of variations and steepest gradient descent (Aubert and Kornprobst, 2010), $E_{_{LGFI}}$ in Eq. (5.6) is minimized with respect to ϕ, leading to the corresponding gradient descent flow (refer to the appendix A.1 for a detailed derivation):

$$\frac{\partial \phi}{\partial t} = \Big(\big(I(x) - I_{_{bLFI}}(x)\big)(c_1 - c_2) + b(x)\big(I(x) - I_{_{GFI}}(x)\big)(m_1 - m_2) \Big) \delta_\epsilon(\phi), \quad (5.9)$$

where $b(x)$ is the bias field defined in Eq.(2.27), and $\{c_1, c_2\}$ and $\{m_1, m_2\}$ are global and local intensity means defined in Eqs. (2.13) and (2.28), respectively. The above gradient descent flow is not stable around object boundaries. Moreover, it does not yield proper segmentation when the boundaries between inhomogeneous objects and the background are indistinguishable. $(I - I_{_{bLFI}})(c_1 - c_2)$ and $(I - I_{_{GFI}})(m_1 - m_2)$ generate large values that cross a maximum threshold resulting in an unstable contour. Therefore, $(I - I_{_{bLFI}})$ and $(I - I_{_{GFI}})$ are replaced by local and global signed pressure force (SPF) functions, which normalize values to $[-1, 1]$ in order to obtain a smooth version of the gradient descent flow:

$$\frac{\partial \phi}{\partial t} = \big(\lambda_1 L_{_{SPF}}(c_1 - c_2) + \lambda_2 b G_{_{SPF}}(m_1 - m_2)\big)\delta_\epsilon(\phi), \tag{5.10}$$

where the proposed local and global SPF functions are defined as:

$$L_{_{SPF}}(I) = \begin{cases} \frac{I(x) - I_{_{bLFI}}(x)}{\max\left(\left|I(x) - I_{_{bLFI}}(x)\right|\right)}, & I(x) \neq 0 \\ 0, & I(x) = 0 \end{cases} \tag{5.11}$$

$$G_{_{SPF}}(I) = \begin{cases} \frac{I(x) - I_{_{GFI}}(x)}{\max\left(\left|I(x) - I_{_{GFI}}(x)\right|\right)}, & I(x) \neq 0 \\ 0, & I(x) = 0 \end{cases} \tag{5.12}$$

By using the calculus of variations and steepest gradient descent, the solution of $E_{_{g,LGFI}}$ from Eq. (5.2) using Eqs. (5.3) and (5.4) is:

$$\begin{aligned} \frac{\partial \phi}{\partial t} = \Bigg(&\lambda_1 L_{_{SPF}}(c_1 - c_2) + \lambda_2 b G_{_{SPF}}(m_1 - m_2) \\ &+ \mu \operatorname{div}\left(g \frac{\nabla \phi}{|\nabla \phi|}\right) + vg\Bigg)\delta_\epsilon(\phi) \end{aligned} \tag{5.13}$$

The two scaling parameters λ_1 and λ_2 in Eqs. (5.10) and (5.13) are used to tune the model to different types of images.

5.2.2 Four-phase active contours formulation

In Eq. (5.6), let $I_{_{bLFI}}(x)$ be a four-phase bias local fitted image and $I_{_{GFI}}(x)$ a global fitted image, using two level-sets $\Phi(\phi_1, \phi_2)$, which are defined as:

$$I_{_{bLFI}}(x) = b(x)(m_1 M_1 + m_2 M_2 + m_3 M_3 + m_4 M_4), \tag{5.14}$$

UNIVERSITAT ROVIRA I VIRGILI
AVANCES EN SISTEMAS INTERACTIVOS PARA PERSONAS CON PARÁLISIS CEREBRAL
Farhan Akram

$$I_{GFI}(x) = c_1 M_1 + c_2 M_2 + c_3 M_3 + c_4 M_4 \tag{5.15}$$

where $M_1(\Phi) = H_\epsilon(\phi_1)H_\epsilon(\phi_2)$, $M_2(\Phi) = H_\epsilon(\phi_1)(1 - H_\epsilon(\phi_2))$, $M_3(\Phi) = (1 - H_\epsilon(\phi_1))$ $H_\epsilon(\phi_2)$ and $M_4(\Phi) = (1 - H_\epsilon(\phi_1))(1 - H_\epsilon(\phi_2))$, which are the characteristic terms that partition a given image into four segments. $b(x)$ is the bias term defined for the four-phase energy functional. m_1, m_2, m_3 and m_4 are local intensity means from VLSBCS (Li et al., 2008a, 2011) and c_1, c_2, c_3 and c_4 are global intensity means from the multiphase level-set framework (MLSF) (Vese and Chan, 2002), which is a multiphase extension of the two-phase energy functional defined by Chan and Vese (2001).

By substituting the four-phase fitted equations in Eq. (5.6) using steepest gradient descent (Aubert and Kornprobst, 2010), the following solutions are obtained for ϕ_1 and ϕ_2 (for detailed formulation see appendix A.2):

$$\begin{aligned}\frac{\partial \phi_1}{\partial t} = \Big[& b\big(I - I_{GFI}\big)\big((m_1 - m_3)H_\epsilon(\phi_2) + (m_2 - m_4)(1 - H_\epsilon(\phi_2))\big) \\ & + \big(I - I_{bLFI}\big)\big((c_1 - c_3)H_\epsilon(\phi_2) + (c_2 - c_4)(1 - H_\epsilon(\phi_2))\big)\Big]\delta_\epsilon(\phi_1)\end{aligned} \tag{5.16}$$

$$\begin{aligned}\frac{\partial \phi_2}{\partial t} = \Big[& b\big(I - I_{GFI}\big)\big((m_1 - m_2)H_\epsilon(\phi_1) + (m_3 - m_4)(1 - H_\epsilon(\phi_1))\big) \\ & + \big(I - I_{bLFI}\big)\big((c_1 - c_2)H_\epsilon(\phi_1) + (c_3 - c_4)(1 - H_\epsilon(\phi_1))\big)\Big]\delta_\epsilon(\phi_2)\end{aligned} \tag{5.17}$$

Four-phase local and global SPF functions can be obtained by substituting I_{bLFI} and I_{GFI} from Eqs. (5.14) and (5.15) in Eqs. (5.11) and (5.12), respectively. By replacing the four-phase local and global fitted differences with their respective SPF functions, Eqs. (5.16) and (5.17) are updated as follows:

$$\begin{aligned}\frac{\partial \phi_1}{\partial t} = \Big[& \lambda_1 b G_{SPF}\big((m_1 - m_3)H_\epsilon(\phi_2) + (m_2 - m_4)(1 - H_\epsilon(\phi_2))\big) \\ & + \lambda_2 L_{SPF}\big((c_1 - c_3)H_\epsilon(\phi_2) + (c_2 - c_4)(1 - H_\epsilon(\phi_2))\big)\Big]\delta_\epsilon(\phi_1)\end{aligned} \tag{5.18}$$

$$\frac{\partial \phi_2}{\partial t} = \Big[\lambda_1 b G_{_{SPF}}\big((m_1 - m_2)H_\epsilon(\phi_1) + (m_3 - m_4)(1 - H_\epsilon(\phi_1))\big) + \lambda_2 L_{_{SPF}}\big((c_1 - c_2)H_\epsilon(\phi_1) + (c_3 - c_4)(1 - H_\epsilon(\phi_1))\Big]\delta_\epsilon(\phi_2) \tag{5.19}$$

The SPF functions defined in Eqs. (5.11) and (5.12) are used to normalize the local and global image differences in the range [-1, 1] inside and outside the region of interest. SPF functions have been formulated in numerous ways (e.g., (Zhang et al., 2010b; Akram et al., 2014, 2015a; Li et al., 2015)), some of them incorporating global intensity means and others using local intensity means. The new SPF functions proposed in this work are based on both global and local intensity-based fitted images. Figure 5.2 shows the signs of an SPF function based on a global fitted image inside and outside the region of interest. In turn, figure 5.3 shows the sign of an SPF function based on a local fitted image inside and outside the region of interest.

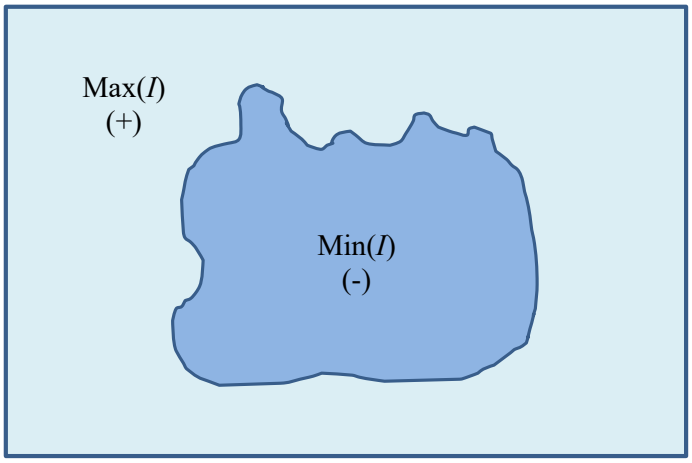

Figure 5.2: Signs of a global SPF function. It is positive outside the object and negative within it.

Since the local SPF function uses local intensity means, it is able to distinguish small changes at the boundaries of intensity inhomogeneous objects. Since the local intensity means are computed in a local neighbourhood, the positive and negative values are distributed close to the inner and outer boundaries of the image contours. In the rest of the image, the SPF function becomes zero. In figure 5.3, white shows negative values of the local SPF function, black shows positive values of the local SPF function, and blue represents the region where the local SPF function becomes

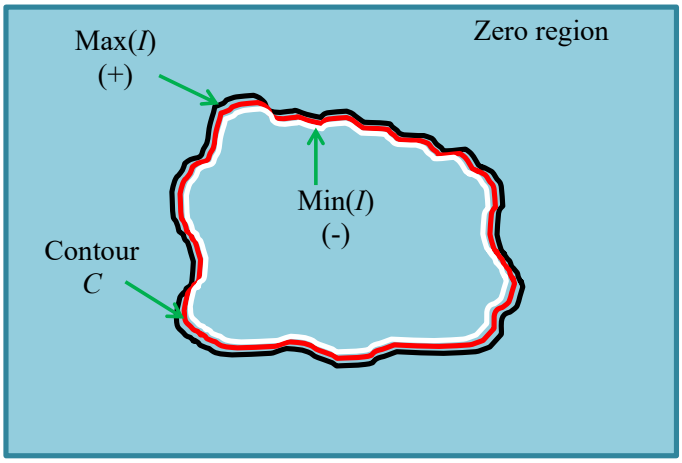

Figure 5.3: Signs of a local SPF function. It is positive along the outer boundary, negative along the inner boundary and zero elsewhere.

zero.

In contrast, the global SPF function is unable to segment intensity inhomogeneous regions, since global intensity means are computed all over the image. It has positive and negative values inside and outside the region of interest, and is zero at its boundary, as shown in figure 5.2.

In level-set methods, it is essential to initialize the level-set function ϕ as a signed distance function (SDF) ϕ_0. If the initial level-set function is significantly different from the SDF, re-initialization schemes are unable to re-initialize the function to the SDF. In the proposed formulation, not only is the re-initialization procedure completely eliminated, but the level-set function ϕ no longer needs to be initialized as an SDF. The initial level-set function ϕ_0 is defined as:

$$\phi(x, t=0) = \begin{cases} -\rho, & x \in \Omega_0 - \partial\Omega_0 \\ 0, & x \in \partial\Omega_0 \\ \rho, & x \in \Omega - \Omega_0 \end{cases} \tag{5.20}$$

where ρ is a positive constant, Ω_0 is the inner region of the initial contour, Ω is the image domain and $\partial\Omega_0$ refers to the initial contour. The stages of the proposed method can be summarized as:

(a) Initialize the level-set function ϕ to ϕ_0 using Eq. (5.20) and the bias field to

UNIVERSITAT ROVIRA I VIRGILI
AVANCES EN SISTEMAS INTERACTIVOS PARA PERSONAS CON PARÁLISIS CEREBRAL
Farhan Akram

$b(x) = 0$.

(b) Compute the edge indicator function $g(I)$ using Eq. (5.5).

(c) Compute the local intensity means, m_1, m_2, and the global means, c_1, c_2, using Eqs. (2.28) and (2.13), respectively. Compute the bias field $b(x)$ from Eq. (2.27).

(d) Calculate $L_{SPF}(I)$ and $G_{SPF}(I)$ using Eqs. (5.11) and (5.12), respectively.

(e) Solve the partial differential equation (PDE) of ϕ using Eq. (5.13).

(f) Regularize the level-set function ϕ at time t by applying a Gaussian kernel G_χ, i.e. $\phi = G_\chi * \phi$, where χ is the standard deviation of the regularizing Gaussian kernel.

(g) Check whether the regularized level-set function is stationary. If not, iterate from step (c).

The steps described above correspond to the two-phase segmentation algorithm. However, for the four-phase algorithm, these steps are replaced with the variables corresponding to two level-sets using their respective definitions and solutions.

Table 5.1: Parameters for the experiments in section 5.3.

	Force term scaling constants		**Length term scaling constant**	**Area term scaling constant**	**Gaussian kernel tuning constant**		**Penalizing term scaling constant**	**Constant for initial level-set**	**Constant for Heaviside and Dirac Functions**	**Time step**
	λ_1	λ_2	μ	v	σ or σ_1	χ or σ_2	γ	ρ	ϵ	Δt
RSF	1	1	0.001×255^2	-	4	-	1	1	1.5	0.1
LIF	-	-	-	-	3	1	-	2	1.5	1
LGD	1	1	0.001×255^2	30	5	-	$1/\mu$	2	1.5	0.1
VLSBCS	1	1	0.001×255^2	-	3	-	1	1	1	0.1
LSACM	1	1	-	20	3	-	0.1	1	1.5	1
Proposed	1	5	1	0.25	3	0.5	-	1	1.5	0.1

5.3 Results and Comparisons

The proposed method was implemented using MATLAB and run on a 3.4 GHz Intel Core-i7 with 16 GB of RAM, testing it on both synthetic images and real brain magnetic resonance (MR) images of 250×250 pixels with 256 grey levels (8bpp). The parameters used for all experiments in this section are shown in Table 5.1.

Figure 5.4 shows the result of the proposed segmentation method and the comparison with the different state-of-the-art methods that have been tested. In this experiment, we used an image with a single homogeneous object and then progressively changed its intensity distribution to a point at which it is even difficult to manually segment it, thus making the object inhomogeneous.

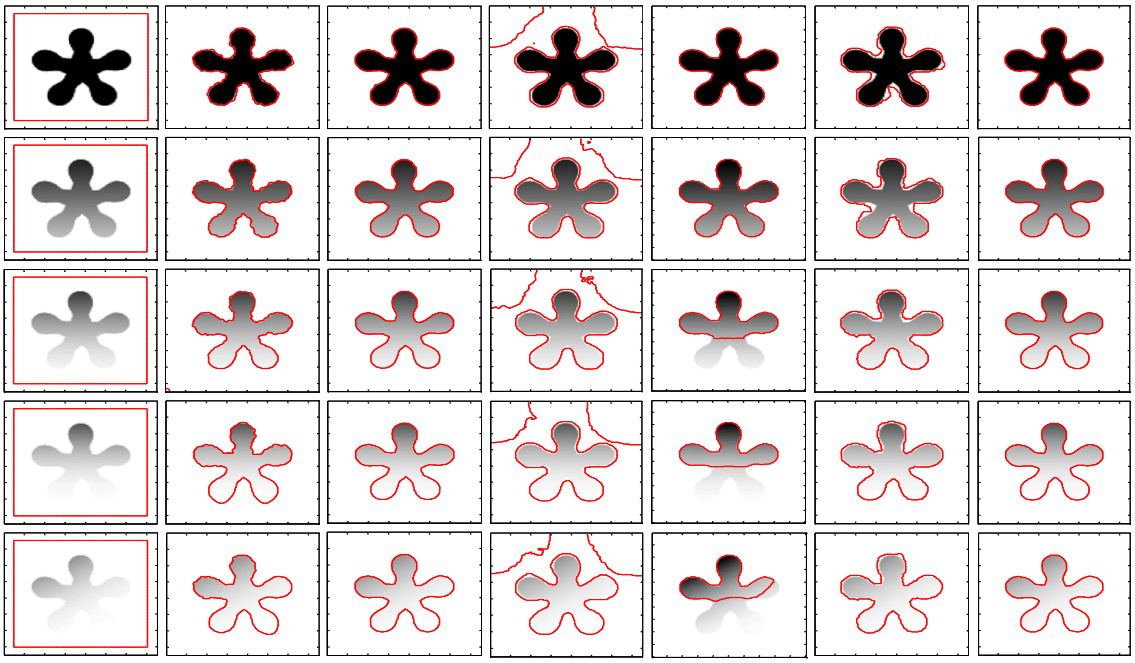

(a) (b) (c) (d) (e) (f) (g)

Figure 5.4: Intensity inhomogeneous image segmentation and comparison with state-of-the-art methods by using images with intensity varying objects. (a) Initial contour, (b) LIF, (c) RSF, (d) LGD, (e) VLSBCS, (f) LSACM, and (g) Proposed method.

The first column shows the five input images with the initial contour, whereas the segmentation results are shown using LIF (Zhang et al., 2010a) in the second column, RSF (Li et al., 2008b, 2007) in the third column, LGD (Wang et al., 2009a) in the fourth column, VLSBCS (Li et al., 2008a, 2011) in the fifth column, LSACM (Zhang et al., 2015, 2016) in the sixth column and the proposed method in the last column, respectively. Visual inspection clearly shows that both the proposed method and RSF provide the best segmentation results. LIF also yields acceptable segmentation results, although the final contour in this method is not quite smooth along the object boundaries. Segmentation results of both LSACM and LGD show that they are not able to strictly find the object boundary. Moreover, the contour

in LGD is also stuck in the background, which is undesirable. VLSBCS properly segmented the first two images, but its segmentation results are not acceptable for the last three images. In LGD, σ was set to 10 for all experiments in figure 5.4, since with a small value of σ, this method is unable to segment the objects in all images. For all the examples in figure 5.4, the parameters of all methods were kept constant. The only change is the initial position of the level-set.

Figure 5.5 shows the experiments conducted with synthetic images with different types of region properties. The first column shows the input images with their respective initial contours. In the first row, both the object and the background are homogeneous. In the second row, the background is homogeneous while the object is inhomogeneous. In the third row, the background is inhomogeneous while the object is homogeneous. In the fourth row, both the background and the object are inhomogeneous. In the last row, the background is homogeneous and there are different inhomogeneous regions, with one of the regions having an extra inhomogeneous region within it.

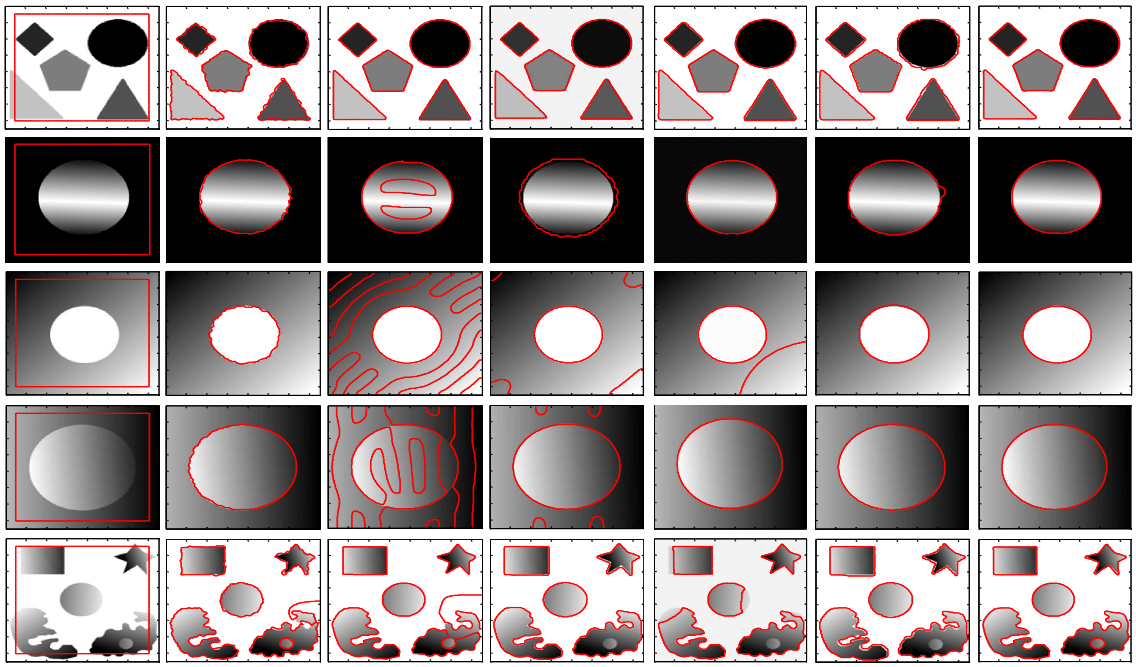

(a) (b) (c) (d) (e) (f) (g)

Figure 5.5: Segmentation results using images with different homogeneity and inhomogeneity possibilities. (a) Initial contour, (b) LIF, (c) RSF, (d) LGD, (e) VLSBCS, (f) LSACM, and (g) Proposed method.

UNIVERSITAT ROVIRA I VIRGILI
AVANCES EN SISTEMAS INTERACTIVOS PARA PERSONAS CON PARÁLISIS CEREBRAL
Farhan Akram

The second column shows the segmentation results with LIF (Zhang et al., 2010a). Notice that it is not able to accurately segment the last image. Although this method is able the segment the objects in the first four images, the results are not acceptable because the contour is not quite smooth along the boundaries of the objects. The segmentation results with RSF (Li et al., 2008b, 2007) are shown in the third column. This method is only able to properly segment the first image, while the segmentation results are not acceptable for the other images. The fourth column shows the segmentation results using LGD (Wang et al., 2009a). This method is able to properly segment the first image. As for the second image, the contour is not quite smooth along the boundary of the object. Although it is able to segment the objects in the third and fourth images, some undesirable contour is stuck in the background. Furthermore, this method is not able to segment the nested inhomogeneous object in the fifth image.

The fifth column shows the segmentation results using VLSBCS by Li et al. (2008a, 2011). This method is able to properly segment the first, second and fourth images. It can segment the object in third image. However, some undesirable contour is stuck in the background. Moreover, this method is not able to properly segment the fifth image. The sixth column shows the results with LSACM by Zhang et al. (2015, 2016). This method is able to properly segment the third and fourth images. Although it is able to segment the objects in the first and second images, the final contour is not smooth and does not properly follow the object boundaries. Moreover, this method is unable to segment the nested inhomogeneous object in the fifth image. The last column shows the segmentation results using the proposed method, which is able to properly segment all images.

Table 5.2 shows a time complexity analysis in terms of CPU time and iterations. The proposed method yields the lowest time complexity for the examples shown in rows 1, 2 and 4, 5. It took 1.58 and 2.19 seconds for the examples shown in the first two rows, respectively. In turn, it took 5.09 and 5.78 seconds for the examples shown in rows 4 and 5, respectively. On the other hand, VLSBCS yields the lowest time complexity for the example shown in row 3. It took 2.27 seconds while the proposed

UNIVERSITAT ROVIRA I VIRGILI
AVANCES EN SISTEMAS INTERACTIVOS PARA PERSONAS CON PARÁLISIS CEREBRAL
Farhan Akram

Table 5.2: Iterations and CPU time for the examples shown in figure 5.4.

Methods		Figure 4				
		Row 1	**Row 2**	**Row 3**	**Row 4**	**Row 5**
LIF	Iterations	400	450	600	2000	2000
	CPU time (s)	5.45	5.97	7.56	57.38	55.91
RSF	Iterations	500	1000	1500	2000	2000
	CPU time (s)	7.72	14.38	26.36	32.63	32.44
LGD	Iterations	500	500	500	500	500
	CPU time (s)	34.03	32.77	33.69	32.06	34.12
VLSBCS	Iterations	20	30	30	100	100
	CPU time (s)	1.71	2.21	**2.27**	5.87	6.31
LSACM	Iterations	40	40	50	60	80
	CPU time (s)	24.69	25.55	32.05	38.69	50.72
Proposed	Iterations	20	30	70	90	100
	CPU time (s)	**1.58**	**2.19**	4.12	**5.09**	**5.78**

method took 4.17 seconds to obtain the final contour. Although VLSBCS yields the lowest time complexity for this example, it is unable to properly segment the object, as shown in figure 5.4.

In figure 5.6, the segmentation and bias correction results using the proposed method (third row) are compared with the ones computed with VLSBCS by Li et al. (2008a, 2011) (first row) and LSACM by Zhang et al. (2015, 2016) (second row) using real brain MR images as a practical application. The first column shows the input image with the initial contour. The second column shows the final contours for each method. The third column shows the estimated bias field. Finally, the last column shows the bias-corrected image. The proposed method can segment more detailed regions than the other methods, as highlighted by the green arrows in the second column. Moreover, the bias-corrected image using the proposed method has more details than the ones computed with the other methods, as highlighted by the red circles in the fourth column. The corrected image obtained using the proposed method also has more details in the nose area.

In figure 5.7, the segmentation results and bias correction using the proposed method (third row) are compared with the ones computed with VLSBCS by Li et al. (2008a, 2011) (first row) and LSACM by Zhang et al. (2015, 2016) (second row) using real brain MR images. The first column shows the input image with the initial contour. The second column shows the final contours. The third column shows the

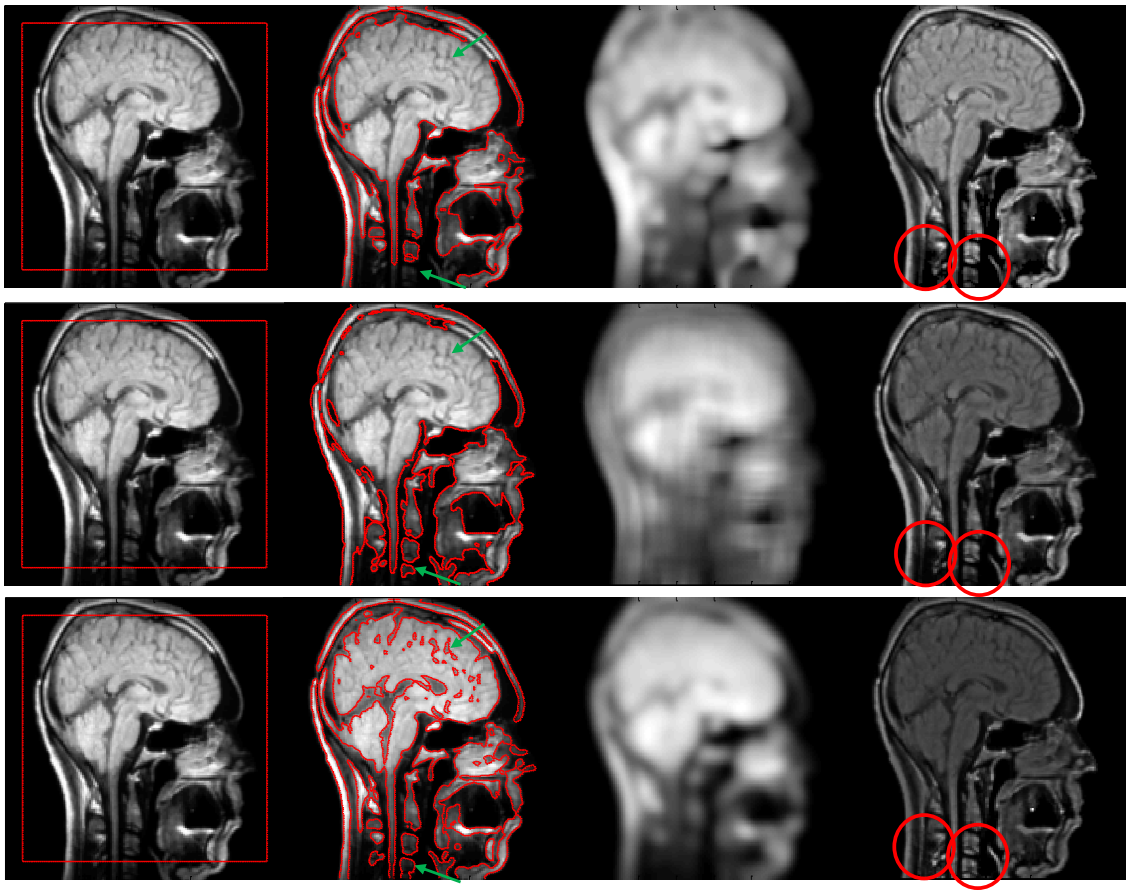

(a) (b) (c) (d)

Figure 5.6: Segmentation and bias correction using Li et al. Li et al. (2008a, 2011) (first row), Zhang et al. Zhang et al. (2015, 2016) (second row) and the proposed method (third row). (a) Initial contour, (b) Final contour, (c) Bias field, and (d) Corrected image.

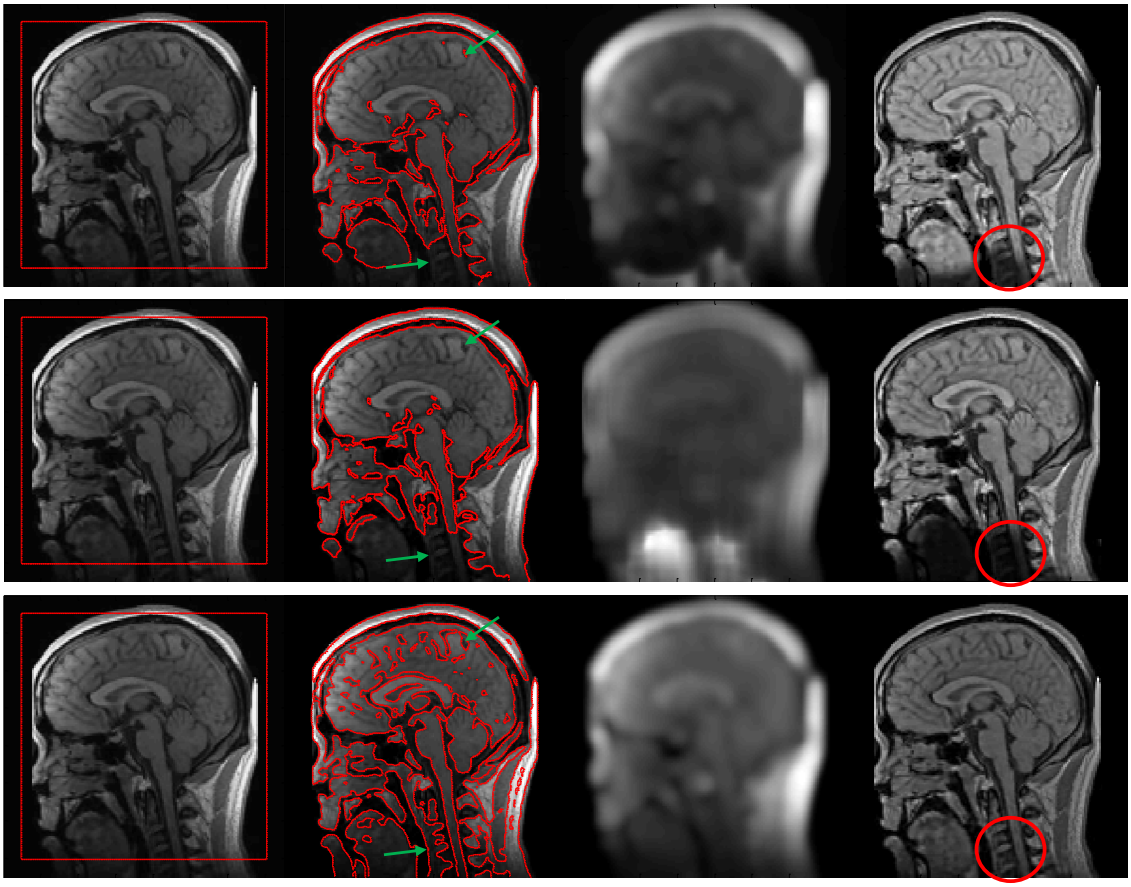

(a) (b) (c) (d)

Figure 5.7: Segmentation and bias correction using Li et al. Li et al. (2008a, 2011) (first row), Zhang et al. Zhang et al. (2015, 2016) (second row) and the proposed method (third row). (a) Initial contour, (b) Final contour, (c) Bias field, and (d) Corrected image.

computed bias field. Finally, the last column shows the bias-corrected image. The results show that the proposed method can segment more detailed regions than the other methods, as highlighted by the green arrows in the second column. Moreover, the bias-corrected image using the proposed method has more details than the ones computed with the other methods, as highlighted by the red circles in the fourth column.

Figure 5.8 shows the effect of the position of the initial level-set on the segmentation for all the tested methods. The first column shows the input image with different initial level-sets, whereas the segmentation results with LIF by Zhang et al. (2010a) are shown in the second column, with RSF by Li et al. (2008b, 2007) in the third column, with LGD by Wang et al. (2009a) in the fourth column, with VLSBCS by Li et al. (2008a, 2011) in the fifth column, with LSACM by Zhang et al. (2015, 2016) in the sixth column and with the proposed method in the last column. These results show that the proposed method is not affected by the position of the initial level-set and yields the segmentation with the best accuracy. In contrast, the segmentation results of all the tested state-of-the-art methods are affected by the position of the initial level-set.

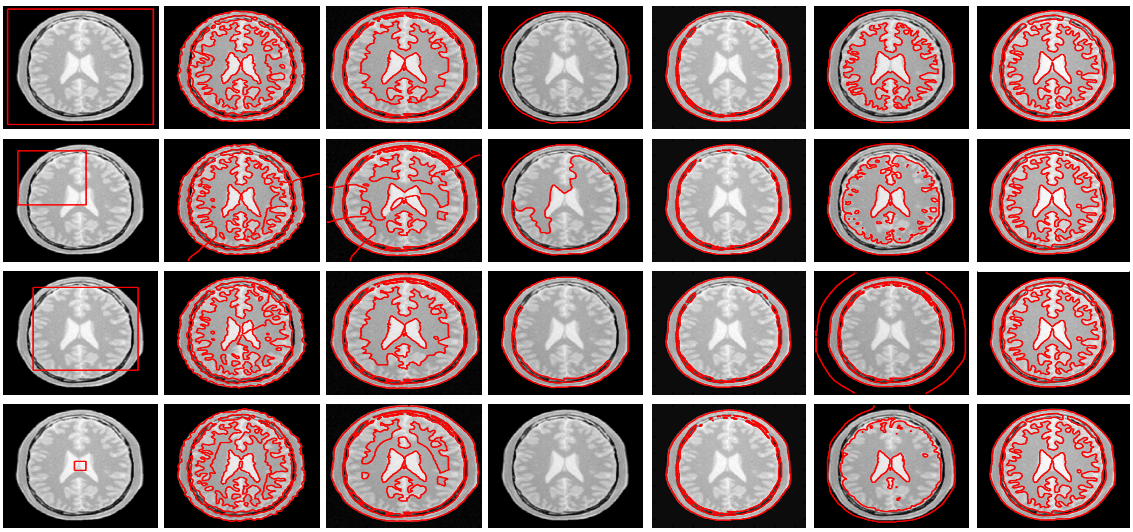

(a) (b) (c) (d) (e) (f) (g)

Figure 5.8: Effect of position of initial contour on the final segmentation results. (a) Initial contour, (b) LIF, (c) RSF, (d) LGD, (e) VLSBCS, (f) LSACM, and (g) Proposed method.

Table 5.3 shows the number of iterations and CPU time for all the tested methods

when applied to the example in figure 5.8. The proposed method yields the best performance in the examples shown in rows 2 and 4. It took 2.48 and 1.42 seconds to obtain the final contours for rows 2 and 4, which is significantly lower than the time required by the other methods. In turn, LGD has the best performance for the example in row 1. Thus, LGD took 3.3 seconds, while the proposed method took 5.15 seconds to obtain the final contour. In turn, LIF yields the best performance for the example shown in row 3. LIF took 3.86 seconds while the proposed method took 16.06 seconds to obtain the final contour.

Table 5.3: Iterations and CPU time for the examples shown in figure 5.8.

Methods		**Figure 8**			
		Row1	**Row2**	**Row3**	**Row4**
LIF	Iterations	250	250	250	200
	CPU time (s)	4.16	4.18	**3.86**	3.29
RSF	Iterations	400	400	400	250
	CPU time (s)	8.69	8.18	8.09	5.56
LGD	Iterations	200	1500	1000	100
	CPU time (s)	**3.3**	22.91	15.65	2.14
VLSBCS	Iterations	100	100	100	100
	CPU time (s)	5.64	7.27	6.47	6.72
LSACM	Iterations	250	250	250	600
	CPU time (s)	14.31	14.53	13.98	33.47
Proposed	Iterations	80	30	300	10
	CPU time (s)	5.15	**2.48**	16.06	**1.42**

Figure 5.9 shows the segmentation result for a synthetic image, which contains three different regions with intensity inhomogeneity, both without noise and after applying additive Gaussian noise. Figure 5.9(b) and (d) show that proposed method is able to properly segment intensity inhomogeneous objects with and without noise, respectively. Figure 5.9(e) shows the central row intensity profile of the input synthetic image with both clean and noisy data along with the final contour. The resultant contour followed the object boundaries perfectly.

Figure 5.10 shows some segmentation results by applying the proposed method to different intensity inhomogeneous noisy images. Although noise affected the crispness of edges in the input data, the proposed method is able to yield acceptable segmentation results.

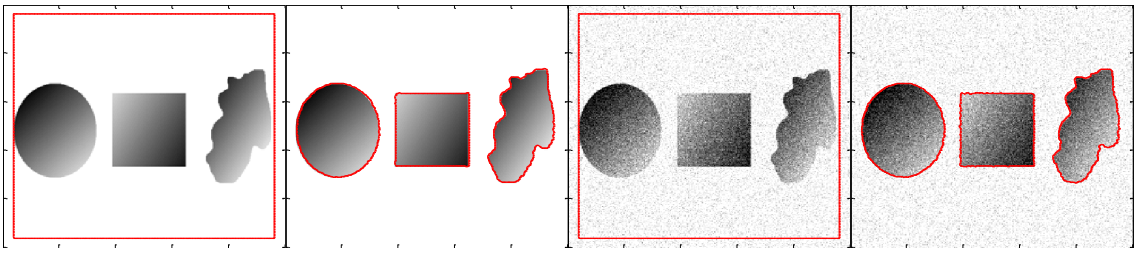

(a) (b) (c) (d)

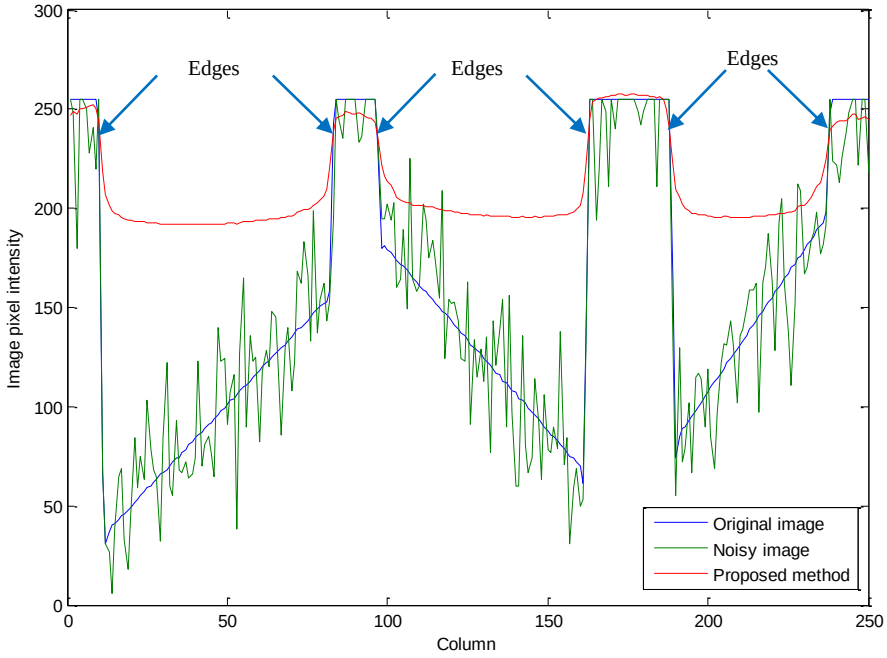

(e)

Figure 5.9: Segmentation results on synthetic images with intensity inhomogeneity with and without noise. (a) Original image with initial contour, (b) Segmentation result using original image without noise, (c) Noisy image with initial contour, (d) Segmentation result using noisy image, (e) Profile selection of the middle rows of the original image (blue line), noisy image (green line) and level-set of proposed method (red line).

5.4 Quantitative analysis

The segmentation of brain MR images into disjoint regions based on white matter (WM), grey matter (GM) and cerebrospinal fluid (CSF) is a well-known problem in brain image analysis. Due to the geometric complexity of the human brain cortex, manual slice-by-slice segmentation is cumbersome and time consuming (Elnakib et al., 2011). Thus, numerous methods have been devised to solve such problems. Active contours are quite popular in this context. Because of the complex intensity

UNIVERSITAT ROVIRA I VIRGILI
AVANCES EN SISTEMAS INTERACTIVOS PARA PERSONAS CON PARÁLISIS CEREBRAL
Farhan Akram

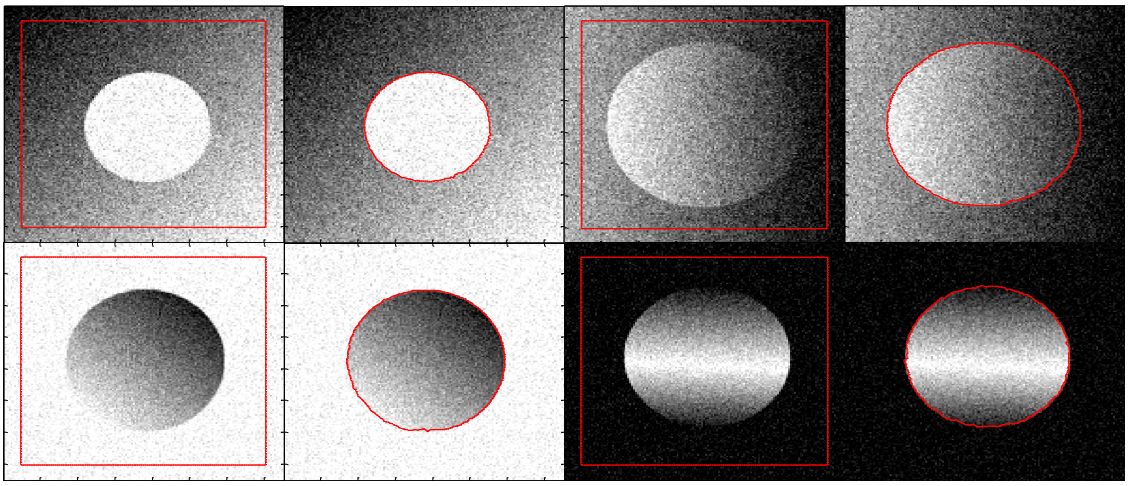

(a) (b) (c) (d)

Figure 5.10: Segmentation results on different intensity inhomogeneous noisy images. (a) and (c) Initial contour, (b) and (d) Final contour.

inhomogeneous regions, brain MR images are hard to be successfully segmented with high accuracy (Balafar et al., 2010). Therefore, this is a good test bench to test the proposed method in a practical application and compare it with other state-of-the-art methods.

5.4.1 Two-phase active contours

This section shows segmentation results for all tested two-phase active contour methods using 2D brain MR images from a public database of 20 brain anatomical models (Cocosco et al., 1997; Aubert-Broche et al., 2006). All images have 250×250 pixels and 8 bits per pixel.

Active contour methods behave differently for different types of images. Because the images used in this section have different characteristics compared to the ones used in section 5.3, the parameters had to be tuned in order to obtain the best possible segmentation results. The parameters used for all experiments in this section are shown in Table 5.4.

In order to partition a brain MR image into WM and GM regions, the segmentation result is split into two regions based on two phases: $\phi > 0$ and $\phi < 0$. The WM and GM regions represent the brain region, which is the region of interest,

Table 5.4: Parameters for the experiments in quantitative analysis section.

	Force term scaling constants		Length term scaling constant	Area term scaling constant	Gaussian kernel tuning constant		Penalizing term scaling constant	Constant for initial level-set	Constant for Heaviside and Dirac Functions	Time step
	λ_1	λ_2	μ	v	σ or σ_1	χ or σ_2	γ	ρ	ϵ	Δt
RSF	1	1	0.001×255^2	-	3	-	1	1	1.5	0.1
LIF	-	-	-	-	2	0.5	-	2	1.5	1
LGD	1	1	0.001×255^2	30	3	-	$1/\mu$	2	1.5	0.1
VLSBCS	1	1	0.001×255^2	-	3	-	1	1	1	0.1
LSACM	1	1	-	20	3	-	0.1	1	1.5	1
Proposed	5	1	1	0.25	3	0.5	-	1	1.5	1

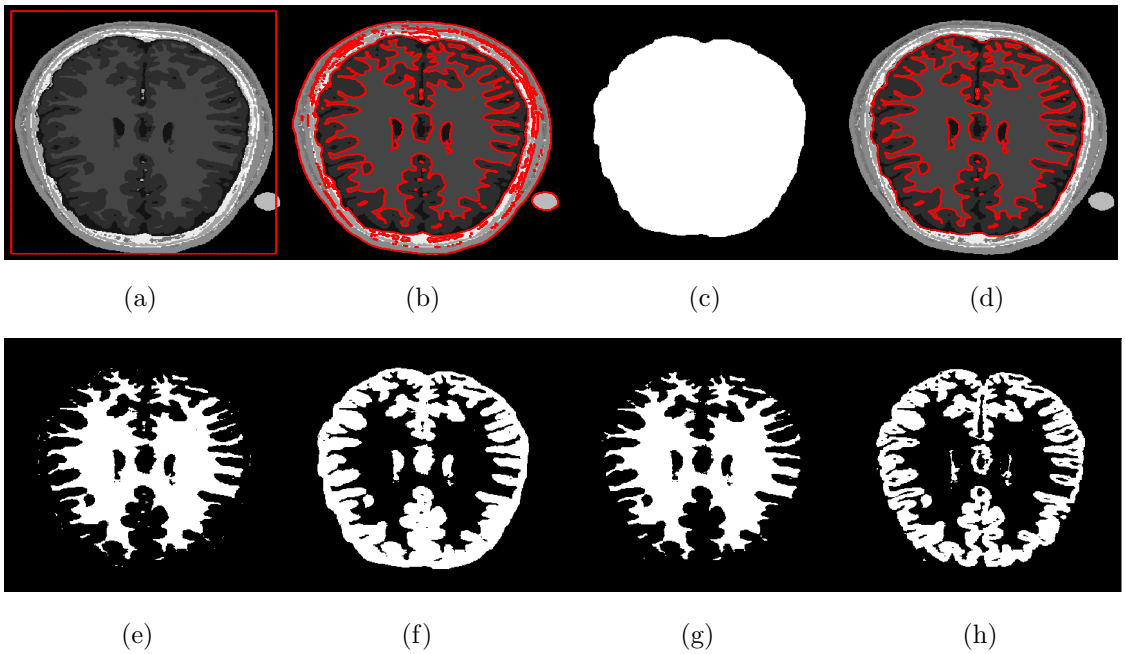

Figure 5.11: WM and GM regions computed with the proposed method and their respective ground truths. (a) Initial contour, (b) Final contour, (c) Brain mask, (d) Masked contour, (e) Computed WM, (f) Computed GM, (g) WM ground truth, and (h) GM ground truth.

while the regions outside the brain (e.g., skull, fat and vacuum) can be taken as irrelevant regions. Therefore, we manually extracted the brain area to segment the WM and GM regions, removing the other irrelevant regions out of the brain. Figure 5.11 shows the WM and GM regions computed from the two phases of the proposed method and the comparison with the ground truth (GT). In the first row of figure 5.11, the first image shows the input image with the initial contour. The second image shows the final contour using the proposed method. The third image shows a manually defined brain mask. The main purpose of the brain mask is to

extract the brain region in order to carefully analyse and compare the segmented WM and GM regions with their respective ground truths. The last image in the first row shows the final contour after scaling with the brain mask. Let $\phi(x, y)$ be the final computed contour shown in the second column of the first row, and $m(x, y)$ the manually defined brain mask shown in the third column of the first row. The scaled final contour $\xi(x, y)$, which is shown in the last column of the first row, is computed as $\xi(x, y) = \phi(x, y)m(x, y)$. In the second row of figure 5.11, the first image shows the WM region computed from the positive phase ($\xi > 0$) of the final contour scaled with the brain mask. The second image shows the GM region computed using the negative phase ($\xi < 0$) of the scaled final contour. In the second row, the third and fourth images show the ground truths of the WM and GM regions, respectively.

Figure 5.12 shows the accuracy analysis of the region of interest in the brain MR images. A total of 100 2D slices from 20 brain anatomical models (Aubert-Broche, 2006) were used. Five 2D slices from every patient were considered. The WM and GM regions for all methods were computed as depicted in figure 5.11. The segmentation accuracy corresponding to the WM and GM regions presented in figure 5.12 was obtained as:

$$\text{Accuracy} = \frac{|A \cap B|}{|A \cup B|} \times 100, \tag{5.21}$$

where A is the computed WM or GM region after brain scaling and B is the ground truth for that region. Different methods can behave differently based on the type of images. Therefore, five slices from each patient were used and average accuracies for those slices were computed to obtain a representative value for each case. Figure 5.12 and Table 5.5 show that the proposed method yields the best segmentation accuracy in most cases for both the WM and GM regions. Both the mean and standard deviation (mean error) are considered for two brain regions, i.e., WM, GM.

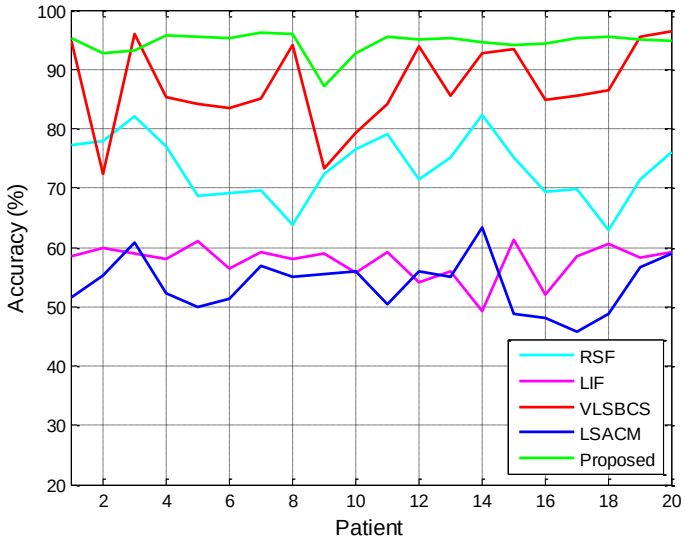

(a)

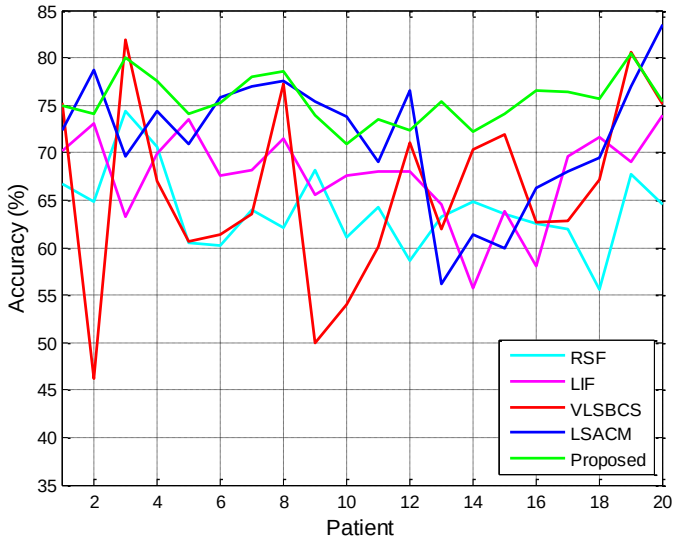

(b)

Figure 5.12: Segmentation accuracy analysis of (a) WM, and (b) GM regions using two-phase active contours.

Table 5.5: Segmentation accuracy of WM and GM regions using the two-phase active contour methods.

Region	RSF	LIF	VLSBCS	LSACM	Proposed
WM	73.34 ± 1.20	57.65 ± 0.68	87.32 ± 1.60	53.82 ± 1.01	**95.69 ± 0.48**
GM	63.97 ± 0.95	67.64 ± 1.07	66.04 ± 2.16	71.63 ± 1.53	**75.78 ± 0.62**

5.4.2 Four-phase active contours

A two-phase method is limited to segmenting images into two regions, which is its big weakness in its application to brain MR image segmentation. In the last subsection, all of the two-phase tested methods are evaluated for WM and GM region segmentation. However, the segmented GM region was a combination of GM and CSF regions, resulting into a high amount of false positives. In this subsection, the four-phase model of the proposed active contour method is evaluated along with the state-of-the-art four-phase active contour methods with respect to the segmentation accuracy of WM, GM and CSF regions. All methods are tested using the same brain MR image database mentioned in the previous subsection with the same image size and intensity. The parameters used for the proposed method are: $\lambda_1 = 2$, $\lambda_2 = 2$, $\mu = 5$, $\sigma = 3$, $\chi = 0.45$, $\rho = 1$, $\epsilon = 1.5$ and $\Delta t = 1$.

In brain MR images, WM, GM and CSF regions represent the brain, which is the region of interest. The regions outside the brain (e.g., skull, fat and vacuum) can be assumed to be irrelevant regions. In order to remove those unwanted regions, it is necessary to strip the skull from the brain MR image using a manually drawn brain mask. A brain mask is used as shown in figure 5.11, although it is used for the four-phase method. Let $\phi_1(x, y)$ and $\phi_2(x, y)$ be the final computed contours for two level-sets, $m(x, y)$ be the manually defined brain mask and $\xi_1(x, y)$ and $\xi_2(x, y)$ scaled final contours with the brain mask, which are computed as: $\xi_1(x, y) = \phi_1(x, y)m(x, y)$ and $\xi_2(x, y) = \phi_2(x, y)m(x, y)$. By using the proposed method, the four regions are computed as follows: $R_1 = (\xi_1 > 0) \cap (\xi_2 > 0)$, $R_2 = (\xi_1 > 0) \cap (\xi_2 < 0)$, $R_3 = (\xi_1 < 0) \cap (\xi_2 > 0)$ and $R_4 = (\xi_1 < 0) \cap (\xi_2 < 0)$. In brain MR images, R_1, R_2 and R_3 regions usually refer to WM, GM and CSF regions, respectively, and R_4 is an empty region, which is discarded.

Figure 5.13 shows the accuracy analysis of the regions of interest (i.e., WM, GM and CSF regions) in the brain MR images. A total of 100 2D slices from 20 brain anatomical models (Aubert-Broche, 2006) were used. Five 2D slices (namely 150, 175, 200, 225 and 250) from every patient were considered. The WM, GM and CSF regions are segmented using MLSF, VLSBCS, LSACM and the proposed methods. The accuracy of WM, GM and CSF regions for the mentioned four-phase active contour methods are computed using Eq. (5.21). In Eq. (5.21), A is the computed WM, GM or CSF region and B is the respective ground truth.

Figure 5.13 and Table 5.6 show that the proposed method yields the best segmentation results for GM and CSF regions. In turn, MLSF yields the best segmentation results for the WM region with an accuracy of 92.52%. The proposed method yields an accuracy of 91.02% for the WM region, which is 1.5% less than the one with the MLSF method. LSACM and VLSBCS yield unsatisfactory segmentation results compared to both the proposed method and MLSF. Table 5.6 also shows the CPU time comparison between the evaluated methods. MLSF is the quickest among the compared four-phase active contour methods. It took an average of 15.12 seconds to get the final segmentation result. In turn, the proposed method took an average of 19.01 seconds to fully converge, which is approximately 4 seconds more than the MLSF method. Both the mean and standard deviation (mean error) are considered for three brain regions, i.e., WM, GM, CSF.

Table 5.6: Segmentation accuracy of WM, GM and CSF regions using the four-phase active contour methods.

Method	WM	GM	CSF	CPU time (s)
MLSF	**92.52 ± 0.82**	85.84 ± 1.91	64.71 ± 0.94	**15.12**
VLSBCS	84.88 ± 1.37	73.22 ± 1.85	56.73 ± 1.02	18.33
LSACM	83.62 ± 1.36	75.43 ± 2.23	59.66 ± 1.90	91.30
Proposed	91.02 ± 0.33	**91.00± 0.54**	**79.73 ± 0.87**	19.01

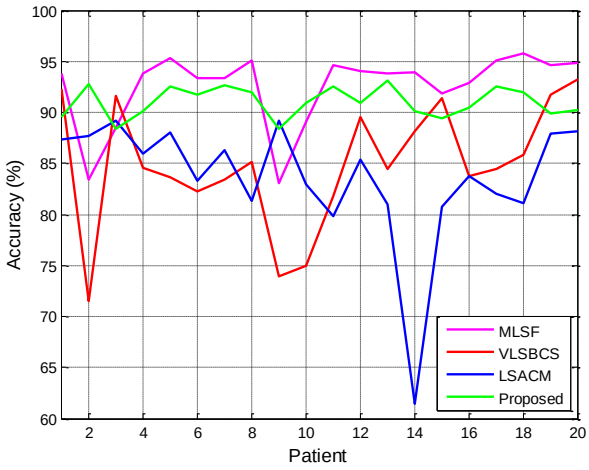

(a)

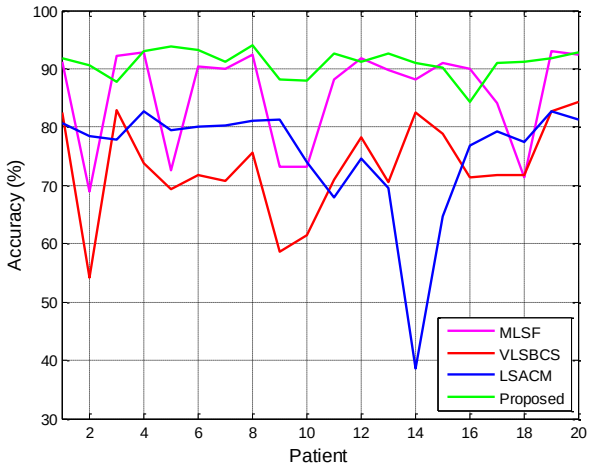

(b)

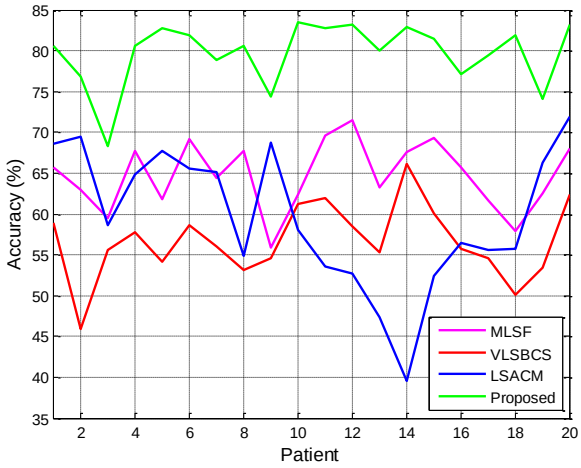

(c)

Figure 5.13: Segmentation accuracy analysis of (a) WM, (b) GM, and (c) CSF regions using four-phase active contours.

5.4.3 Comparison with brain MR image segmentation softwares

In this section, the segmentation results of the proposed method are compared with three alternative open source brain MR image segmentation softwares: SPM (Ashburner and Friston, 2005; Cuadra et al., 2005), LSF (Smith et al., 2004; Zhang et al., 2001) and BrainSuite (Shattuck and Leahy, 2002; Kasiri et al., 2010) using the Brain Web database. In order to compare the segmentation results, the brain region was extracted by stripping the skull using a brain mask. Figure 14 shows a skull stripped brain region and the visual comparison of the segmented regions with their respective ground truth. It shows that all the compared methods yield similar segmentation results from a qualitative point of view.

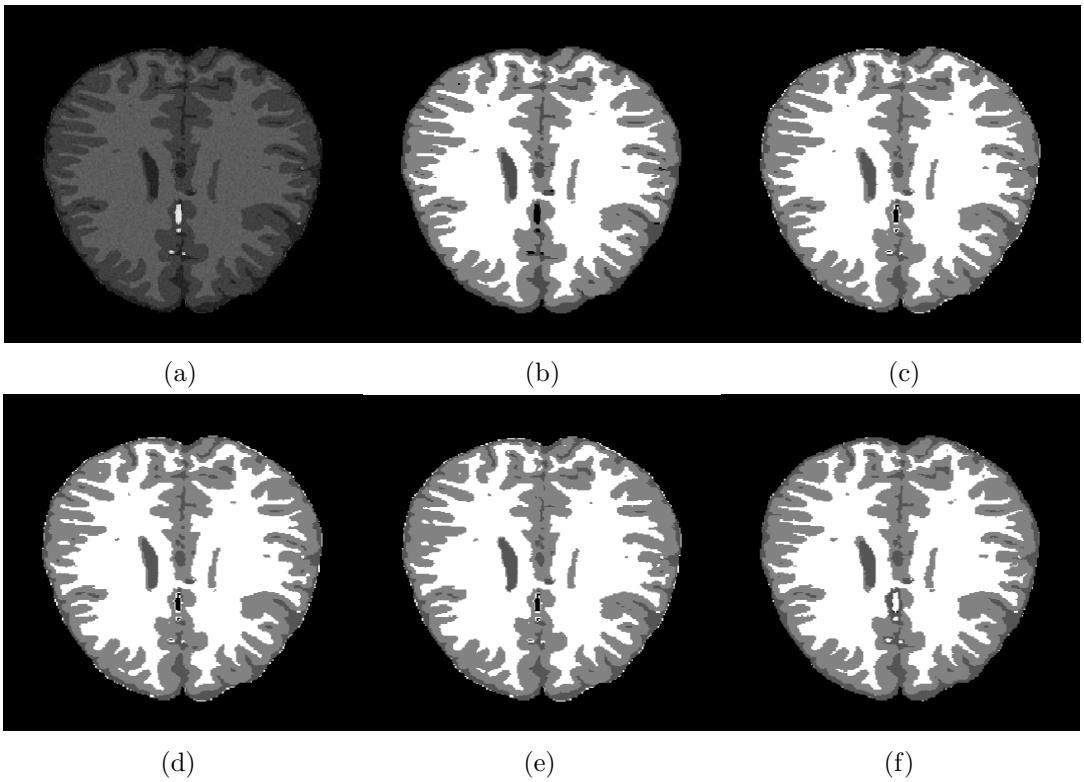

Figure 5.14: Visual comparison of the segmentation results of the proposed method with alternative brain MR image segmentation softwares. (a) Skull stripped brain image, (b) Ground truth (c) SPM, (d) FSL, (e) BrainSuite, and (f) Proposed method.

Table 5.7 shows the segmentation accuracy of the evaluated methods using two similarity metrics. Both the mean and standard deviation of the evaluated metrics

are considered for all three brain regions, i.e., WM, GM and CSF. These similarity metrics are the Jaccard index (Jaccard, 1912) and the Dice coefficient (Dice, 1945), which are frequently used when the ground truth of the regions of interest is available. These similarity metrics are defined as:

$$J(S,G) = \frac{|S \cap G|}{|S \cup G|},$$
$$D(S,G) = \frac{2|S \cap G|}{|S| + |G|} \tag{5.22}$$

where S is the segmented region and G its respective ground truth.

Table 5.7: Segmentation accuracy of WM, GM and CSF regions for the proposed method and the evaluated brain segmentation softwares.

Region	Brain segmentation softwares	Dice coefficient	Jaccard index
WM	SPM	0.95±0.02	0.90±0.03
	FSL	0.93±0.02	0.86±0.03
	BrainSuite	0.91±0.06	0.84±0.09
	Proposed	**0.96±0.01**	**0.92±0.02**
GM	SPM	0.93±0.02	0.87±0.04
	FSL	0.92±0.02	0.85±0.04
	BrainSuite	0.80±0.16	0.68±0.20
	Proposed	**0.94±0.01**	**0.88±0.02**
CSF	SPM	0.76±0.02	0.61±0.02
	FSL	0.74±0.06	0.60±0.02
	BrainSuite	0.46±0.16	0.31±0.08
	Proposed	**0.88±0.01**	**0.80±0.02**

Table 7 shows that the proposed method yields the best segmentation accuracy using both similarity measures for all three brain regions, i.e., WM, GM and CSF. For the GM region, if we consider the mean error (standard deviation) then the Dice coefficient computed using SPM is 0.95, which is the same as the proposed method. However, SPM yields a Jaccard index of 0.91, which is 0.01 more than the Jaccard index computed by the proposed method.

5.5 Summary

This chapter proposes a new region-based active contour method for image segmentation and bias correction by using an energy functional based on both local and global fitted images. In order to minimize that energy functional, the square image fitted difference is formulated by using both local and global fitted differences. In the gradient descent solution, both the local and global image differences are replaced by local and global signed pressure force (SPF) functions. Finally, a Gaussian kernel is applied to regularize the curve at each step and avoid the computationally expensive re-initialization.

The main contribution of this chapter is the formulation of a new energy functional from the LIF method (Zhang et al., 2010a) and the modification of the attained gradient descent solution with new SPF functions based on local and global fitted images to make the solution more stable. Qualitative and quantitative analysis show that the proposed method yields significantly better segmentation results and correction of homogeneous regions than alternative state-of-the-art methods. MR images have been used as a practical test bench.

In this chapter, the proposed method is also used to segment brain MR images into white matter (WM), gray matter (GM) and cerebrospinal fluid (CSF) regions. A two-phase method is limited to segmenting images into two regions, which is its big weakness in its application to brain MR image segmentation. Therefore, both two-phase and four-models are formulated to apply the proposed method in the application field of brain MR images.

CHAPTER 6

Brain MR image segmentation using multiphase active contours with pixel correction

6.1 Introduction

Brain MR imaging is a widely used imaging technology to study the brain anatomy and function. Segmentation of brain MR images into different disjoint regions: grey matter (GM), white matter (WM) and cerebrospinal fluid (CSF) can help physicians and doctors to carefully analyse head injuries, stroke, brain tumours and other brain diseases (Zhang et al., 2007). The study of segmented regions can also help psychiatrists to understand the development of different parts of the human brain

UNIVERSITAT ROVIRA I VIRGILI
AVANCES EN SISTEMAS INTERACTIVOS PARA PERSONAS CON PARÁLISIS CEREBRAL
Farhan Akram

with more detail, which is helpful to pinpoint the type of brain disorder.

Due to the geometric complexity of the human brain cortex, manual slice-by-slice segmentation is cumbersome and time consuming. Moreover, the complexity of intensity inhomogeneous regions makes brain MR images hard to segment with high accuracy (Balafar et al., 2010). Numerous methods have been devised to segment the brain into different non-overlapping regions (Elnakib et al., 2011). In particular, the active contour method introduced in (Kass et al., 1988) is widely-used for medical image segmentation. In this method, a curve evolves towards the boundaries of the objects of interest under a certain force field by minimizing the curve's intrinsic energy.

A multiphase level-set framework (MLSF) using n level-sets was proposed to segment a given image into 2^n phases (regions) (Vese and Chan, 2002). This method is an extension of a previous work on active contours without edges by Chan and Vese (2001), which was a two-phase segmentation method. It was developed under the assumption that the input image must have homogeneous intensity regions. Therefore, it does not properly work on images that contain inhomogeneous regions or with small intensity differences among different regions.

A variational level-set approach for bias correction and segmentation (VLSBCS) of images corrupted with intensity inhomogeneities was proposed by Li et al. (2008a, 2011). The computed bias field is intrinsically ensured to be smooth by the data term in the variational formulation, without any additional effect to maintain the smoothness of the bias field. In this work, the two-phase model is also extended to a four-phase approach.

A local statistical active contour model (LSACM) for image segmentation in the presence of intensity inhomogeneity was proposed by Zhang et al. (2016, 2015). In this method, inhomogeneous objects are modelled as Gaussian distributions of different means and variances. A statistical energy functional is then defined for each local region, which combines the bias field, the level-set function, and the constant approximating the true signal of the corresponding object. In this work, a four-phase energy functional is also formulated along with a two-phase model. Therefore, it is

suitable to segment brain MR images into the desired regions of interest i.e., WM, GM and CSF.

In this chapter, a four-phase region based active contour method is proposed to segment brain MR images into three regions of interests i.e., WM, GM and CSF. In the proposed energy functional, two different two-phase fitted image differences are multiplied to formulate a squared fitted image difference, which reduces the mathematical complexity of a four-phase model. The local intensity averages, which are used to construct image differences, are computed by introducing a Gaussian kernel to smooth the two-phase piecewise approximation of Chan and Vese (2001) method. Moreover, a post processing (pixel correction) algorithm is also devised in this work. In this algorithm, averages of non-zero pixels of WM, GM and CSF regions are computed to construct the upper and lower bounds of the thresholding function. Based on the decided bounds of the threshold, each pixel is assigned a binary value (0 or 1) to define new WM, GM and CSF regions. The experimental results of both 2D and 3D images show that the pixel correction algorithm improves the segmentation accuracy of WM, GM, CSF regions of all evaluated state-of-the-art methods. Therefore, it can widely be used to improve the accuracy of WM, GM and CSF regions of intensity-based brain MR image segmentation methods. The results also show that the proposed method always converges to yield acceptable segmentation results unlike the other evaluated methods.

The main contributions of this work are as follows:

- A hybrid region-based multiphase active contour model is proposed by integrating local and global fitted images in a multiplicative manner. The proposed method combines two different two-phase fitted images to formulate a four-phase model, which has not been exploited before.
- A post-processing (pixel correction) method is also proposed to increase the segmentation accuracy of the regions of interest (WM, GM and CSF regions).
- Local active contour methods are very sensitive to the initial position of the contour. The proposed method uses both local and global intensity means based fitted images, thus not being sensitive to the initial position of the

UNIVERSITAT ROVIRA I VIRGILI
AVANCES EN SISTEMAS INTERACTIVOS PARA PERSONAS CON PARÁLISIS CEREBRAL
Farhan Akram

contour.

- The proposed method is designed for both 2D and 3D brain MR image segmentation.

This chapter is organized as follows. The proposed method is described in section 6.2. The pixel correction algorithm to improve the segmentation accuracy is described in section 6.3. Experimental results for both 2D and 3D images are shown in section 6.4 using real brain magnetic resonance images. Finally, the chapter is summarized in section 6.5.

6.2 Proposed method

The piecewise approximation model which approximates non-overlapping segments to a given image can be defined as:

$$I(x) = u(x) + n(x), \tag{6.1}$$

where $I(x)$ is the input image, $u(x)$ is the approximated image after segmentation, and $n(x)$ is noise.

A local image fitting energy functional is proposed by Zhang et al. (2010a) in which the difference between the fitted image and the original image is minimized. In this paper, a novel multiphase (four-phase) image segmentation method is proposed to partition a brain MR image into three distinct regions using an image fitting energy functional. Actually, four-phase active contours partition an image into four regions. However, the fourth region is discarded, since it contains unnecessary background information. The proposed four-phase fitted image (FFI) energy functional E_{FFI} is based on the product of two different two-phase fitted image differences to minimize the error, which is defined as follows:

$$E_{FFI} = E_{prop}(\Phi) + \mu L(\phi_i) + vA(\phi_i), \tag{6.2}$$

where Φ is the function which represents two level-sets (ϕ_1, ϕ_2), ϕ_i is an i^{th} level-set curve and $i = 1, 2$. $\mu \geq 0$, $v \geq 0$ are fixed parameters. E_{prop} is the proposed four-phase energy functional, which is defined later in this section. $L(\phi_i)$ and $A(\phi_i)$ are length and area terms, respectively. $L(\phi_i)$ regularizes the curve and $A(\phi_i)$ smoothes the object to speed up the curve evolution. $L(\phi_i)$ and $A(\phi_i)$ be defined as:

$$L(\phi_i) = \int_{\Omega} |\nabla H_\epsilon(\phi_i)| dx, \tag{6.3}$$

$$A(\phi_i) = \int_{\Omega} H_\epsilon(\phi_i) dx, \tag{6.4}$$

Let $I : \Omega \to \mathbf{R}^2$ be the input image, $I_{GFI}(x)$ the global fitted image for the level set ϕ_1 and $I_{LFI}(x)$ the local fitted image for the level set ϕ_2. An energy functional for the proposed four-phase fitted image segmentation model E_{prop} can then be defined as:

$$E_{prop}(\Phi) = \frac{1}{2} \int_{\Omega} \big(I(x) - I_{GFI}(x)\big)\big(I(x) - I_{LFI}(x)\big) dx, \qquad x \in \Omega \tag{6.5}$$

where $I_{GFI}(x)$ and $I_{LFI}(x)$ are two-phase global and local fitted images for ϕ_1 and ϕ_2, respectively, which are defined as:

$$I_{GFI}(x) = c_1 M_1(\phi_1(x)) + c_2 M_2(\phi_1(x)), \tag{6.6}$$

$$I_{LFI}(x) = f_1 M_1(\phi_2(x)), + f_2 M_2(\phi_2(x)), \tag{6.7}$$

where $M_1(\phi_1) = H_\epsilon(\phi_1)$, $M_2(\phi_1) = 1 - H_\epsilon(\phi_1)$, $M_1(\phi_2) = H_\epsilon(\phi_2)$ and $M_2(\phi_2) = 1 - H_\epsilon(\phi_2)$ are characteristic terms defined for both level-sets (ϕ_1 and ϕ_2) and $H_\epsilon(\phi)$

is the regularized version of the Heaviside function in Eq. (2.10). In Eqs. (6.6) and (6.7), (c_1, c_2) and (f_1, f_2) are global and local intensity means for level-sets ϕ_1 and ϕ_2, respectively, which are defined in Eqs. (2.13) and (2.19).

By using the calculus of variations and the steepest gradient descent (Aubert and Kornprobst, 2010), E_{prop} in Eq. (6.5) is minimized with respect to ϕ_1 and ϕ_2, leading to the corresponding gradient descent flows (refer to the appendix B.1 for a detailed derivation):

$$\frac{\partial \phi_1}{\partial t} = \big(I(x) - I_{LFI}(x)\big)(c_1 - c_2)\delta_\epsilon(\phi_1), \tag{6.8}$$

$$\frac{\partial \phi_2}{\partial t} = \big(I(x) - I_{GFI}(x)\big)(f_1 - f_2)\delta_\epsilon(\phi_2), \tag{6.9}$$

where $\delta_\epsilon(\phi)$ is the regularized Dirac function defined in Eq. (2.12). By using calculus of variations and applying steepest gradient descent (Aubert and Kornprobst, 2010), on E_{FFI} Eq. (6.2) following solutions of ϕ_1 and ϕ_2 are obtained:

$$\frac{\partial \phi_1}{\partial t} = \left(\big(I(x) - I_{LFI}(x)\big)(c_1 - c_2) + \mu \operatorname{div}\left(\frac{\nabla \phi_1}{|\nabla \phi_1|}\right) - v\right)\delta_\epsilon(\phi_1), \tag{6.10}$$

$$\frac{\partial \phi_2}{\partial t} = \left(\big(I(x) - I_{GFI}(x)\big)(f_1 - f_2) + \mu \operatorname{div}\left(\frac{\nabla \phi_2}{|\nabla \phi_2|}\right) - v\right)\delta_\epsilon(\phi_2), \tag{6.11}$$

A signed distance function (SDF) defined below is used for the initialization of the level-set functions:

$$\phi_i(x, t=0) = \begin{cases} -\rho, & x \in \Omega_i - \partial\Omega_i \\ 0, & x \in \partial\Omega_i \\ \rho, & x \in \Omega - \Omega_i \end{cases} \tag{6.12}$$

where $\rho > 0$ is a constant ($\rho = 1$ in this work). In Eq. (6.12), $t = 0$ and $i = 1, 2$ define the initial conditions of both level-set functions. Ω_i is the inner region of the initial level-set ϕ_i, Ω is the image domain and $\partial\Omega_i$ is the boundary of level-set ϕ_i.

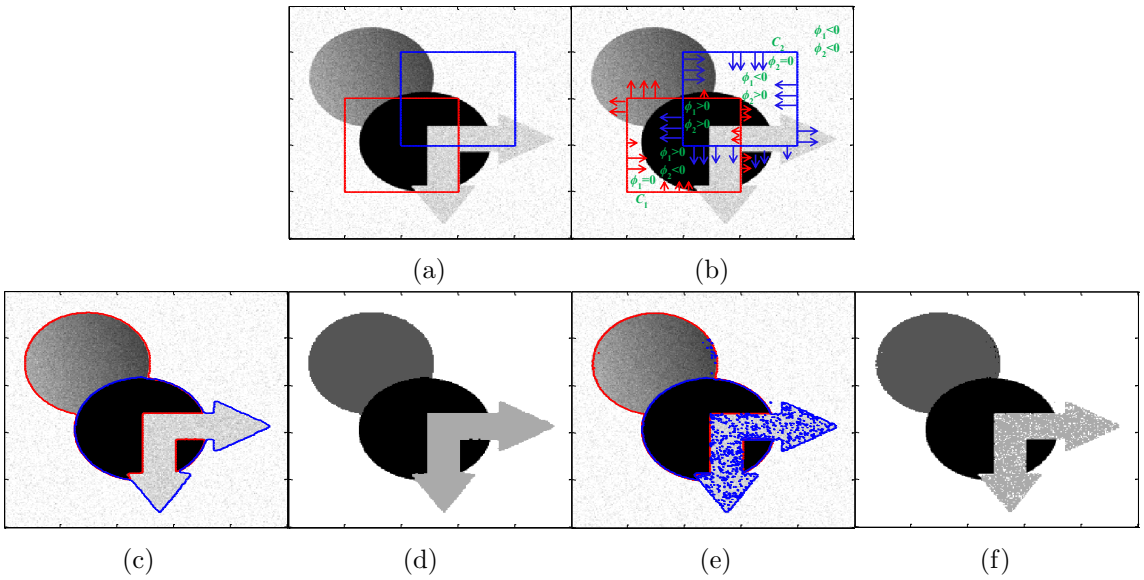

Figure 6.1: Four-phase image segmentation. (a) Initial contour. (b) Four regions and the flow of contour during evolution. Final contour: (c) proposed method and (e) MLSF. Segmentation results: (d) proposed method and (f) MLSF.

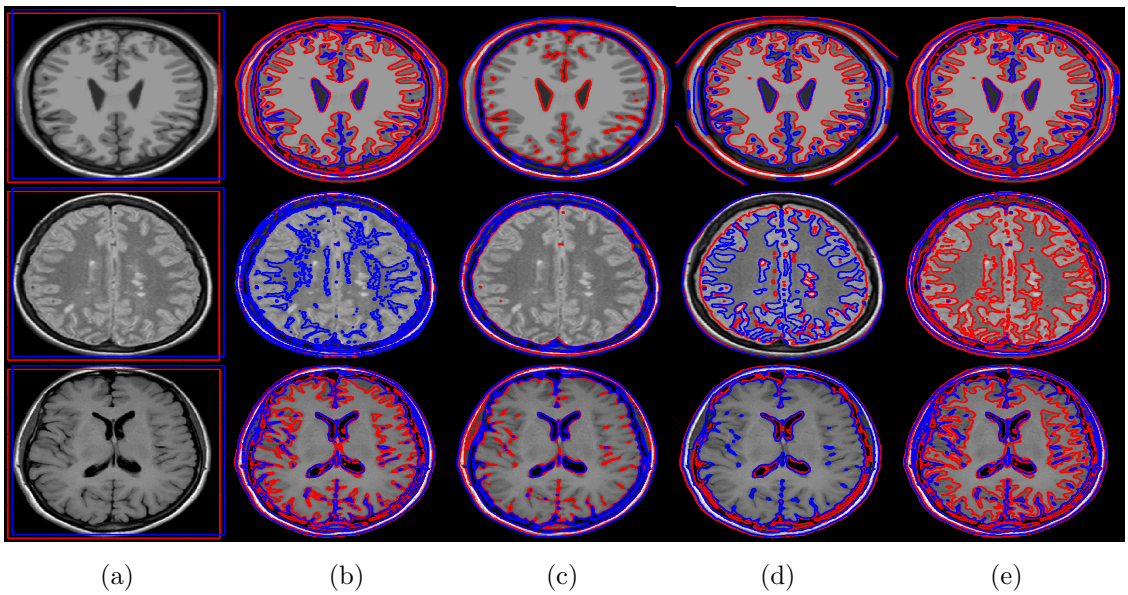

Figure 6.2: Four-phase segmentation comparison using a 2D brain MR image. (a) Initial contour, (b) MLSF, (c) VLSBCS, (d) LSACM, and (e) Proposed method.

Figure 6.1 shows how different regions are computed using the four-phase active contour methods. In this figure, a synthetic image with three objects is used, which

UNIVERSITAT ROVIRA I VIRGILI
AVANCES EN SISTEMAS INTERACTIVOS PARA PERSONAS CON PARÁLISIS CEREBRAL
Farhan Akram

is also affected by Poisson noise. Figure 6.1(b) shows how four regions are computed based on the different combinations of ϕ_1 and ϕ_2 in a four-phase active contour method. It also shows the flow of level-sets during the curve evolution process. At the boundary, ϕ_1 and ϕ_2 are zero, with contours C_1 and C_2 partitioning the image. Figure 6.1(c) and (e) show the final contour of the proposed method and MLSF, respectively. In turn, figure 6.1(d) and (f) show the final segmentation results of both methods, which concludes that the proposed method yields the best result in this case.

After evolving the level-set functions using Eqs. (6.10) and (6.11), they are regularized by using $\phi_i^k = G_\chi * \phi_i^k$, where $i = 1, 2$ represents the number of level-sets and k is the iteration number during the curve evolution. The regularization mentioned above not only regularizes the level-set functions, but also eliminates the need for re-initialization, which is computationally very expensive. Here, χ is the standard deviation of the Gaussian kernel used in the regularization process.

In this chapter, a new region-based active contour method is proposed for the four-phase image segmentation to partition a brain MR image into the WM, GM and CSF regions. Figure 6.2 shows the final four-phase segmentation result using the proposed and state-of-the-art methods. The proposed method segmented regions with more details, hence yielding better segmentation results.

In figure 6.3, a flow chart of the proposed segmentation algorithm is shown. A 2D brain MR image is first segmented using the proposed four-phase region-based active contour method. Then, the WM, GM and CSF regions are extracted from the final contour. After that, the proposed pixel correction method is used to increase the accuracy of the segmented WM, GM and CSF regions. The pixel correction method computes different thresholds using the intensity information from the segmentation result of the four-phase region-based active contour method. These thresholds are then used to correct the pixels of the WM, GM and CSF regions from the final contour.

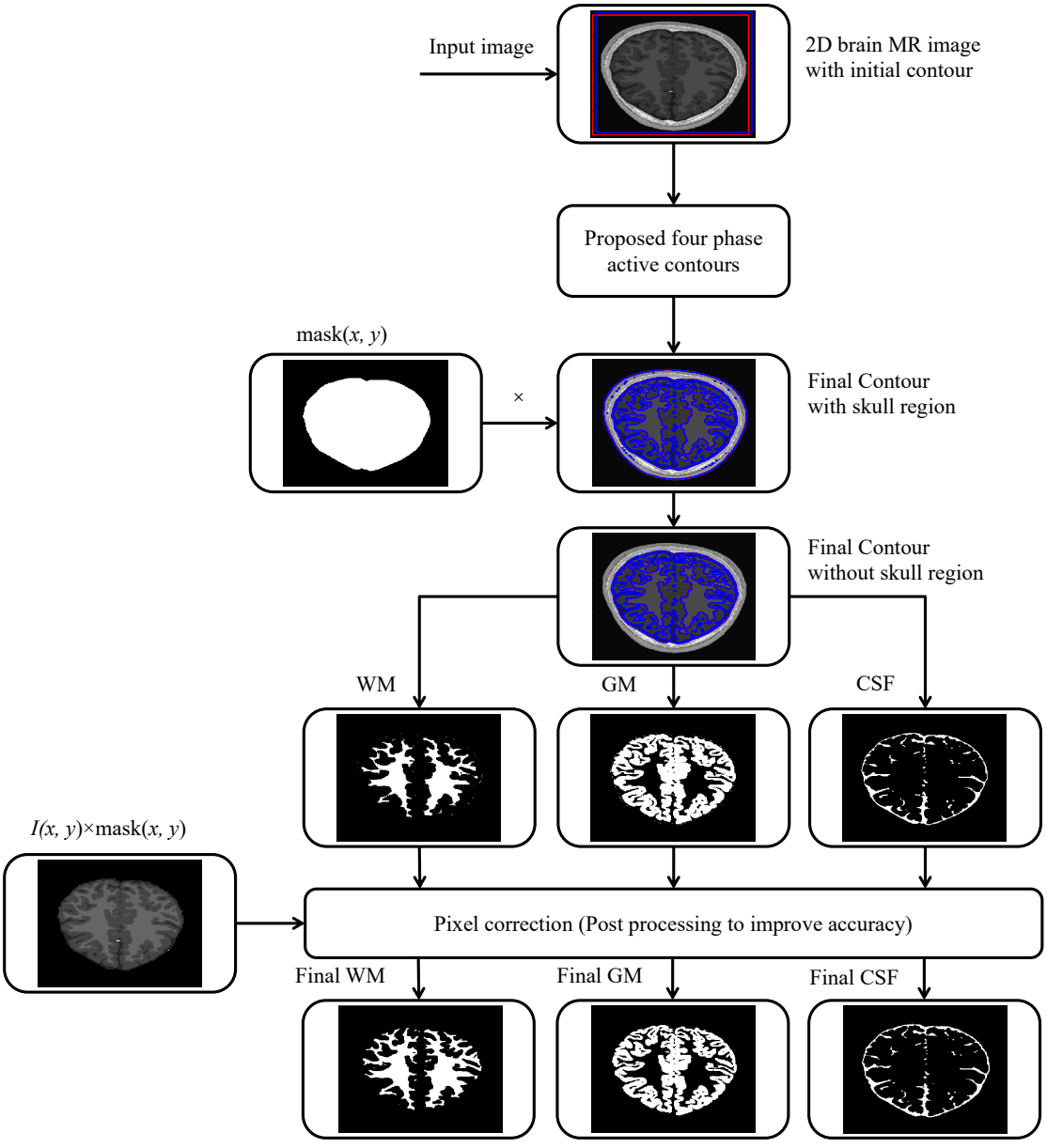

Figure 6.3: Brain MR image segmentation algorithm.

6.3 Pixel correction

In this section, a thresholding-based post processing (pixel correction) method is proposed to improve the accuracy of the segmented WM, GM and CSF regions in a brain MR image. The segmentation results obtained after the previous stage are modified according to a pixel correction algorithm based on simple thresholding. The WM, GM and CSF binary regions computed in the previous stage are intersected with the input grey-level image to compute the intensity average of their non-zero pixels. Here, non-zero regions are referring to the objects in an image (without background). These averages are then used to define a set of thresholds. If N is the number of rows and columns ($N = 250$ in this work), the intensity means corresponding to the three regions of interest are respectively defined as:

$$\overline{WM}(x,y) = \frac{\sum_{x=1}^{N}\sum_{y=1}^{N} I(x,y)WM(x,y)}{\sum_{x=1}^{N}\sum_{y=1}^{N} WM(x,y)}, \quad I(x,y) \neq 0 \tag{6.13}$$

$$\overline{GM}(x,y) = \frac{\sum_{x=1}^{N}\sum_{y=1}^{N} I(x,y)GM(x,y)}{\sum_{x=1}^{N}\sum_{y=1}^{N} GM(x,y)}, \quad I(x,y) \neq 0 \tag{6.14}$$

$$\overline{CSF}(x,y) = \frac{\sum_{x=1}^{N}\sum_{y=1}^{N} I(x,y)CSF(x,y)}{\sum_{x=1}^{N}\sum_{y=1}^{N} CSF(x,y)}, \quad I(x,y) \neq 0 \tag{6.15}$$

Different thresholds are decided by using the computed averages $\overline{WM}$, $\overline{GM}$ and $\overline{CSF}$ to construct new binary images for the WM, GM and CSF regions. Based on the decided bounds of the threshold, each pixel is assigned a binary value (0 or 1). The binary images corresponding to the regions of interest are finally defined as:

UNIVERSITAT ROVIRA I VIRGILI
AVANCES EN SISTEMAS INTERACTIVOS PARA PERSONAS CON PARÁLISIS CEREBRAL
Farhan Akram

$$WM(x,y) = \begin{cases} 1, & \frac{\overline{WM}}{2} + 128 > I(x,y) \geq \frac{\overline{WM}+\overline{GM}}{2} \\ 0, & \text{Otherwise} \end{cases} \tag{6.16}$$

$$GM(x,y) = \begin{cases} 1, & \frac{\overline{WM}+\overline{GM}}{2} > I(x,y) \geq \frac{\overline{GM}+\overline{CSF}}{2} \\ 0, & \text{Otherwise} \end{cases} \tag{6.17}$$

$$GM(x,y) = \begin{cases} 1, & \frac{\overline{GM}+\overline{CSF}}{2} > I(x,y) \geq \frac{\overline{CSF}}{2} \\ 0, & \text{Otherwise} \end{cases} \tag{6.18}$$

The pixel-corrected WM, GM and CSF regions have higher accuracy compared to the previously segmented regions and thus replace them. Detailed comparisons are shown in section 6.4.

6.4 Results

6.4.1 Two dimensional image segmentation

In this section, a 2D segmentation results are shown using the proposed method. Moreover, segmentation results of WM, GM and CSF regions are compared with the state-of-the-art method quantitatively. The proposed method was implemented using MATLAB and run on a 3.4 GHz Intel Core-i7 with 16 GB of RAM, testing it on real brain magnetic resonance (MR) images of 250×250 pixels with 256 grey levels (8bpp) (Cocosco et al., 1997; Aubert-Broche et al., 2006). The parameters used in all experiments in this section are: $\mu = 25$, $v = 175$, $\sigma = 3$, $\chi = 0.5$, $\epsilon = 1$ and time step $\tau = 0.001$.

Figure 6.4 shows 2D segmented WM, GM and CSF regions using the proposed method and their respective ground truths. It shows that the final contour is first computed using the proposed four-phase active contour method. Later, a brain

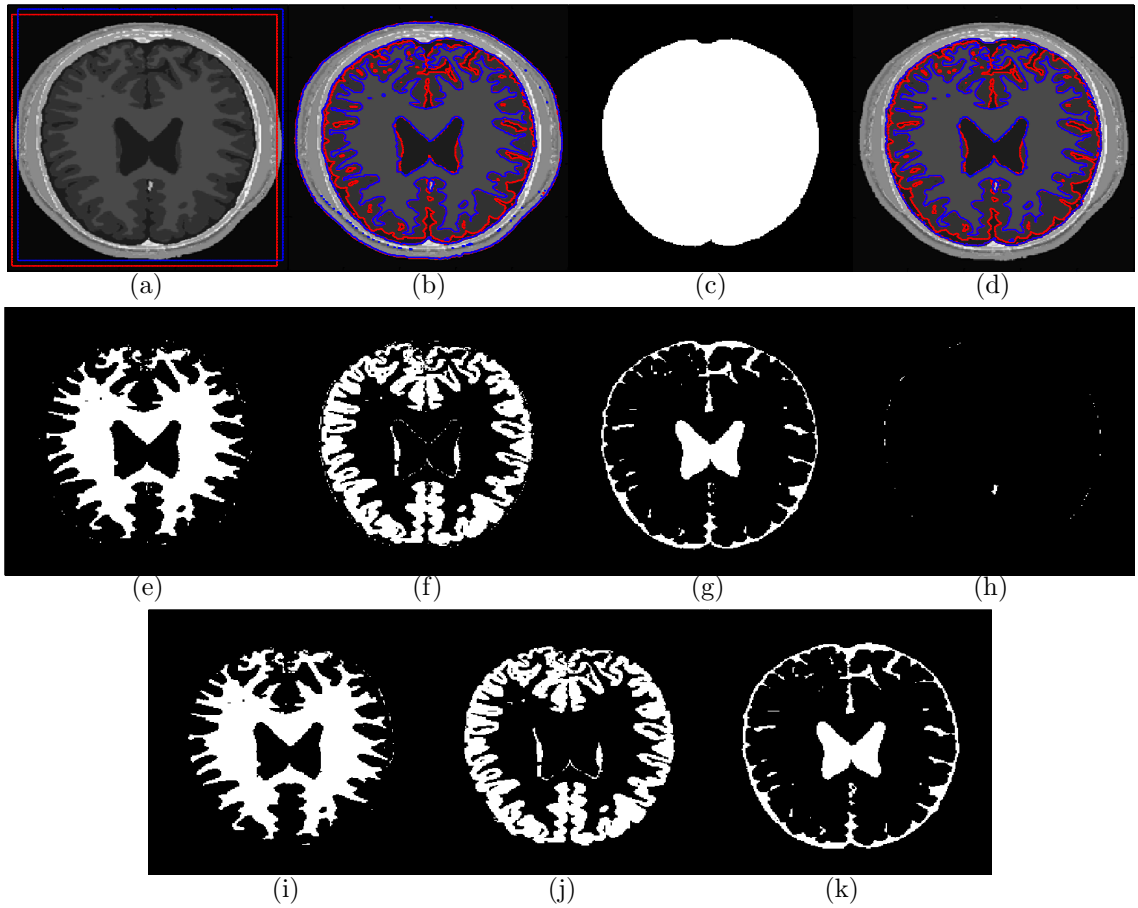

Figure 6.4: WM, GM and CSF regions computed using the proposed method. (a) Initial contour, (b) Final contour, (c) Brain region mask, (d) Final contour after scaling using brain mask, (e) Computed WM region, (f) Computed GM region, (g) Computed CSF region, (i) WM region ground truth, (j) GM region ground truth, and (k) CSF region ground truth.

mask is used to strip the skull region from the final contour information. Let ϕ_1 and ϕ_2 be the level-sets used for the four-phase active contour segmentation. Then, the four regions shown in figure 6.4(e)-(h) are computed according to the following combination: ($\phi_1 > 0$ and $\phi_2 < 0$), ($\phi_1 < 0$ and $\phi_2 > 0$), ($\phi_1 < 0$ and $\phi_2 < 0$) and ($\phi_1 > 0$ and $\phi_2 > 0$), respectively.

In this work, several metrics are used to evaluate the binary segmentation of an image. Let Ω_p be the set of all pixels in an image $I : \Omega \rightarrow \mathbf{R}^2$. The ground truth $G \in \Omega_p$ is a set of pixels of a particular region (WM, GM or CSF) labelled by an expert. Similarly, $S \in \Omega_p$ is a set of pixels of the region labelled by the proposed algorithm. The true positive (TP) set is defined as $TP = G \cap S$, which is the set of segmented brain regions common in both G and S. The true negative (TN) set

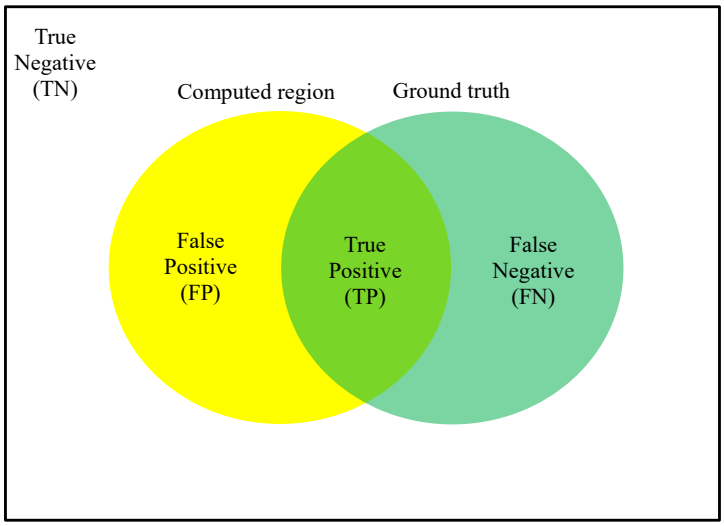

Figure 6.5: Region similarity between the segmented region and the ground truth yields the false positive, true positive, false negative and true negative areas.

is defined as $TN = \overline{G} \cap \overline{S}$, which is the set of segmented non-brain regions common in both G and S. Similarly, the false positive (FP) set is defined as $FP = \overline{G} \cap S$, which is the set of false pixels segmented as brain region not belonging to set G. In turn, the false negative (FN) is defined as $FN = G \cap \overline{S}$, which is the brain region missed by the proposed method during the segmentation process. Figure 6.5 shows the relationship of subsets: FP, FN, TP and TN for the given image with respect to G and S.

From these subsets, the success rates in terms of precision and recall are computed. In image segmentation, precision is the fraction of segmented region that is relevant to the regions of interest. In turn, recall is the fraction of segmented region relevant to the regions of interest that is successfully segmented. Both precision and recall are defined as:

$$\text{Precision} = \frac{TP}{TP + FP}, \qquad \text{Recall} = \frac{TP}{TP + FN} \tag{6.19}$$

The Jaccard index (JI) (Jaccard, 1912), the Dice similarity coefficient (DC) (Dice, 1945) and the Matthew's correlation coefficient (MCC) (Matthews, 1975) are similarity metrics frequently used in set comparison, that is, to compute the

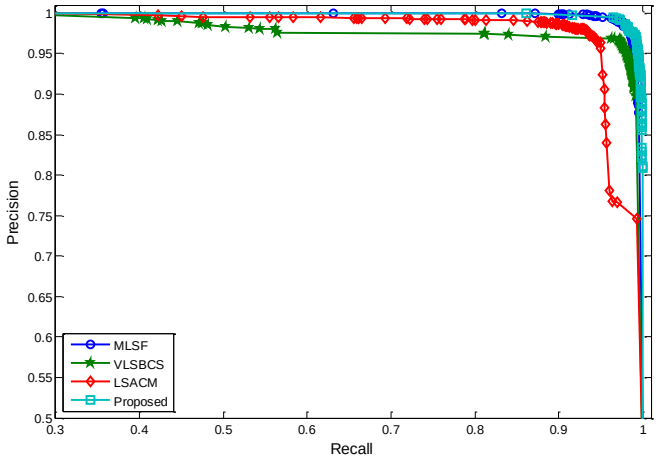

(a)

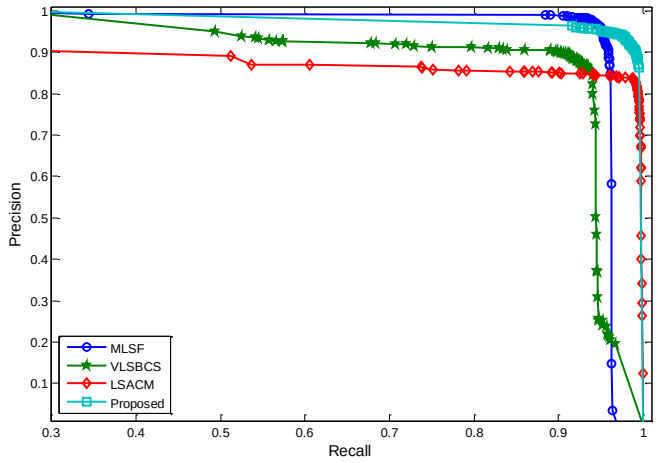

(b)

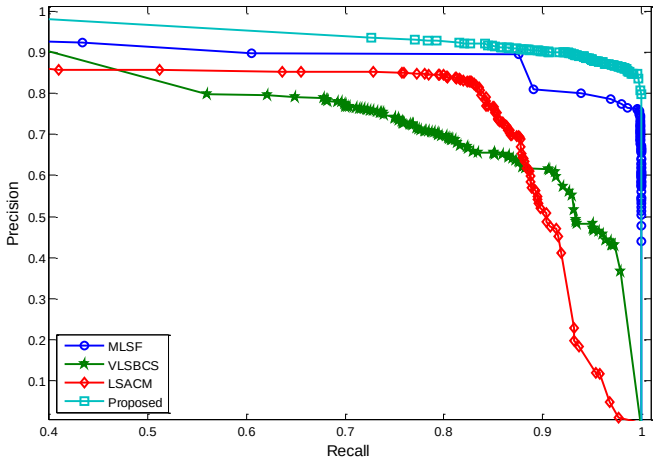

(c)

Figure 6.6: Segmentation accuracy comparison of the proposed method with the state-of-the-art. (a) WM region accuracy, (b) GM region accuracy, and (c) CSF region accuracy.

UNIVERSITAT ROVIRA I VIRGILI
AVANCES EN SISTEMAS INTERACTIVOS PARA PERSONAS CON PARÁLISIS CEREBRAL
Farhan Akram

segmentation accuracy when the ground truth of the region of interest is available. These metrics are defined as:

$$\text{JI} = \frac{TP}{TP + FP + FN} \times 100, \quad \text{DC} = \frac{TP}{\frac{1}{2}(TP + FN + TP + FP)} \times 100,$$
$$\text{MCC} = \frac{(TP \times TN) - (FP \times FN)}{\sqrt{(TP + FP)(TP + FN)(TN + FP)(TN + FN)}} \times 100 \tag{6.20}$$

In this work, the precision and recall (PR) curves are computed using Eq. (6.19) for the segmented WM, GM and CSF regions to demonstrate the robustness of the proposed method. In figure 6.6 and 6.7, PR curves of three regions of interest (WM, GM and CSF) are computed to show the segmentation accuracy rate of the proposed method and comparison with the state-of-the-art. For these experiments, 100 2D slices from 20 patients are used i.e., 5 slices (slice number 150, 175, 200, 225 and 250) for each patient.

Figure 6.6 shows the PR curves of WM, GM and CSF regions before applying the pixel correction algorithm. In figure 6.6(a), the PR curve of the WM region segmentation shows that in the proposed method and MLSF yield similar precision and recall points in average. The proposed method has some results with low precision but it ensures convergence. However, MLSF outperforms the proposed method, but figure 6.6(a) shows it has some results with very low recall, which concludes that it does not always converge. In figure 6.6(b) and (c), the PR curves of the GM and CSF regions show that the proposed method outperforms the compared state-of-the-art methods.

Table 6.1 shows a segmentation accuracy comparison of the WM, GM and CSF regions among the evaluated methods using the similarity metrics from Eq. (6.20) before applying the pixel correction algorithm. Both the mean and standard deviation (mean error) of the evaluated metrics are considered for all three brain regions, i.e., WM, GM and CSF. For the WM region, the MLSF method yields the highest values for all similarity metrics. For this region, the proposed method has a JI of 91.97%, DSC of 95.76% and MCC of 95.06%, which is 0.55%, 0.04% and

0.15% less than the respective values computed by the MLSF method. In turn, the proposed method yields the best results for all similarity metrics for both GM and CSF regions.

Table 6.1: Segmentation accuracy of the WM, GM and CSF regions with the tested methods using 2D slices.

Regions	Methods	JI	DSC	MCC
WM	MLSF	**92.52 ± 0.92**	**95.80± 0.67**	**95.21± 0.65**
	VLSBCS	84.88± 1.72	90.69± 1.23	89.84± 1.21
	LSACM	83.62 ± 1.30	90.46 ± 0.89	89.03 ± 0.95
	Proposed	91.97 ± 0.45	95.76 ± 0.25	95.06 ± 0.26
GM	MLSF	85.84 ± 1.96	90.34± 1.97	89.08± 1.94
	VLSBCS	73.22± 2.19	82.10 ± 1.95	79.21± 2
	LSACM	75.43 ± 1.43	84.99 ± 1.26	82.33 ± 1.40
	Proposed	**90.50 ± 0.23**	**95.00 ± 0.13**	**93.67 ± 0.16**
CSF	MLSF	64.71 ± 0.93	78.16 ± 0.74	78.97 ± 0.68
	VLSBCS	56.73± 0.81	72.05 ± 0.67	71.15 ± 0.59
	LSACM	59.66 ± 1.75	72.86 ± 1.74	72.54 ± 1.55
	Proposed	**82.69± 0.48**	**90.45± 0.30**	**89.82± 0.32**

Figure 6.7 shows the PR curves of the WM, GM and CSF regions after applying the pixel correction algorithm. In figure 6.7(a), the PR curve of the WM region segmentation shows that the proposed method yields low precision for some results compared to the other evaluated methods, but it has a high recall value for all results, which ensures that the algorithm will always converge. In turn, even though VLSBCS and LSACM have some results with higher precision than the proposed method, they also have some results with very low recall, which shows that they do not always converge. In figure 6.7(b), the PR curve of the GM region shows that the proposed method yields the best results and always converges, unlike the other methods. Figure 6.7(c) shows a PR curve of the CSF region, indicating that for some results, MLSF yields a high precision and for other results a low precision compared to the proposed method. However, the proposed method has more results with higher precision than MLSF. The PR curves in figure 6.7 show that after applying the pixel correction algorithm, the accuracy rates of all the evaluated methods are fairly increased compared to the PR curves in figure 6.6, which concludes that the proposed post processing (pixel correction) method works well on all four-phase

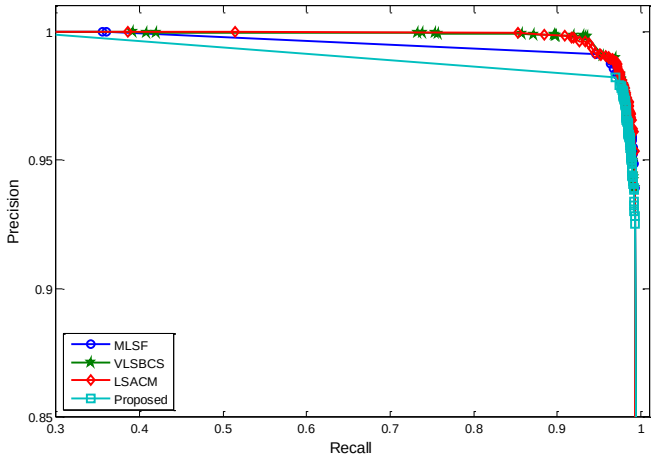

(a)

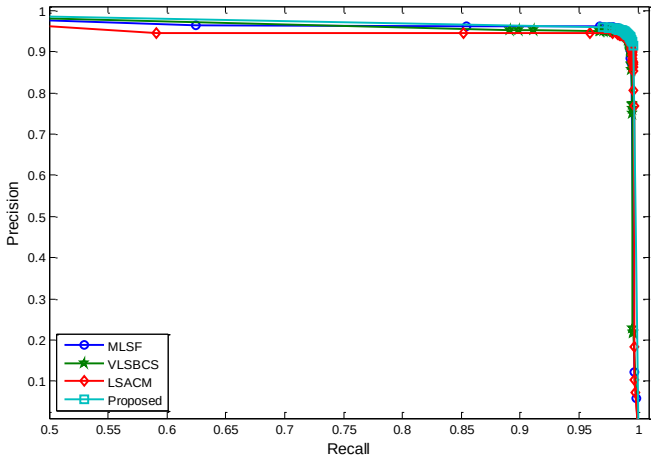

(b)

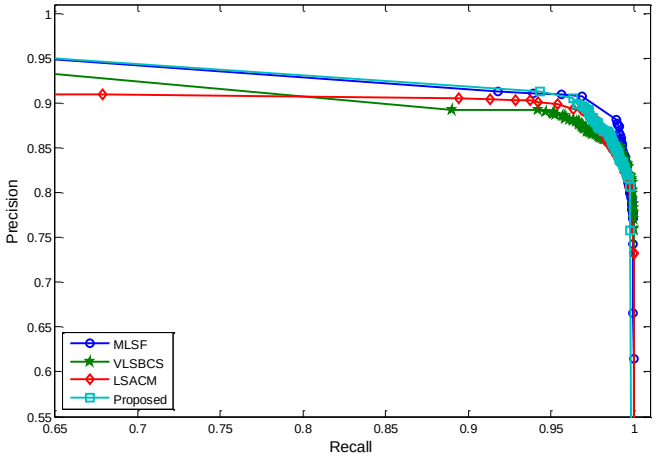

(c)

Figure 6.7: Segmentation accuracy comparison of the proposed method with the state-of-the-art after post processing (pixel correction with thesholding based approach). (a) WM region accuracy, (b) GM region accuracy, and (c) CSF region accuracy.

region-based active contour methods in the brain MR image segmentation problem.

Table 6.2: Segmentation accuracy of the WM, GM and CSF regions with the tested methods using 2D slices after applying pixel correction.

Regions	Methods	JI	DSC	MCC
WM	MLSF	94.14 ± 0.85	96.71 ± 0.63	96.21 ± 0.61
	VLSBCS	92.22 ± 1.01	95.58 ± 0.72	95.03 ± 0.69
	LSACM	94.32 ± 0.74	96.88 ± 0.52	96.38 ± 0.52
	Proposed	**94.59 ± 0.14**	**97.22 ± 0.07**	**96.64 ± 0.08**
GM	MLSF	91.71 ± 1.20	94.97 ± 1.14	94.20 ± 1.06
	VLSBCS	89.43 ± 1.26	93.73 ± 1.05	92.85 ± 0.96
	LSACM	88.71 ± 1.39	93.07 ± 1.30	92.18 ± 1.18
	Proposed	**93.41 ± 0.09**	**96.59 ± 0.05**	**95.69 ± 0.06**
CSF	MLSF	81.52 ± 0.38	89.77 ± 0.24	89.60 ± 0.22
	VLSBCS	83.75 ± 0.30	91.13 ± 0.18	90.79 ± 0.17
	LSACM	83.66 ± 0.78	90.81 ± 0.71	90.48 ± 0.67
	Proposed	**84.71 ± 0.26**	**91.70 ± 0.15**	**91.38 ± 0.15**

Table 6.2 shows a segmentation accuracy comparison of the WM, GM and CSF regions among the evaluated methods using the similarity metrics from Eq. (6.20) after applying the pixel correction algorithm. It shows that the proposed method yields the best values for all similarity metrics among the evaluated methods for all regions of interest i.e., WM, GM and CSF regions.

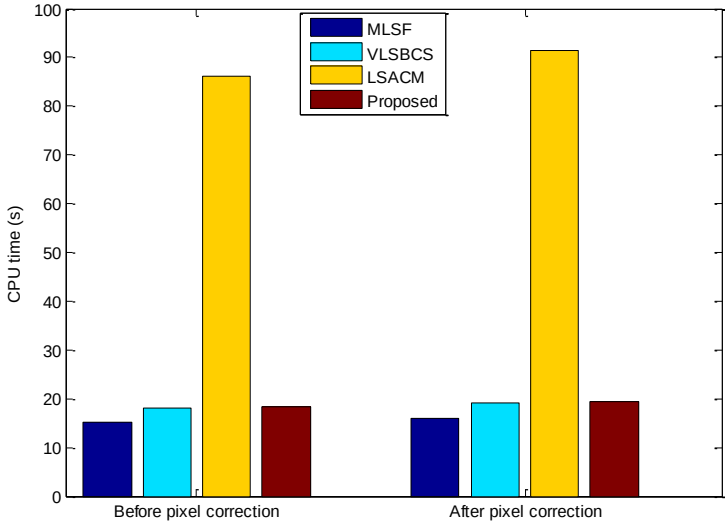

Figure 6.8: Average CPU time of the evaluated methods from figure 6.6 and figure 6.7.

Figure 6.8 shows that MLSF is the fastest among the evaluated methods. It took a CPU time of 15.12s and 16.03s for figure 6.6 and 6.7, respectively. In turn, the

proposed method took an average CPU time of 18.45s and 19.43s for both figures, respectively. MLSF is the fastest, although it not as accurate as the proposed method.

6.4.2 Volumetric data segmentation using 3D brain models

In this section, segmentation results of the proposed method and the state-of-the-art are compared using 3D brain MR models (Cocosco et al., 1997; Aubert-Broche et al., 2006). In all images, the range of intensities is represented from 0 to 255 grey levels, while the size in voxels ($length \times width \times height$) is ($250 \times 250 \times 362$). The parameters of the proposed method are the same as those given in section 6.4.1.

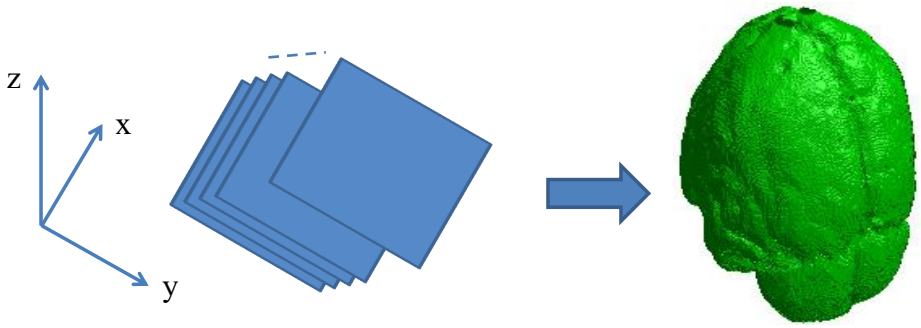

Figure 6.9: 3D volume reconstruction using 2D slices.

Figure 6.9 shows how a 3D volume is constructed using all 2D segmentation results from spatial brain MR data. After extracting 2D segmentation results from all slices, the 2D slices of a particular region of interest i.e., WM, GM and CSF are combined to construct their respective 3D volume.

In figure 6.10, a segmentation result of the WM region from the brain MR volumetric data is shown (before and after applying pixel correction). Figure 6.10(a) shows a segmented region using the proposed four-phase active contour method. In the top part of the segmented region, the edges are not fine and information seems scrambled as compared to the ground truth in figure 6.10(d). Figure 6.10(b) shows that the pixel correction algorithm is applied to the vertical slices to improve the segmentation accuracy. It is observed that the segmentation accuracy of the horizontal slices close to the skull is low for all of the evaluated methods. The

UNIVERSITAT ROVIRA I VIRGILI
AVANCES EN SISTEMAS INTERACTIVOS PARA PERSONAS CON PARÁLISIS CEREBRAL
Farhan Akram

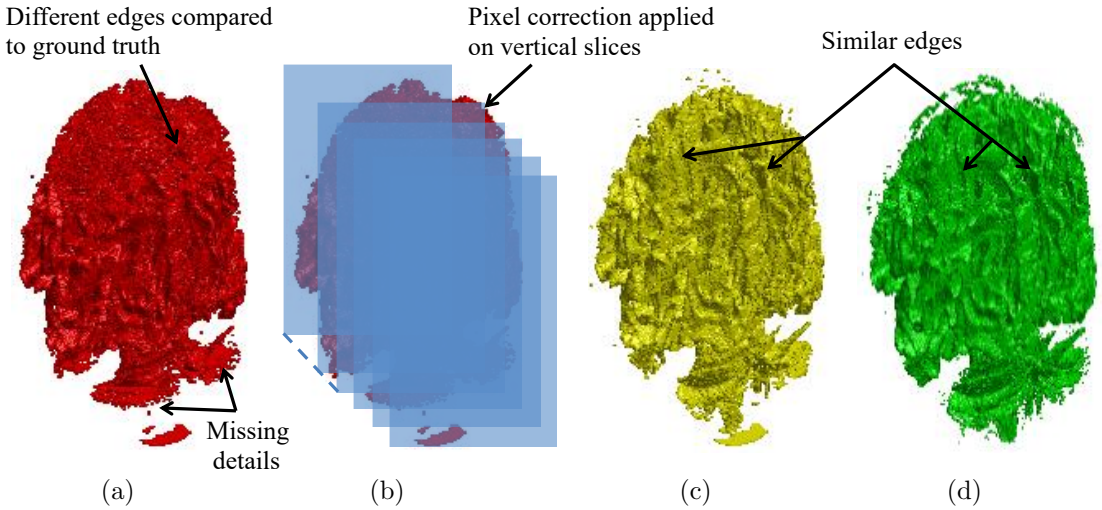

Figure 6.10: Pixel correction for the 3D MR images. (a) Segmented region before pixel correction, (b) Slice-by-slice pixel correction on the vertical slices, (c) Segmented region after pixel correction, and (d) Ground truth.

pixel correction algorithm works on the previous pixel information. If there is no information in the first horizontal slices, then it will not be able to update the wrong information in the next slices. However, if it is applied to the vertical slices, pixel intensity information from the upper slices can be used to update information in the first horizontal slices (which have high noise and almost no information). In figure 6.10(c), the segmented region after applying pixel correction has a high similarity with the ground truth in figure 6.10(d).

Figure 6.11 shows a 3D segmentation results of the WM, GM and CSF regions before and after applying the pixel correction algorithm. In figure 6.11, the segmentation results before applying pixel correction are shown in red. The segmentation results after applying pixel correction are shown in yellow. In turn, the ground truths of their respective regions are shown in green. It can be seen that the red WM, GM and CSF volumes are very noisy compared to their ground truths in green. In turn, the yellow WM, GM and CSF volumes, which are computed after applying the pixel correction, are much closer to the green ground truths (GT) and are less noisy compared to the red WM, GM and CSF regions. WM_1, GM_1 and CSF_1 are the segmented regions computed before pixel correction. WM_2, GM_2 and CSF_2 are the segmented regions computed after applying pixel correction. In turn,

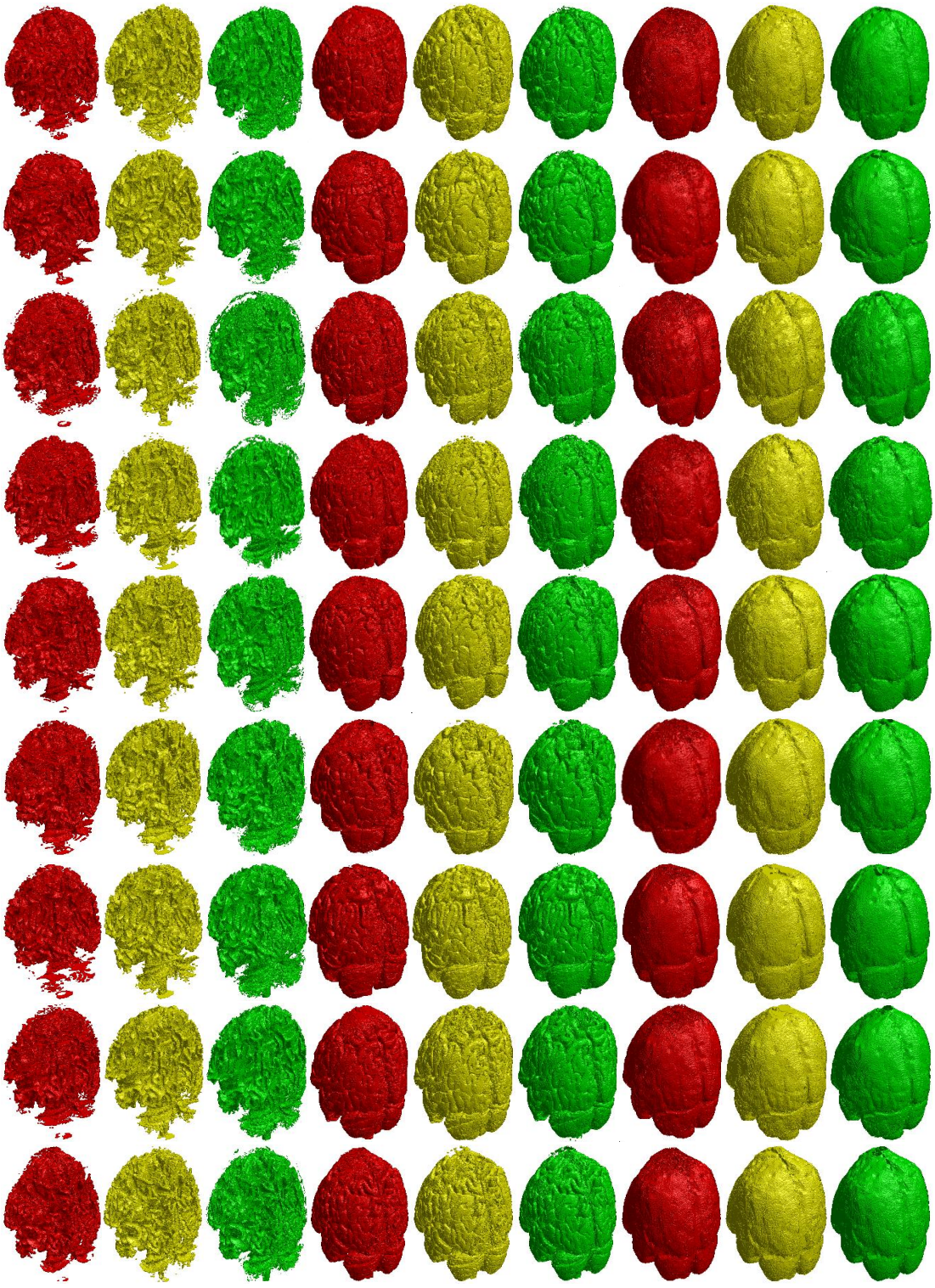

Figure 6.11: 3D segmentation of WM, GM and CSF regions using the proposed method (in red before and in yellow after pixel correction) and their respective ground truths (in green).

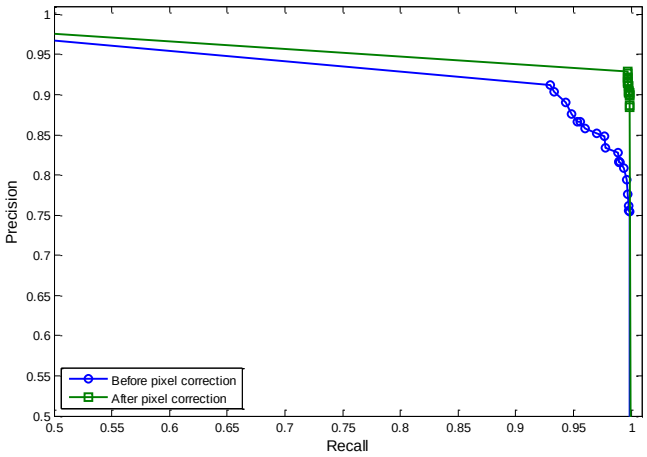

(a)

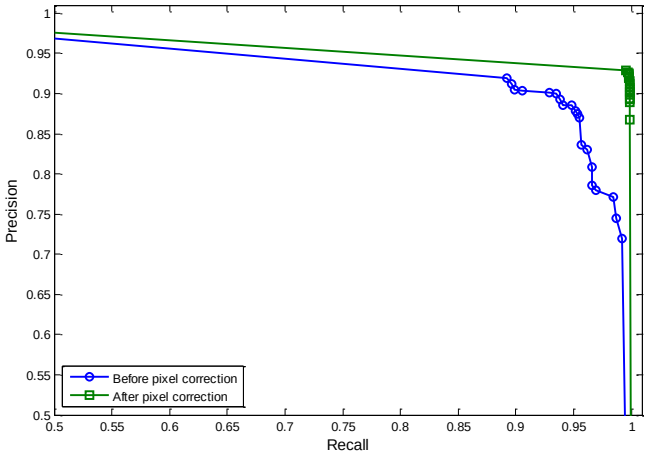

(b)

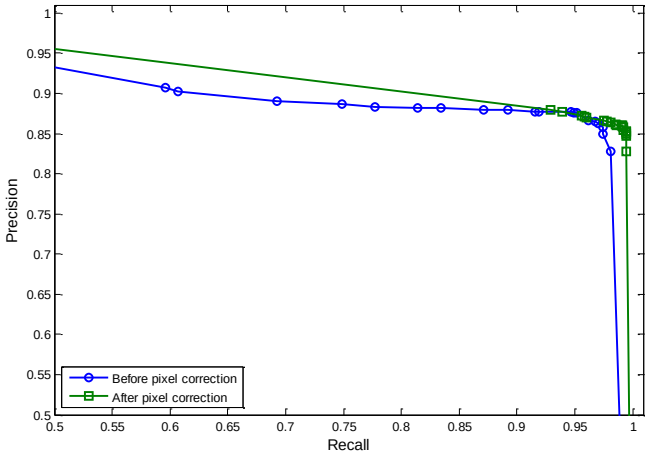

(c)

Figure 6.12: 3D segmentation accuracy of the WM, GM and CSF regions using 20 cases from the brain anatomical models. (a) WM region accuracy before and after applying pixel correction, (b) GM region accuracy before and after applying pixel correction, and (c) CSF region accuracy before and after applying pixel correction.

UNIVERSITAT ROVIRA I VIRGILI
AVANCES EN SISTEMAS INTERACTIVOS PARA PERSONAS CON PARÁLISIS CEREBRAL
Farhan Akram

WM_{GT}, GM_{GT} and CSF_{GT} are their respective ground truths.

Figure 6.12 shows the PR curves of the WM, GM and CSF regions using 3D volumetric data, as shown in figure 6.11, to compare the segmentation accuracy between the proposed active contour method before and after applying the pixel correction algorithm. The pixel correction algorithm distinctively improves the segmentation accuracy of the WM, GM and CSF regions, which is shown by the high accuracy differences among the PR curves in figure 6.12.

Table 6.3: 3D segmentation accuracy of the WM, GM and CSF regions before and after pixel correction.

Regions	Statistical measures	Proposed method without pixel correction	Proposed method with pixel correction
WM	JI	81.35 ± 1.07	**90.77 ± 0.28**
	DSC	89.65 ± 0.89	**95.16 ± 0.23**
	MCC	88.94 ± 0.85	**94.74 ± 0.22**
GM	JI	81.31 ± 1.37	**90.81 ± 0.35**
	DSC	89.51 ± 1.16	**95.17 ± 0.30**
	MCC	87.78 ± 1.11	**94.42 ± 0.27**
CSF	JI	77.09 ± 0.39	**84.46 ± 0.26**
	DSC	86.68 ± 0.32	**91.56 ± 0.22**
	MCC	85.99 ± 0.30	**91.25 ± 0.21**
CPU time (s)		**2.87** $\times 10^3$	2.88×10^3

Table 6.3 shows that after applying pixel correction the proposed method improves the results of similarity metrics (JI, DSC and MCC) by 9.42%, 5.51% and 5.8% for the WM region, 9.5%, 5.66% and 6.64% for the GM region and 7.37%, 4.88% and 5.26% for the CSF region, respectively.

Figure 6.13 shows the segmented WM, GM and CSF regions of the brain MR volumetric data using different state-of-the art methods before and after applying the pixel correction algorithm. WM_1, GM_2 and CSF_1 refer to the segmented regions before applying pixel correction. In turn, WM_2, GM_2 and CSF_2 are the segmented regions obtained after applying pixel correction. Visually, it can be seen that the pixel correction algorithm significantly improves the segmentation results of all methods. Therefore, the proposed pixel correction method can be used in CAD systems of brain MR images to improve the end results.

Table 6.4 shows WM, GM and CSF region segmentation accuracy comparisons

Table 6.4: Segmentation accuracy comparison (using the set similarity metrics) of the WM, GM and CSF regions with state-of-the-art shown in figure 6.13.

Regions	Statistical measures	MLSF	VLSBCS	LSACM	Proposed
$\mathbf{WM_1}$	JI	75.57	73.97	43.43	**83.28**
	DSC	86.09	85.04	60.56	**90.88**
	MCC	84.60	83.52	58.30	**90.06**
$\mathbf{GM_1}$	JI	71.15	60.96	58.48	**84.58**
	DSC	83.14	75.74	73.80	**91.65**
	MCC	80.76	72.07	69.13	**90.25**
$\mathbf{CSF_1}$	JI	57.81	50.64	38.70	**82.43**
	DSC	73.27	67.23	55.80	**90.37**
	MCC	71.48	64.88	52.75	**89.83**
$\mathbf{WM_2}$	JI	92.91	92.72	**93.37**	91.73
	DSC	96.32	96.22	**96.57**	95.69
	MCC	95.98	95.86	**96.22**	95.33
$\mathbf{GM_2}$	JI	88.76	88.70	86.56	**91.92**
	DSC	94.05	94.01	92.79	**95.79**
	MCC	93.16	93.10	91.80	**95.09**
$\mathbf{CSF_2}$	JI	82.67	82.48	80.38	**85.36**
	DSC	90.51	90.40	89.12	**92.10**
	MCC	90.02	89.90	88.49	**91.85**
CPU time (s)		**2.62**$\times 10^3$	5.31×10^3	17.47×10^3	2.83×10^3

Figure 6.13: Comparison of volumetric segmentation results of WM, GM and CSF regions. Segmentation results using MLSF (first row), VLSBCS (second row), LSACM (third row), and proposed method (last row), respectively.

with the state-of-the-art methods from figure 6.13 using the three similarity metrics: JI, DSC and MCC. The proposed method yields the best values for all similarity measures for all three regions i.e., WM, GM and CSF before applying pixel correction. The LSACM method yields the best results for the WM region after applying pixel correction. For the WM region, it shows that the proposed method yields values of 91.73%, 95.69% and 95.33% for JI, DSC and MCC, respectively, which is 1.64%, 0.88% and 0.89% less than the respective values attained by the LSACM method. In turn, the proposed method yields the best values for the GM and CSF region, after applying pixel correction. Table 6.4 shows MLSF yields the lowest time complexity,

UNIVERSITAT ROVIRA I VIRGILI
AVANCES EN SISTEMAS INTERACTIVOS PARA PERSONAS CON PARÁLISIS CEREBRAL
Farhan Akram

although it has a low accuracy for all regions compared to the proposed method.

6.5 Summary

Segmenting brain MR image into three different disjoint regions i.e., WM, GM and CSF is beneficial from various medical and psychological perspectives. In this chapter, a four-phase active contour method is proposed to segment brain MR images into the WM, GM and CSF regions. The idea is to formulate a squared difference for the four-phase model by multiplying two different two-phase differences from the different level-sets, which helps to reduce the mathematical complexity of the model. Moreover, a post processing (pixel correction) method is proposed, which improves the accuracy of the segmented regions significantly. The results show that the developed pixel correction algorithm works properly for all state-of-the-art methods that have been evaluated. Therefore, it can be used to improve the segmentation results of the WM, GM and CSF regions from all intensity-based methods. The proposed method yields better segmentation accuracy both qualitatively and quantitatively than state-of-the-art methods for both 2D and 3D (volumetric data) images.

CHAPTER 7

Conclusions and future work

7.1 Conclusions

Intensity inhomogeneity is one of the well-known problems in image segmentation, which can significantly affect the accuracy of intensity-based image segmentation methods. In this thesis, novel edge-based and region-based active contour methods are proposed to segment intensity inhomogeneous images. In the second chapter, numerous active contour methods are discussed in detail. The energy functionals of different edge-based and region-based approaches are given. Moreover, both global and local models are discussed as subcategories of region-based active contour methods. This thesis has following four main contributions.

In chapter 3, a novel edge-based active contour method driven by the difference of Gaussians (DoG) function is proposed in the context of intensity inhomogeneous image segmentation. The DoG function uses differences of two smooth images

UNIVERSITAT ROVIRA I VIRGILI
AVANCES EN SISTEMAS INTERACTIVOS PARA PERSONAS CON PARÁLISIS CEREBRAL
Farhan Akram

to extract edge information in an image. It acts as a balloon force in the energy functional to evolve the level-set curve, which consequently segments the global structure of the given image. In the proposed formulation, the internal energy term penalizes the deviation of the level-set function from a signed distance function (SDF), whereas the external energy term evolves the contour towards the boundaries of the objects. The results show that the proposed method yields the best segmentation results using both synthetic and real images as compared to the discussed state-of-the-art methods. Moreover, it yields the lowest CPU time among the compared methods.

In chapter 4, a retrospective region-based active contour method is proposed to both segment and correct intensity inhomogeneity. A phase stretch transform (PST) kernel is used to redefine the image intensity means and bias field. A bias fitted image is defined and used to formulate an energy functional. Moreover, the final gradient descent solution is stabilized using a proposed biased signed pressure force (bSPF) function. Finally, the level-set curve is regularized using a Gaussian kernel, which also removes the need for computationally expensive re-initialization. The proposed method is compared with the state-of-the-art retrospective active contour methods both qualitatively and quantitatively, concluding that it yields the best segmentation and bias correction results.

This chapter has four major contributions. First, new local intensity means and bias field term are computed using a PST kernel. Second, a bias fitted image is defined and a new energy functional based on that fitted image is formulated. Third, a biased fitted image-based signed pressure force (SPF) function is defined to stabilize the gradient descent solution. Lastly, a Gaussian kernel is used to regularize the level-set curve, which removes the computationally expensive re-initialization step and makes the algorithm insensitive to the initial position of the level-set curve.

In chapter 5, a new retrospective region-based active contour method is proposed for both image segmentation and bias correction by using an energy functional based on both local and global fitted images. In order to minimize that energy functional, the square image fitted difference is formulated by using both local and global

UNIVERSITAT ROVIRA I VIRGILI
AVANCES EN SISTEMAS INTERACTIVOS PARA PERSONAS CON PARÁLISIS CEREBRAL
Farhan Akram

fitted differences. In the gradient descent solution, both the local and global image differences are replaced by local and global signed pressure force (SPF) functions. Finally, a Gaussian kernel is applied to regularize the curve at each step and avoid the computationally expensive re-initialization.

The main contribution of this chapter is the formulation of a new energy functional from the LIF method (Zhang et al., 2010a) and the modification of the attained gradient descent solution with new SPF functions based on local and global fitted images to make the solution more stable. In chapter 5, synthetic intensity inhomogeneous and real brain MR images have been used as a practical test bench for both quantitative and qualitative analysis. Both analysis show that the proposed method yields significantly better segmentation results and correction of inhomogeneous regions than alternative state-of-the-art methods.

Segmenting brain MR images into three different disjoint regions: white matter (WM), gray matter (GM) and cerebrospinal fluid (CSF) is beneficial from various medical and psychological perspectives. In chapter 6, a multiphase (four-phase) active contour method is proposed to segment brain MR images into WM, GM and CSF regions. The idea is based on formulating a squared difference for the four-phase model by multiplying two different two-phase differences from the different level-sets, which helps reduce the mathematical complexity of the model. Moreover, a post-processing (pixel correction) method is proposed, which improves the accuracy of the segmented regions significantly. The results show that the developed pixel correction algorithm properly works for all state-of-the-art methods. Therefore, it can be used to improve the segmentation results of the WM, GM and CSF regions obtained from all intensity-based methods. The proposed method yields better segmentation accuracy both qualitatively and quantitatively than the state-of-the-art methods for both 2D and 3D (volumetric data) images.

7.2 Future work

In chapter 3, an edge-based active contour method is proposed to segment intensity inhomogeneous images. A difference of Gaussians is used to obtain the edge

UNIVERSITAT ROVIRA I VIRGILI
AVANCES EN SISTEMAS INTERACTIVOS PARA PERSONAS CON PARÁLISIS CEREBRAL
Farhan Akram

information, which extracts the global structure of the given image. However, it cannot be used for region segmentation, which can be helpful in the area of medical image analysis for different applications, such as left and right ventricle segmentation in cardiac MR images, tumour extraction in breast mammograms and brain MR images, etc. Moreover, it is unable to correct intensity inhomogeneities because the energy functional is devised to segment the objects but not to correct them. In the future, we aim at formulating an edge-based active contour method with the following features:

- It can be used for selective segmentation by introducing a characteristic term to restrict the contour to the region of interest.
- It can both segment and correct intensity inhomogeneous images by introducing a bias field component in the energy functional.

In chapter 4, a new region-based active contour method for image segmentation and bias correction is proposed using an energy functional driven by a bias fitted image. The proposed method is able to segment the global structure of the image. However, it is unable to segment the selected region. In the future work, we aim at formulating a selective region segmentation method using active contours, which will be able to segment regions of interest (selected regions) in different medical imaging applications.

In chapter 5, a new region-based active contour method for image segmentation and bias correction is proposed by using an energy functional based on both local and global fitted images. In order to minimize that energy functional, the square image fitted difference is formulated by using both local and global fitted differences. One of the drawbacks of a local fitted region-based active contour method is its high time complexity. In the future work, we aim at formulating a new region-based active contour method by modifying the proposed energy functional in a way to reduce time complexity. In order to do that, we plan to integrate a phase-shift approach similar to the one proposed by Lee and Seo (2006).

In chapter 6, a multiphase region-based active contour method is proposed to segment the brain MR images into WM, GM and CSF regions. However, it is not able

to compute the bias field and correct the intensity inhomogeneous brain MR images, which is considered one of its limitations. Moreover, the local parameters increase the time complexity of the proposed method compared to the global segmentation methods. In the future work, we aim at formulating a new energy functional by introducing a bias field computational component. With it, our method will be able to overcome the aforementioned limitation for both 2D and 3D (volumetric) brain MR images.

7.3 Publications derived from this thesis

7.3.1 Journals

1. **Farhan Akram**, Miguel Angel Garcia, Domenec Puig, Active contours driven by local and global fitted image models for image segmentation robust to intensity inhomogeneity, *PLOS ONE*, 12(4):1–34, 2017.
   Impact factor: 3.057. Multidisciplinary sciences (Q1). (Akram et al., 2017).
2. **Farhan Akram**, Miguel Angel Garcia, Domenec Puig, Active contours driven by difference of Gaussians, *Journal of Visual Communication and Image Representation*, 2017 (Under revision).
   Impact factor: 1.530. Computer science, Information systems (Q2).
3. **Farhan Akram**, Miguel Angel Garcia, Domenec Puig, Brain MR Image Segmentation Using Multiphase Active Contours with Pixel Correction, *Applied sciences*, 2017 (Under revision).
   Impact factor: 1.726. Multidisciplinary sciences (Q2).

7.3.2 Conferences

1. **Farhan Akram**, Domenec Puig, Miguel Angel Garcia, Adel Saleh, Multiphase region-based active contours for semi-automatic segmentation of brain MRI images, *In VISAPP 2015 - Proceedings of the 10th International Conference on Computer Vision Theory and Applications*, Volume 1, Berlin, Germany,

11-14 March, 2015., pages 447–454. (Akram et al., 2015b).

2. Adel Saleh, Mohamed Abdel-Nasser, **Farhan Akram**, Miguel Angel Garcia, Domenec Puig, Analysis of temporal coherence in videos for action recognition. *In Image Analysis and Recognition - 13th International Conference, ICIAR 2016*, Portugal, July 13-15, 2016, Proceedings, pages 325–332. (Saleh et al., 2016a).
3. Adel Saleh, Miguel Angel Garcia, **Farhan Akram**, Mohamed Abdel-Nasser, Domenec Puig, Exploiting the kinematic of the trajectories of the local descriptors to improve human action recognition. *In Proceedings of the 11th Joint Conference on Computer Vision, Imaging and Computer Graphics Theory and Applications (VISIGRAPP 2016)* Volume 3, Rome, Italy, February 27-29, 2016., pages 182–187. (Saleh et al., 2016b).
4. **Farhan Akram**, Miguel Angel Garcia, Vivel Kumar Singh, Nasibeh Saffari, Mostafa Kamal Sarker, Domenec Puig, Image segmentation using active contours driven by bias fitted image robust to intensity inhomogeneity, *Catalan conference on artificial intelligence (CCIA 2017).* (Submitted)
5. Mostafa Kamal Sarker, Maria Leyva, Adel Saleh, Vivek Kumar Singh, **Farhan Akram**, Petia Radeva, Domenec Puig, FoodPlaces: Learning Deep Features for Food Related Scene Understanding, *Catalan conference on artificial intelligence (CCIA 2017).* (Submitted)
6. Vivek Kumar Singh, Santiago Romani, Jordina Torrents-Barrena, **Farhan Akram**, Nindhi Pandey, Mostafa Kamal Sarker, Adel Saleh, Meritxell Arenas, Miguel Arquez, Domenec Puig, Classification of Breast Cancer Molecular Subtypes from their Micro-Texture in Mammograms using a VGGNet-Based Convolutional Neural Network, *Catalan conference on artificial intelligence (CCIA 2017).* (Submitted)

APPENDIX A

Derivations of active contours driven by local and global fitted image models

A.1 Derivation of the gradient descent flow of the two-phase model

By using the definitions of two-phase local and global fitted images from Eqs. (5.7) and (5.8) in the energy functional $E_{_{LGFI}}$ defined in Eq. (5.6), the variation η is added to the level-set function ϕ such that $\phi = \tilde{\phi} + \epsilon\eta$. Keeping m_1, m_2, c_1, c_2 and $b(x)$

fixed, differentiating with respect to ϕ and letting $\epsilon \to 0$, we have:

$$\frac{\partial E_{_{LGFI}}}{\partial \phi} = \lim_{\epsilon \to 0} \frac{d}{d\epsilon} \Bigg(\frac{1}{2} \int_{\Omega} \Big(I - b\big(m_1 H_\epsilon(\tilde{\phi}) + m_2(1 - H_\epsilon(\tilde{\phi}))\big)\Big) \Big(I - \big(c_1 H_\epsilon(\tilde{\phi}) + c_2(1 - H_\epsilon(\tilde{\phi}))\big)\Big) dx \Bigg)$$

$$= \frac{1}{2} \lim_{\epsilon \to 0} \Bigg(- \int_{\Omega} \Big[\Big(I - b\big(m_1 H_\epsilon(\tilde{\phi}) + m_2(1 - H_\epsilon(\tilde{\phi}))\big)\Big)(c_1 - c_2) - b\Big(I - \big(c_1 H_\epsilon(\tilde{\phi}) + c_2(1 - H_\epsilon(\tilde{\phi}))\big)\Big)(m_1 - m_2)\Big] \delta_\epsilon(\tilde{\phi}) \eta dx \Bigg)$$

$$= \frac{1}{2} \lim_{\epsilon \to 0} \Bigg(- \int_{\Omega} \Big[\Big(I - b\big(m_1 H_\epsilon(\phi) + m_2(1 - H_\epsilon(\phi))\big)\Big)(c_1 - c_2) - b\Big(I - \big(c_1 H_\epsilon(\phi) + c_2(1 - H_\epsilon(\phi))\big)\Big)(m_1 - m_2)\Big] \delta_\epsilon(\phi) \eta dx \Bigg)$$

The following Euler Lagrange equation is obtained:

$$- \Big[\Big(I - b\big(m_1 H_\epsilon(\phi) + m_2(1 - H_\epsilon(\phi))\big)\Big)(c_1 - c_2) + b\Big(I - \big(c_1 H_\epsilon(\phi) + c_2(1 - H_\epsilon(\phi))\big)\Big)(m_1 - m_2)\Big] \delta_\epsilon(\phi) = 0$$

By applying steepest gradient descent (Aubert and Kornprobst, 2010), the final gradient descent flow is obtained:

$$\frac{\partial \phi}{\partial t} = \Big[\Big(I - b\big(m_1 H_\epsilon(\phi) + m_2(1 - H_\epsilon(\phi))\big)\Big)(c_1 - c_2) + b\Big(I - \big(c_1 H_\epsilon(\phi) + c_2(1 - H_\epsilon(\phi))\big)\Big)(m_1 - m_2)\Big] \delta_\epsilon(\phi)$$

$$= \Big((I - I_{_{bLFI}})(c_1 - c_2) + b(I - I_{_{GFI}})(m_1 - m_2)\Big) \delta_\epsilon(\phi)$$

A.2 Derivation of the gradient descent flow of the four-phase model

By using the definitions of two-phase local and global fitted images from Eqs. (5.14) and (5.15) in the energy functional E_{LGFI} defined in Eq. (5.6), and adding the variations η_1 and η_2 to the level set functions ϕ_1 and ϕ_2, respectively, such that $\tilde{\phi_1} = \phi_1 + \epsilon\eta_1$ and $\tilde{\phi_2} = \phi_2 + \epsilon\eta_2$. Keeping m_1, m_2, m_3, m_4, c_1, c_2, c_3, c_4 and ϕ_2 fixed, differentiating with respect to ϕ_1 and letting $\epsilon \to 0$, we have:

$$
\begin{aligned}
\frac{\partial E_{LGFI}}{\partial \phi} = \lim_{\epsilon\to 0}\frac{d}{d\epsilon}\Bigg(\frac{1}{2}\int_{\Omega}\Big(I - b\big(m_1 H_\epsilon(\tilde{\phi_1})H_\epsilon(\tilde{\phi_2}) + m_2 H_\epsilon(\tilde{\phi_1})(1-H_\epsilon(\tilde{\phi_2}))\\
+ m_3(1-H_\epsilon(\tilde{\phi_1}))H_\epsilon(\tilde{\phi_2}) + m_4(1-H_\epsilon(\tilde{\phi_1}))(1-H_\epsilon(\tilde{\phi_2}))\big)\Big)\\
\Big(I - \big(c_1 H_\epsilon(\tilde{\phi_1})H_\epsilon(\tilde{\phi_2}) + c_2 H_\epsilon(\tilde{\phi_1})(1-H_\epsilon(\tilde{\phi_2}))\\
+ c_3(1-H_\epsilon(\tilde{\phi_1}))H_\epsilon(\tilde{\phi_2}) + c_4(1-H_\epsilon(\tilde{\phi_1}))(1-H_\epsilon(\tilde{\phi_2}))\big)\Big)dx\Bigg)
\end{aligned}
$$

$$
\begin{aligned}
= \frac{1}{2}\lim_{\epsilon\to 0}\Bigg(\int_{\Omega} -b\Big(I - \big(c_1 H_\epsilon(\tilde{\phi_1})H_\epsilon(\tilde{\phi_2}) + c_2 H_\epsilon(\tilde{\phi_1})(1-H_\epsilon(\tilde{\phi_2}))\\
+ c_3(1-H_\epsilon(\tilde{\phi_1}))H_\epsilon(\tilde{\phi_2}) + c_4(1-H_\epsilon(\tilde{\phi_1}))(1-H_\epsilon(\tilde{\phi_2}))\big)\Big)\\
\big((m_1-m_3)H_\epsilon(\tilde{\phi_2}) + (m_2-m_4)(1-H_\epsilon(\tilde{\phi_2}))\big)\\
- \Big(I - b\big(m_1 H_\epsilon(\tilde{\phi_1})H_\epsilon(\tilde{\phi_2}) + m_2 H_\epsilon(\tilde{\phi_1})(1-H_\epsilon(\tilde{\phi_2}))\\
+ m_3(1-H_\epsilon(\tilde{\phi_1}))H_\epsilon(\tilde{\phi_2}) + m_4(1-H_\epsilon(\tilde{\phi_1}))(1-H_\epsilon(\tilde{\phi_2}))\big)\Big)\\
\big((c_1-c_3)H_\epsilon(\tilde{\phi_2}) + (c_2-c_4)(1-H_\epsilon(\tilde{\phi_2}))\big)\delta_\epsilon(\tilde{\phi_1})\eta_1 dx\Bigg)
\end{aligned}
$$

$$
\begin{aligned}
&= \frac{1}{2}\lim_{\epsilon\to 0}\Bigg(\int_{\Omega} -b\Big(I - \big(c_1 H_\epsilon(\phi_1)H_\epsilon(\phi_2) + c_2 H_\epsilon(\phi_1)(1-H_\epsilon(\phi_2))\\
&+ c_3(1-H_\epsilon(\phi_1))H_\epsilon(\phi_2) + c_4(1-H_\epsilon(\phi_1))(1-H_\epsilon(\phi_2))\big)\Big)\\
&\big((m_1-m_3)H_\epsilon(\phi_2) + (m_2-m_4)(1-H_\epsilon(\phi_2))\big)\\
&- \Big(I - b\big(m_1 H_\epsilon(\phi_1)H_\epsilon(\phi_2) + m_2 H_\epsilon(\phi_1)(1-H_\epsilon(\phi_2))\\
&+ m_3(1-H_\epsilon(\phi_1))H_\epsilon(\phi_2) + m_4(1-H_\epsilon(\phi_1))(1-H_\epsilon(\phi_2))\big)\Big)\\
&\big((c_1-c_3)H_\epsilon(\phi_2) + (c_2-c_4)(1-H_\epsilon(\phi_2))\big)\delta_\epsilon(\phi_1)\eta_1 dx\Bigg)
\end{aligned}
$$

The following Euler Lagrange equation is obtained:

$$
\begin{aligned}
&-\Big[b\Big(I - \big(c_1 H_\epsilon(\phi_1)H_\epsilon(\phi_2) + c_2 H_\epsilon(\phi_1)(1-H_\epsilon(\phi_2)) + c_3(1-H_\epsilon(\phi_1))H_\epsilon(\phi_2)\\
&+ c_4(1-H_\epsilon(\phi_1))(1-H_\epsilon(\phi_2))\big)\Big)\big((m_1-m_3)H_\epsilon(\phi_2) + (m_2-m_4)(1-H_\epsilon(\phi_2))\big)\\
&+ \Big(I - b\big(m_1 H_\epsilon(\phi_1)H_\epsilon(\phi_2) + m_2 H_\epsilon(\phi_1)(1-H_\epsilon(\phi_2)) + m_3(1-H_\epsilon(\phi_1))H_\epsilon(\phi_2)\\
&+ m_4(1-H_\epsilon(\phi_1))(1-H_\epsilon(\phi_2))\big)\Big)\big((c_1-c_3)H_\epsilon(\phi_2)\\
&+ (c_2-c_4)(1-H_\epsilon(\phi_2))\Big]\delta_\epsilon(\phi_1) = 0
\end{aligned}
$$

By using the steepest gradient descent method (Aubert and Kornprobst, 2010), the final gradient descent flow obtained for ϕ_1 is:

$$
\begin{aligned}
\frac{\partial\phi_1}{\partial t} &= \Big[b\Big(I - \big(c_1 H_\epsilon(\phi_1)H_\epsilon(\phi_2) + c_2 H_\epsilon(\phi_1)(1-H_\epsilon(\phi_2)) + c_3(1-H_\epsilon(\phi_1))H_\epsilon(\phi_2)\\
&+ c_4(1-H_\epsilon(\phi_1))(1-H_\epsilon(\phi_2))\big)\Big)\big((m_1-m_3)H_\epsilon(\phi_2) + (m_2-m_4)(1-H_\epsilon(\phi_2))\big)\\
&+ \Big(I - b\big(m_1 H_\epsilon(\phi_1)H_\epsilon(\phi_2) + m_2 H_\epsilon(\phi_1)(1-H_\epsilon(\phi_2)) + m_3(1-H_\epsilon(\phi_1))H_\epsilon(\phi_2)\\
&+ m_4(1-H_\epsilon(\phi_1))(1-H_\epsilon(\phi_2))\big)\Big)\big((c_1-c_3)H_\epsilon(\phi_2)\\
&+ (c_2-c_4)(1-H_\epsilon(\phi_2))\Big]\delta_\epsilon(\phi_1)
\end{aligned}
$$

$$
\begin{aligned}
&= \Big[b\big(I - I_{GFI}\big)\big((m_1-m_3)H_\epsilon(\phi_2) + (m_2-m_4)(1-H_\epsilon(\phi_2))\big)\\
&+ \big(I - I_{bLFI}\big)\big((c_1-c_3)H_\epsilon(\phi_2) + (c_2-c_4)(1-H_\epsilon(\phi_2))\big)\Big]\delta_\epsilon(\phi_1)
\end{aligned}
$$

A.2. Derivation of the gradient descent flow of the four-phase model127

Similarly, keeping m_1, m_2, m_3, m_4, c_1, c_2, c_3, c_4 and ϕ_1 fixed, differentiating with respect to ϕ_2 and by the steepest gradient descent method (Aubert and Kornprobst, 2010), the following gradient descent flow for ϕ_2 is obtained:

$$\begin{aligned}\frac{\partial \phi_2}{\partial t} = &\Big[b\big(I - I_{_{GFI}}\big)\big((m_1 - m_2)H_\epsilon(\phi_1) + (m_3 - m_4)(1 - H_\epsilon(\phi_1))\big) \\ &+ \big(I - I_{_{bLFI}}\big)\big((c_1 - c_2)H_\epsilon(\phi_1) + (c_3 - c_4)(1 - H_\epsilon(\phi_1))\Big]\delta_\epsilon(\phi_2)\end{aligned}$$

UNIVERSITAT ROVIRA I VIRGILI
AVANCES EN SISTEMAS INTERACTIVOS PARA PERSONAS CON PARÁLISIS CEREBRAL
Farhan Akram

APPENDIX B

Derivations of multiphase active contours with pixel correction

B.1 Derivation of the gradient descent flow

In Eq. (6.5), the variation η_1 and η_2 are added to the level set functions ϕ_1 and ϕ_2, respectively, such that $\phi_1 = \tilde{\phi_1} + \epsilon\eta_1$ and $\phi_2 = \tilde{\phi_2} + \epsilon\eta_2$. Keeping c_1, c_2, f_1, f_2 and

ϕ_2 fixed and differentiating with respect to ϕ_1 (letting $\epsilon \to 0$), we have:

$$\begin{aligned}\frac{\partial E_{prop}}{\partial \phi_1} &= \lim_{\epsilon\to 0}\frac{d}{d\epsilon}\Bigg(\frac{1}{2}\int_{\Omega}\Big(I-\big(c_1H_\epsilon(\tilde{\phi_1})+c_2(1-H_\epsilon(\tilde{\phi_1}))\big)\Big)\\ &\qquad\Big(I-\big(f_1H_\epsilon(\tilde{\phi_2})+f_2(1-H_\epsilon(\tilde{\phi_2}))\big)\Big)dx\Bigg)\\ &= \frac{1}{2}\lim_{\epsilon\to 0}\Bigg(-\int_{\Omega}\Big(I-\big(f_1H_\epsilon(\tilde{\phi_2})+f_2(1-H_\epsilon(\tilde{\phi_2}))\big)\Big)\\ &\qquad(c_1-c_2)\delta_\epsilon(\tilde{\phi_1})\eta_1 dx\Bigg)\\ &= -\frac{1}{2}\Bigg(\int_{\Omega}\Big(I-\big(f_1H_\epsilon(\phi_2)+f_2(1-H_\epsilon(\phi_2))\big)\Big)(c_1-c_2)\delta_\epsilon(\phi_1)\eta_1 dx\Bigg)\end{aligned}$$

The following Euler Lagrange equation is obtained:

$$-\Big(I-\big(f_1H_\epsilon(\phi_2)+f_2(1-H_\epsilon(\phi_2))\big)\Big)(c_1-c_2)\delta_\epsilon(\phi_1)=0$$

By applying steepest gradient descent Aubert and Kornprobst (2010), the final gradient descent flow is obtained:

$$\begin{aligned}\frac{\partial \phi_1}{\partial t} &= \Big(I-\big(f_1H_\epsilon(\phi_2)+f_2(1-H_\epsilon(\phi_2))\big)\Big)(c_1-c_2)\delta_\epsilon(\phi_1)\\ &= \big((I-I_{LFI})(c_1-c_2)\big)\delta_\epsilon(\phi_1)\end{aligned}$$

Similarly, keeping c_1, c_2, f_1, f_2 and ϕ_1 fixed and differentiating with respect to ϕ_2 (letting $\epsilon \to 0$), we have:

$$\begin{aligned}\frac{\partial E_{prop}}{\partial \phi_2} &= \frac{1}{2}\lim_{\epsilon\to 0}\Bigg(-\int_{\Omega}\Big(I-\big(c_1H_\epsilon(\tilde{\phi_1})+c_2(1-H_\epsilon(\tilde{\phi_1}))\big)\Big)\\ &\qquad(f_1-f_2)\delta_\epsilon(\tilde{\phi_2})\eta_2 dx\Bigg)\\ &= -\frac{1}{2}\Bigg(\int_{\Omega}\Big(I-\big(c_1H_\epsilon(\phi_1)+c_2(1-H_\epsilon(\phi_1))\big)\Big)(f_1-f_2)\delta_\epsilon(\phi_2)\eta_2 dx\Bigg)\end{aligned}$$

The following Euler Lagrange equation is obtained:

$$-\Big(I-\big(c_1H_\epsilon(\phi_1)+c_2(1-H_\epsilon(\phi_1))\big)\Big)(f_1-f_2)\delta_\epsilon(\phi_2)=0$$

By applying steepest gradient descent Aubert and Kornprobst (2010), the final gradient descent flow is obtained:

$$\begin{aligned}\frac{\partial\phi_2}{\partial t}&=\Big(I-\big(c_1H_\epsilon(\phi_1)+c_2(1-H_\epsilon(\phi_1))\big)\Big)(f_1-f_2)\delta_\epsilon(\phi_2)\\&=\big((I-I_{GFI})(f_1-f_2)\big)\delta_\epsilon(\phi_2)\end{aligned}$$

UNIVERSITAT ROVIRA I VIRGILI
AVANCES EN SISTEMAS INTERACTIVOS PARA PERSONAS CON PARÁLISIS CEREBRAL
Farhan Akram

References

Akram, F., Garcia, M. A., and Puig, D. (2017). Active contours driven by local and global fitted image models for image segmentation robust to intensity inhomogeneity. *PLOS ONE*, 12(4):1–34.

Akram, F., Kim, J., Lee, C., and Choi, K. N. (2015a). Segmentation of regions of interest using active contours with SPF function. *Computational and Mathematical Methods in Medicine*, 2015:710326:1–710326:14.

Akram, F., Kim, J., Lim, H. U., and Choi, K. N. (2014). Segmentation of intensity inhomogeneous brain mr images using active contours. *Computational and Mathematical Methods in Medicine*, 2014:194614:1–194614:14.

Akram, F., Puig, D., García, M. A., and Saleh, A. (2015b). Multiphase region-based active contours for semi-automatic segmentation of brain MRI images. In *VISAPP 2015 - Proceedings of the 10th International Conference on Computer Vision Theory and Applications, Volume 1, Berlin, Germany, 11-14 March, 2015.*, pages 447–454.

Asghari, M. H. and Jalali, B. (2015). Edge detection in digital images using

UNIVERSITAT ROVIRA I VIRGILI
AVANCES EN SISTEMAS INTERACTIVOS PARA PERSONAS CON PARÁLISIS CEREBRAL
Farhan Akram

dispersive phase stretch transform. *International Journal of Biomedical Imaging*, 2015:687819:1–687819:6.

Ashburner, J. and Friston, K. J. (2005). Unified segmentation. *NeuroImage*, 26(3):839–851.

Aubert, G. and Kornprobst, P. (2010). *Mathematical Problems in Image Processing: Partial Differential Equations and the Calculus of Variations*. Springer Publishing Company, Incorporated, 2nd edition.

Aubert-Broche, B. (2006). *Brain web: Anatomical models of 20 normal brains*. http://brainweb.bic.mni.mcgill.ca/brainweb/anatomic_normal_20.html [Accessed: April 24, 2015].

Aubert-Broche, B., Griffin, M., Pike, G. B., Evans, A. C., and Collins, D. L. (2006). Twenty new digital brain phantoms for creation of validation image data bases. *IEEE Transactions on Medical Imaging*, 25(11):1410–1416.

Balafar, M. A., Ramli, A. R., Saripan, M. I., and Mashohor, S. (2010). Review of brain MRI image segmentation methods.

Barghout, L. and Sheynin, J. (2013). Real-world scene perception and perceptual organization: Lessons from computer vision. *Journal of Vision*, 13(9):709–709.

Batenburg, K. J. and Sijbers, J. (2009). Adaptive thresholding of tomograms by projection distance minimization. *Pattern Recognition*, 42(10):2297–2305.

Caselles, V., Catté, F., Coll, T., and Dibos, F. (1993). A geometric model for active contours in image processing. *Numerische Mathematik*, 66(1):1–31.

Caselles, V., Kimmel, R., and Sapiro, G. (1997). Geodesic Active Contours. *International Journal of Computer Vision*, 22(1):61–79.

Chan, T. F. and Vese, L. A. (2001). Active contours without edges. *IEEE Transactions on Image Processing*, 10(2):266–277.

Chen, L., da Cheng, H., and Zhang, J. (1994). Fuzzy subfiber and its application to seismic lithology classification. *Information Sciences - Applications*, 1(2):77–95.

Cocosco, C. A., Kollokian, V., Kwan, R. K.-S., Pike, G. B., and Evans, A. C. (1997). Brainweb: Online interface to a 3d mri simulated brain database. *NeuroImage*, 5:425.

Cuadra, M. B., Cammoun, L., Butz, T., Cuisenaire, O., and Thiran, J. P. (2005). Comparison and validation of tissue modelization and statistical classification methods in T1-weighted MR brain images. *IEEE Transactions on Medical Imaging*, 24(12):1548–1565.

Dice, L. R. . (1945). Measures of the Amount of Ecologic Association Between Species. *Ecology*, 26(3):297–302.

Elnakib, A., Gimel'farb, G., Suri, J. S., and El-Baz, A. (2011). Medical Image Segmentation: A Brief Survey. In *Multi Modality State-of-the-Art Medical Image Segmentation and Registration Methodologies*, volume 1, pages 235–280.

Evans, L. C. (1998). *Partial Differential Equations*, volume 19.

Guberman, S., Maximov, V. V., and Pashintsev, A. (2012). Gestalt and image understanding. *GESTALT THEORY*, 34(2):143–166.

Huang, C. and Zeng, L. (2015). An active contour model for the segmentation of images with intensity inhomogeneities and bias field estimation. *PLoS ONE*, 10(4):e0120399.

Huttenlocher, D. P., Klanderman, G. A., and Rucklidge, W. J. (1993). Comparing Images Using the Hausdorff Distance. *IEEE Transactions on Pattern Analysis and Machine Intelligence*, 15(9):850–863.

Ivanovska, T., Laqua, R., Wang, L., Schenk, A., Yoon, J. H., Hegenscheid, K., Völzke, H., and Liebscher, V. (2016). An efficient level set method for simultaneous intensity inhomogeneity correction and segmentation of MR images. *Computerized Medical Imaging and Graphics*, 48:9–20.

UNIVERSITAT ROVIRA I VIRGILI
AVANCES EN SISTEMAS INTERACTIVOS PARA PERSONAS CON PARÁLISIS CEREBRAL
Farhan Akram

Jaccard, P. (1912). The distribution of the flora in the alphine zone. *The New Phytologist*, XI(2):37–50.

Kahali, S., Adhikari, S. K., and Sing, J. K. (2016). On estimation of bias field in MRI images: polynomial vs Gaussian surface fitting method. *Journal of Chemometrics*, 30(10):602–620.

Kasiri, K., Javad, D. M., Kazemi, K., Sadegh, H. M., and Kafshgari, S. (2010). Comparison evaluation of three brain MRI segmentation methods in software tools. *2010 17th Iranian Conference of Biomedical Engineering (ICBME)*, (November):1–4.

Kass, M., Witkin, A., and Terzopoulos, D. (1988). Snakes: Active contour models. *International Journal of Computer Vision*, 1(4):321–331.

Kimmel, R. (2003). Fast Edge Integration. *Geometric Level Set Methods in Imaging Vision and Graphics*, 0:59–77.

Lankton, S. and Tannenbaum, A. (2008). Localizing region-based active contours. *IEEE Transactions on Image Processing*, 17(11):2029–2039.

Lee, S. H. and Seo, J. K. (2006). Level set-based bimodal segmentation with stationary global minimum. *IEEE Transactions on Image Processing*, 15(9):2843–2852.

Lewis, E. B. and Fox, N. C. (2004). Correction of differential intensity inhomogeneity in longitudinal MR images. *NeuroImage*, 23(1):75–83.

Li, C., Gatenby, C., Wang, L., and Gore, J. C. (2009a). A robust parametric method for bias field estimation and segmentation of MR images. In *2009 IEEE Computer Society Conference on Computer Vision and Pattern Recognition Workshops, CVPR Workshops 2009*, pages 218–223.

Li, C., Gore, J. C., and Davatzikos, C. (2014). Multiplicative intrinsic component optimization (MICO) for MRI bias field estimation and tissue segmentation. *Magnetic Resonance Imaging*, 32(7):913–923.

Li, C., Huang, R., Ding, Z., Gatenby, C., Metaxas, D., and Gore, J. (2008a). A variational level set approach to segmentation and bias correction of images with intensity inhomogeneity. In *Lecture Notes in Computer Science (including subseries Lecture Notes in Artificial Intelligence and Lecture Notes in Bioinformatics)*, volume 5242 LNCS, pages 1083–1091.

Li, C., Huang, R., Ding, Z., Gatenby, J. C., Metaxas, D. N., and Gore, J. C. (2011). A level set method for image segmentation in the presence of intensity inhomogeneities with application to MRI. *IEEE Transactions on Image Processing*, 20(7):2007–2016.

Li, C., Kao, C. Y., Gore, J. C., and Ding, Z. (2007). Implicit active contours driven by local binary fitting energy. In *Proceedings of the IEEE Computer Society Conference on Computer Vision and Pattern Recognition*.

Li, C., Kao, C. Y., Gore, J. C., and Ding, Z. (2008b). Minimization of region-scalable fitting energy for image segmentation. *IEEE Transactions on Image Processing*, 17(10):1940–1949.

Li, C., Xu, C., Anderson, A. W., and Gore, J. C. (2009b). MRI tissue classification and bias field estimation based on coherent local intensity clustering: A unified energy minimization framework. In *Lecture Notes in Computer Science (including subseries Lecture Notes in Artificial Intelligence and Lecture Notes in Bioinformatics)*, volume 5636 LNCS, pages 288–299.

Li, C., Xu, C., Gui, C., and Fox, M. (2005). Level Set Evolution without Re-Initialization: A New Variational Formulation. In *2005 IEEE Computer Society Conference on Computer Vision and Pattern Recognition (CVPR'05)*, volume 1, pages 430–436.

Li, C., Xu, C., Gui, C., and Fox, M. D. (2010). Distance regularized level set evolution and its application to image segmentation. *IEEE Trans Image Process*, 19(12):3243–3254.

Li, X., Jiang, D., Shi, Y., and Li, W. (2015). Segmentation of MR image using local and global region based geodesic model. *Biomedical Engineering Online*, 14(1):8.

Malladi, R., Sethian, J., and Vemuri, B. (1995). Shape modeling with front propagation: a level set approach. *IEEE Transactions on Pattern Analysis and Machine Intelligence*, 17(2):158–175.

Matthews, B. W. (1975). Comparison of the predicted and observed secondary structure of T4 phage lysozyme. *BBA - Protein Structure*, 405(2):442–451.

Meyer, C. R., Bland, P. H., and Pipe, J. (1995). Retrospective correction of intensity inhomogeneities in MRI. *IEEE Transactions on Medical Imaging*, 14(1):36–41.

Mumford, D. and Shah, J. (1989). Optimal approximations by piecewise smooth functions and associated variational problems. *Communications on Pure and Applied Mathematics*, 42(5):577–685.

Nock, R. and Nielsen, F. (2004). Statistical region merging. *IEEE Transactions on Pattern Analysis and Machine Intelligence*, 26(11):1452–1458.

Ohlander, R., Price, K., and Reddy, D. R. (1978). Picture segmentation using a recursive region splitting method. *Computer Graphics and Image Processing*, 8(3):313–333.

Osher, S. and Paragios, N. (2003). *Geometric level set methods in imaging, vision, and graphics*.

Osher, S. and Sethian, J. A. (1988). Fronts propagating with curvature-dependent speed: Algorithms based on Hamilton-Jacobi formulations. *Journal of Computational Physics*, 79(1):12–49.

Panton, R. L. (2013). *Incompressible Flow*. John Wiley and Sons, Inc.

Peng, Y., Liu, F., and Liu, S. (2014). Active contours driven by normalized local image fitting energy. *Concurrency Computation Practice and Experience*, 26(5):1200–1214.

Saleh, A., Abdel-Nasser, M., Akram, F., García, M. A., and Puig, D. (2016a). Analysis of temporal coherence in videos for action recognition. In *Image Analysis and Recognition - 13th International Conference, ICIAR 2016, in Memory of Mohamed Kamel, Póvoa de Varzim, Portugal, July 13-15, 2016, Proceedings*, pages 325–332.

Saleh, A., García, M. A., Akram, F., Abdel-Nasser, M., and Puig, D. (2016b). Exploiting the kinematic of the trajectories of the local descriptors to improve human action recognition. In *Proceedings of the 11th Joint Conference on Computer Vision, Imaging and Computer Graphics Theory and Applications (VISIGRAPP 2016) - Volume 3: VISAPP, Rome, Italy, February 27-29, 2016.*, pages 182–187.

Sethian, J. A. (1999). *Level set methods and fast marching methods.*

Shattuck, D. W. and Leahy, R. M. (2002). Brainsuite: An automated cortical surface identification tool. *Medical Image Analysis*, 6(2):129–142.

Smith, S. M., Jenkinson, M., Woolrich, M. W., Beckmann, C. F., Behrens, T. E. J., Johansen-Berg, H., Bannister, P. R., De Luca, M., Drobnjak, I., Flitney, D. E., Niazy, R. K., Saunders, J., Vickers, J., Zhang, Y., De Stefano, N., Brady, J. M., and Matthews, P. M. (2004). Advances in functional and structural MR image analysis and implementation as FSL. *Neuroimage*, 23(SUPPL. 1):S208–S219.

Studholme, C., Cardenas, V., Song, E., Ezekiel, F., Maudsley, A., and Weiner, M. (2004). Accurate Template-Based Correction of Brain MRI Intensity Distortion with Application to Dementia and Aging. *IEEE Transactions on Medical Imaging*, 23(1):99–110.

Vese, L. A. and Chan, T. F. (2002). A multiphase level set framework for image segmentation using the Mumford and Shah model. *International Journal of Computer Vision*, 50(3):271–293.

Vokurka, E. A., Thacker, N. A., and Jackson, A. (1999). A fast model independent

UNIVERSITAT ROVIRA I VIRGILI
AVANCES EN SISTEMAS INTERACTIVOS PARA PERSONAS CON PARÁLISIS CEREBRAL
Farhan Akram

method for automatic correction of intensity nonuniformity in MRI data. *Journal of Magnetic Resonance Imaging*, 10(4):550–562.

Vovk, U., Pernus, F., and Likar, B. (2004). MRI intensity inhomogeneity correction by combining intensity and spatial information. *Physics in Medicine and Biology*, 49(17):4119–4133.

Vovk, U., Pernus, F., and Likar, B. (2006). Intensity inhomogeneity correction of multispectral MR images. *NeuroImage*, 32(1):54–61.

Vovk, U., Pernus, F., and Likar, B. (2007). A review of methods for correction of intensity inhomogeneity in MRI. *IEEE Transactions on Medical Imaging*, 26(3):405–421.

Wang, L., He, L., Mishra, A., and Li, C. (2009a). Active contours driven by local Gaussian distribution fitting energy. *Signal Processing*, 89(12):2435–2447.

Wang, L., Li, C., Sun, Q., Xia, D., and Kao, C. Y. (2009b). Active contours driven by local and global intensity fitting energy with application to brain MR image segmentation. *Computerized Medical Imaging and Graphics*, 33(7):520–531.

Wang, X. F., Huang, D. S., and Xu, H. (2010). An efficient local Chan-Vese model for image segmentation. *Pattern Recognition*, 43(3):603–618.

Xie, X., Zhang, A., and Wang, C. (2015). Local average fitting active contour model with thresholding for noisy image segmentation. *Optik*, 126(9-10):1021–1026.

Xu, C., Yezzi, A., and Prince, J. L. (2000). On the relationship between parametric and geometric active contours. In *Conference Record of the Thirty-Fourth Asilomar Conference on Signals, Systems and Computers (Cat. No.00CH37154)*, volume 1, pages 483–489 vol.1.

Zhang, K., Liu, Q., Song, H., and Li, X. (2015). A variational approach to simultaneous image segmentation and bias correction. *IEEE Transactions on Cybernetics*, 45(8):1426–1437.

Zhang, K., Song, H., and Zhang, L. (2010a). Active contours driven by local image fitting energy. *Pattern Recognition*, 43(4):1199–1206.

Zhang, K., Zhang, L., Lam, K., and Zhang, D. (2016). A level set approach to image segmentation with intensity inhomogeneity. *IEEE Transaction on Cybernetics*, 46(2):546–557.

Zhang, K., Zhang, L., Song, H., and Zhou, W. (2010b). Active contours with selective local or global segmentation: A new formulation and level set method. *Image and Vision Computing*, 28(4):668–676.

Zhang, Y., Brady, M., and Smith, S. (2001). Segmentation of brain MR images through a hidden Markov random field model and the expectation-maximization algorithm. *IEEE Trans Med Imaging*, 20(1):45–57.

Zhang, Y., Matuszewski, B. J., Shark, L.-K., and Moore, C. J. (2007). A novel medical image segmentation method using dynamic programming. In *International Conference on Medical Information Visualisation-BioMedical Visualisation, MediVis'07.*, pages 69–74. IEEE.

UNIVERSITAT ROVIRA I VIRGILI
AVANCES EN SISTEMAS INTERACTIVOS PARA PERSONAS CON PARÁLISIS CEREBRAL
Farhan Akram

UNIVERSITAT
ROVIRA i VIRGILI